African Journal of Engineering Research and Innovation

AJERI Vol 2. No. 2. 2024

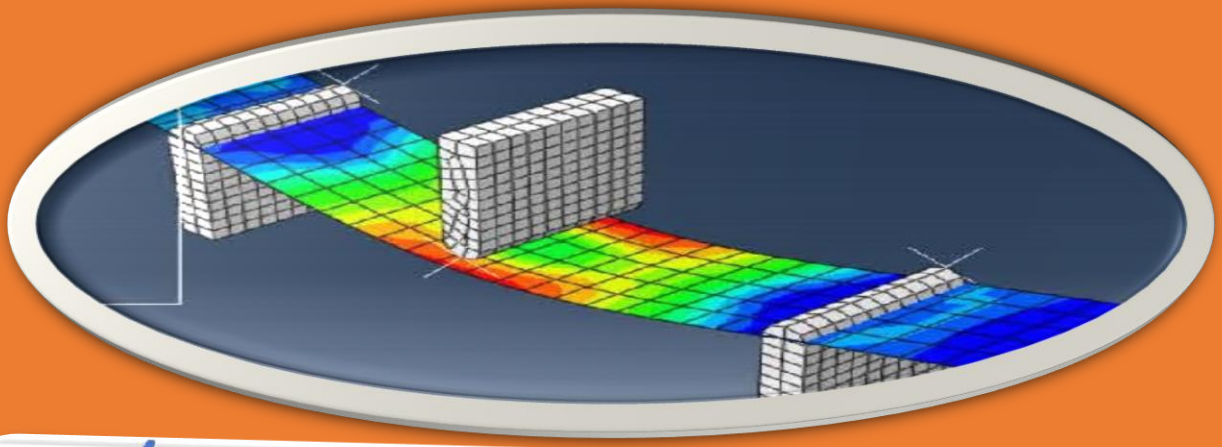

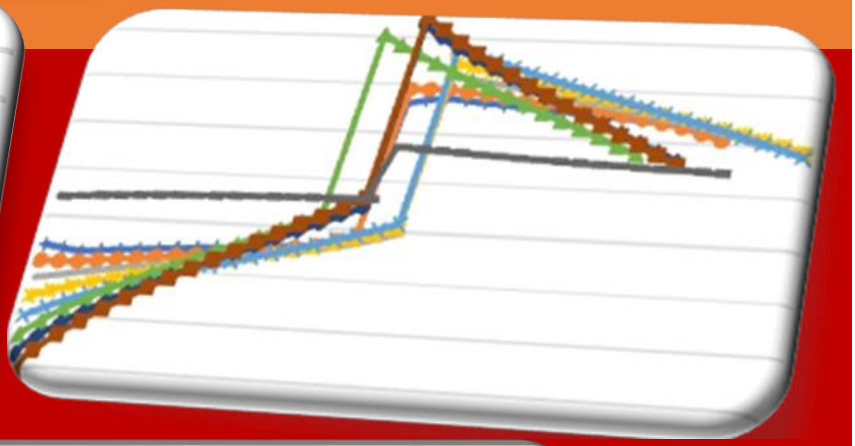

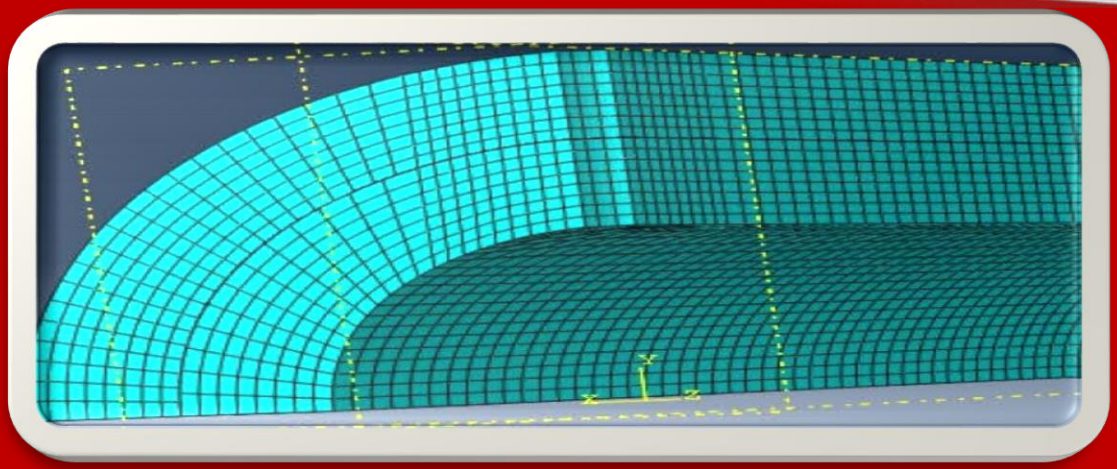

The Institution of Engineers of Kenya

ISSN: 2957- 7780

In partnership with

ISSN: 2957- 7780

AJERI

African Journal of Engineering in Research and Innovation

ISSN: 2957- 7780 Volume 2. No 2. 2024

Published by:

The *Institution of Engineers of Kenya*

P.O Box 41346- 00100

Nairobi Kenya

Tel: +254 (20) 2729326, 0721 729363, (020) 2716922

Email: editor@iekenya.org

Website: www.iekenya.org

IEK

African Journal of Engineering Research and Innovation (AJERI), is published by **The *Institution of Engineers of Kenya*,** IEK, as an international forum for publication of high-quality papers in all areas of Engineering

 ISSN: 2957- 7780

CONTENTS **Pages**

Tuning Protocol Stack Layers for Improved Communication in Wireless Sensor Networks

[1]R. Kufakunesu, [2]M. O. Odhiambo

[1]Department of Electrical and Smart Systems Engineering University of South Africa, [2]Mangosuthu University of Technology, Durban, South Africa

[1]rkufakunesu@gmail.com , [2]ohanga.marcel@mut.ac.za

Article History
Submission Date: 5th September 2023
Acceptance Date: 20th December 2023
Publication Date: 30th June 2024

Abstract

Wireless sensor networks (WSNs) monitor events or gather information and report the information to a sink node, or a base station. Wireless communication is the main activity that consumes energy in WSNs, thus, conserving energy is very important as the nodes depend on batteries for communication. In this paper we propose a cross-layer scheme that improves energy efficiency by tuning the exchange and control of data between two layers. A Markov Chain model is employed to analyse the effect of tuning the physical and media access control layers, to find possible energy gains. The study utilises the IEEE 802.11 channel and S-Aloha MAC protocol in a star topology WSN. Reed Solomon codes, a form of Forward Error Correction (FEC) and channel access probability were used to explore their effect on energy efficiency. Analytical and MATLAB simulation models are used to identify the statistics of collisions, overall packets transmitted, as well as the total number of slots used during transmission. The proposed cross-layer tuning approach results in quantifiable potential energy gains which improve the lifetime of the WSN.

Keywords - Cross-layer tuning, energy efficiency, forward error correction (FEC), IEEE 802.11, markov chain, Reed Solomon, wireless sensor network.

1. Introduction

A wireless sensor network (WSN) is a wireless set of nodes expansively distributed, that uses sensors to record physical quantities such as temperature, pressure, motion and sound in the environment. The battery provides the power for each sensor node [1]. A critical feature in the application of wireless sensor networks is the lifetime of the network. The network lifetime must be sufficient for the objective of the WSN to be achieved. The supply of power to the sensor

 ISSN: 2957- 7780

nodes is limited, thus posing a big challenge in WSN deployment. Since wireless sensors depend on battery power for their operation, it is difficult to replace the batteries once the sensors are deployed in the field. This energy scarcity impacts on the network's localisation and routing protocols. The major activity that consumes energy in a WSN is wireless communication, that is, message size, transmission of messages, receiving messages, node awake time, and distance between nodes. The power utilisation of wireless devices greatly depends on the operations in the physical layer. The MAC layer, on the other hand, manages the wireless resources for the physical layer and therefore directly influences energy consumption. The MAC protocols contribute to energy depletion when there are collisions, overhearing, idle listening and through the control packets [2].

Researchers have devised methods to efficiently utilise the limited energy available for WSN by optimising the design parameters and protocols. The most common cross-layer design developed is between the physical layer and the MAC layer compared to any combination of the other layers in the protocol stack. This is mainly because they are adjacent to each other [3][4][5][6][7]. Significant work has been presented in the endeavour to minimise energy consumption at the MAC layer and it has been found that energy can be conserved in the physical layer by optimising its parameters [8].

This study focuses on tuning the adjacent layers of the protocol stack, the physical layer and the MAC layer, to improve the communication performance in a WSN using the Markov chain model and Reed Solomon forward error correction coding on an 802.11g channel with Additive White Gaussian Noise (AWGN). The model framework in [9] was used for cross-layer tuning in this research. While the authors in [9] used impulse radio ultra-wide band signals, in this body of work we use Wi-Fi signals. IEEE 802.11g is commonly known as Wi-Fi whose typical structure is the star topology, with many wireless stations connecting to an access point (AP) that then connects to a network infrastructure. The MAC and PHY specifications for implementation are given in [10]. The key benefit of developing 802.11g sensing systems is its compatibility with already existing networks and infrastructure.

The remainder of the paper is organized as follows. Related work is covered in Section II. In Section III we provide the methodology used to obtain the results. An analysis of the test results is covered under Section IV. Finally, Section V concludes the paper and provides recommendations for future studies.

ISSN: 2957- 7780

2. Related Work

Individual layer optimisation in wireless sensor networks has been the norm in the recent past until the advent of cross-layer optimisation. In wireless sensor networks, the typical objectives of cross-layer optimisation are minimisation of energy utilisation [11], optimal scheduling [12], efficient routing [13], topology control [14] and QoS provisioning [15].

The authors in [16], combined the processes of the conventional communication layers into a single protocol that has reliable communication with minimum energy utilisation, local congestion avoidance and adaptive communication decisions. Analysis and evaluation of the performance and results of the simulation experiment showed that XLP significantly improved the communication operation and eclipsed the conventional protocol layer scheme regarding both the complexity of implementation and the network performance.

Another cross-layer approach was proposed in [17] wherein the authors exploited the interface between the MAC layer and the network layer. They introduced a cross-layer routing protocol, known as the Cross-Layer Balancing routing (CLB-routing) which improves the network lifetime by offsetting the energy utilisation in the forwarding effort between nodes. The network layer utilises the data provided by the MAC layer about the communication overheads of all the neighbouring nodes. This data informs the transmitting node the frequency of data transmission by the forwarding nodes and selects the least used nodes for data transmission, thus balancing the load. Their results showed that energy could be saved by using CBL-routing protocol because it utilised all the forwarding nodes equitably avoiding network partitioning which drains energy.

Cross-layer optimisation of the physical layer, MAC layer and network layers was proposed in [18]. The cross-layer approach maximises the network lifetime of a WSN with limited interference for AWGN and Rayleigh fading channels. They expressed the network lifetime maximisation as a non-linear optimisation problem, incorporating power allocation, link scheduling, transmission rate and routing flow processes for every active time slot. They relaxed the resulting non-convex rate constraint by using an estimation of the signal-to-interference-plus-noise ratio (SINR) to transform it to a convex rate. They developed the Lagrangian form of the optimisation problem and used the Karush-Kuhn-Tucker (KKT) optimality conditions to derive the analytical statements for their network topology. They achieved the maximum network lifetime for both Rayleigh fading channels and AWGN under varied conditions. From their numerical results, they found that they needed to increase transmit power to combat poor channel conditions caused by fading. Simultaneous link scheduling with very weak interference allowed

 ISSN: 2957- 7780

the authors to exploit spatial reuse, wherein activating concurrent transmissions at decreased rates dictates decreased transmission power, resulting in an extended network lifetime.

WSN application to the body was used in [19]. They proposed a network optimisation approach that combines network topology and cross-layer optimisation to prolong the life of the network. They propose primal and dual decomposition technique to convert the original non-convex problems to convex ones. They solve the optimisation problems using CVX solvers. The authors combine the optimum location of the relay nodes positioned on the surface of the body, and the optimum transmission power and transmission time of the embedded sensor nodes to maximise the lifetime of the network. The decision of the optimum information forwarding on the routing layer and that of of transmission power and transmission time control on the physical layer are taken into account concurrently. The results showed an improvement in network performance.

Analytical and simulation models have been used in the evaluation of the performance of different medium access control protocols. In [20], the author propositioned a Markov model that analyses saturation throughput with idea channel conditions of IEEE 802.11 having finite stations that always have a packet to transmit but with infinite retransmissions. The study in [21] provides a Markov model that evaluates the performance of a single-hop network using SMAC, analysing network throughput, packet service delay and energy utilisation. The model, nonetheless, does not take into account packet queueing delay which is essential in determining packet latency. Some work focuses on the analysis of specific metrics for a particular MAC protocol or a string of them that have comparable characteristics, like the work presented in [22], where they analyse the dispersion of end-to-end delay in a wireless sensor network using a Markov process. Many researchers have analysed the behaviour and performance of PHY and MAC layers using FEC [23-29] and stochastic techniques respectively [30, 31]. Although these studies analysed the behaviour and performance of optimising the layers, most of the studies do not quantify the gains achieved.

This proposed solution differs from the existing solutions in that our proposed mathematical model accurately describes contention at the MAC layer, which is not apparent in the existing solutions as they assume an ideal receiver. The proposed solution also evaluated and quantified the energy gains achieved by the cross-layer optimisation of PHY and MAC layer and produced expected results which are reflective of more realistic parameter considerations. We use the model framework introduced in [9]. While the authors used ultra-wideband signals with non-coherent energy detection, in this paper we use the IEEE 802.11g channel with AWGN.

 ISSN: 2957- 7780

3. System Model

The PHY layer and MAC layer were tuned to improve communication performance in a wireless sensor network. The PHY layer was optimized by the introduction of forward error correction in the form of Reed Solomon (RS) code. The energy consumption performance was evaluated for a range of code rates. The medium access control protocol employed is S-Aloha because of its low communication overhead and ease of implementation.

The probability of packet collision when accessing the channel was employed to tune the MAC layer. A contention-free MAC protocol, SMAC, was also used to compare energy consumption between the two MAC protocols. The proposed mathematical model accurately describes contention at the MAC layer. This allowed for the determination of practical synchronized transmissions under different MAC schemes. Potential energy gains were determined for different RS codes considering the probability of channel access. The research evaluated the average number of steps required for a sensor node to successfully transfer a data frame during a transmission period using a Markov chain model. The model facilitated the determination of the number of steps required for every sensor node to have broadcast its information to the sink node successfully. When the length of every step is known, the number of steps to absorption can be converted into time to absorption. Knowledge of the time to absorption facilitated for the analysis of the consequence of tweaking the parameters of the protocol stack.

A. Assumptions

(i) The sensor nodes are homogenous.

(ii) The sensor nodes are stationary, and their position will not change after deployment.

(iii) The sink node is a full function device and receives all the data transmitted from the sensor nodes

(iv) A sensor node does not generate a new packet for transmission until the previous one is delivered successfully.

B. Network Setup

The WSN is a star topology that comprised twenty homogenous sensor nodes that are stationary and whose position would not change after deployment. The sink node is a full function device and received all the data streams from the sensor nodes and could connect with other sink nodes within range. The sensor nodes do not generate new packets for broadcast pending the successful delivery of the previous packet. The activities of this network setup took place as follows:

 ISSN: 2957- 7780

(i) A beacon message is sent to the sensor nodes for synchronisation with the sink node and to identify when they will attempt to access the channel

(ii) Beacon message contains information about the length of the transmission slot and its starting time.

(iii) There are M nodes with a data packet to transmit.

(iv) If **M**-1 nodes independently sense a spike in temperature after the first node transmission period has started, it is assumed that for these nodes, either their timer has not expired or the spike in the reading is not critical enough to trigger the transmission of the wake-up signal to the sink node.

(v) The sink node determines in which slot every sensor node transmits. Once sensor nodes receive the beacon message, they are then able to transmit the data packets during the allocated transmission slot.

(vi) Sink node allocates reserved time slots to every node that requires communication with the sink node by sending the acknowledge message (ACK).

(vii) If there is a single transmission in a slot, there will be no collision and the probability of success hinges on the probability of bit error at the receiver detection process.

(viii) If the transmission is unsuccessful owing to collisions or channel errors, the nodes attempt to resend the packet in a new slot.

(ix) If the transmission is successful, the node will enter a sleep mode.

(x) Throughout the period of transmission, new packets can arrive independently at every node with some probability. Buffering of data packets is not supported at the nodes, but a new packet can replace the old packet, in which case the node transmits only the latest sensor observation.

(xi) The period of transmission terminates when each node has successfully sent its data packet and entered a sleep mode.

(xii) The number of nodes that do not have a packet to transmit at the beginning of the competition period cannot be larger than M during the transmission period because it is assumed that the nodes that do not have a packet to transmit at the beginning of the competition period will stay in sleep mode and transmit their observations on the next transmission period.

C. Physical Layer Tuning

Binary modulation was employed to allow the communication system to send data at the least power expenditure that is practicable. Energy consumption for uncoded and coded transmission

 ISSN: 2957- 7780

was determined by computing the bit error probability during transmission. Calculating the packet transmission probability provided one of the inputs of the Markov chain model to calculate the state transition probabilities. Table I shows the characteristics of the transceivers used in the study.

Table 1: Physical layer characteristics for transceivers

Characteristic	Type
IEEE Standard	802.11g
Frequency Band	2.4GHz
Modulation	BPSK
Spreading Method	OFDM
Communication Range	40m
Bandwidth	20MHz
Transmission Scheme	CSMA/CA
Channel	AWGN

The bit error rate performance of the uncoded OFDM scheme over the AWGN channel is given by:

$$P_b = Q\left[\sqrt{\frac{2E_b}{N_0}}\right] = \frac{1}{2}erfc\left(\sqrt{\frac{E_b}{N_o}}\right) \quad (1)$$

The packet error probability (PEP) will thus be given by:

$$PEP = 1 - (1 - P_b)^D. \quad (2)$$

where D is the length of the packet in bits = 127 bytes = 1016 bits.

The desired BER: $P_b = 10^{-5}$

The BER performance of the Reed Solomon coded OFDM system over the AWGN channel is given by:

$$P_{b.i} = Q\left(\frac{2E}{N_o}\right). \quad (3)$$

Where $E = r_i E_b$ and r_i is the i^{th} code rate

The project explored the possible energy gains that could be accomplished by tuning the rate for forward error correction, in this case Reed-Solomon Codes.

RS code operates with the following parameters:

(a) Symbol length: bits per symbol b = 6.
(b) Block length: $n = 2^b - 1$, symbols.
(c) Message data length: $k = 2^b - 1 - 2t$, symbols.
(d) Redundant/parity bits: t
(e) Size of parity check code: n-k = 2t symbols.
(f) Code rate: $r = {}^{k}/_{n}$.

ISSN: 2957- 7780

Different code rates were applied to study performance of the network in terms of energy utilisation. SMAC and S-Aloha protocols were used as media access control and a comparison done between the two protocols that is for t = {3, 5, 6, 7, 8}

Symbol error probability before decoding

$$P_{sym.i} = 1 - (1 - P_{b.i})^{b}. \quad (4)$$

Decoded symbol error probability in the case of hard decision

$$\mathrm{P}_{ds.i} = \frac{1}{n}\sum_{e=t+1}^{n} \binom{n}{e} {P_{sym.i}}^{e}(1 - P_{sym.i})^{n-e}. \quad (5)$$

The packet error probability (PEP_i) will thus be given by:

$$PEP_i = 1 - (1 - P_{ds.i})^{X_i}. \quad (6)$$

Where $X_i = \frac{D_i}{b}$ and is the number of code symbols in a packet,

$D_i = \frac{D}{r_i}$ is the packet length when using code rate r_i.

D. MAC Layer Tuning

The nodes that require communication with the sink node are not known at any given time because that hinges on the number of nodes that have data packets to transmit. The MAC layer is optimal when there is maximum channel access for the transmission of a packet to take place. Finding the probability of successful channel access provided input to calculate the state transition probabilities in the Markov chain model. The probability that any node has accessed the channel in a slot is given by:

$$P_{succ}^{MAC}(p) = Mp(1 - p)^{M-1}. \quad (7)$$

The probability that j nodes successfully accessed the channel is given by:

$$P_{succ}^{MAC}(p) = (M - j)p(1 - p)^{M-j-1}. \quad (8)$$

where *M* is the number of nodes competing for channel access in a slot with probability *p*.

By computing the derivative of Equation (7), the maximum channel access efficiency can be established at the value of zero:

$$P_{succ}^{MAC} = (p*)' = 0, \quad (9)$$

ISSN: 2957- 7780

which occurs when $p* = \frac{1}{M}$, explicitly, when the quantity of slots in the transmission period matches the number of nodes competing for the channel. This scenario corresponds to the traffic load $G = 1$.

Thus, the probability of successful maximum channel access can be computed as:

$$P_{succ}^{MAC}(p*) = (1 - 1/M)^{M-1}. \quad (10)$$

The values of p used in the project are:

$$p = \left\{0.05,\ 0.1,\ 0.2, {}^{1}/_{M-j}\right\}.$$

E. Network Traffic Generation

In this event-driven wireless temperature sensor network, the traffic arrival process was modelled dusing the Poisson process. The network traffic load is expressed as:

$$G = \theta T_f, \quad (11)$$

where θ is the average packet arrival rate per second and T_f is the duration of uncoded data transmission.

If the data transmission is coded, the packet duration is affected by the coding overhead, by the component $1/r_i$ and as such, the slot interval needs to accommodate this overhead.

$$P_r(a = \varsigma) = \frac{(\rho\tau)^{\varsigma}}{\varsigma} e^{-\rho\tau}. \quad (12)$$

where $a = \varsigma$ new packets arrive independently at each node during a time period τ according to a Poisson probability distribution with ρ packets / s.

ς is the number of arrivals according to a Poisson distribution

τ is the time period for the Poisson process

ρ is the number of packets per second in a Poisson process

The specifications for the WSN design are given in Table 2.

Table 2: Parameters employed for performance evaluation

Parameter	Definition	Value
b	Bits per coded symbol	6
N	Number of nodes in the network	20
M	Number of nodes with packet to transmit at the initial state	20

ISSN: 2957- 7780

Parameter	Definition	Value
P	Probability to transmit in a slot	0.05,0.1,0.2, 1/(M-j)
ρ	Arrival rate for Poisson arrival process	0.05events/sec
L_{PMH}	Payload and MAC layer header	130 bytes
L_{PH}	PHY layer header	6 bytes
L_{ACK}	ACK frame size	14 bytes
L_{CTS}	CTS frame size	14 bytes
L_{RTS}	RTS frame size	20 bytes
L_{PRE}	Preamble length	18 bytes
SIFS	Short inter-frame space	10µs
DIFS	Distributed Coordination Function inter-frame space	28µs
CW	Contention Window size	0-15
$T_{MaxWaitACK}$	Maximum wait time for ACK frame	160µs
R	Bitrate in Mbps	1Mbps
$P_{tx,circ}$	Transmitter circuitry power consumption	60mW
$P_{tx,RF}$	Transmitter RF power component	6mW
P_{idle}	Idle mode power consumption	2mW

F. Markov Chain Model

There are events that can transpire in the Markov chain model including the following:

(i) Successful channel access & successful transmission & no new arrivals => move from state j to state $j + 1$; Probability for event 1 is defined as:

$$P_{(1)} = P_{succ}^{MAC} P_{succ}^{PHY} P_{\Omega}(\Omega = 0) \quad (13)$$

(ii) Successful channel access and successful transmission and κ node(s) have a new packet=> move from state j to state $j - \kappa + 1$; Probability for event 2 is defined as:

$$P_{(2)} = P_{succ}^{MAC} P_{succ}^{PHY} P_{\Omega}(\Omega = \kappa). \quad (14)$$

(iii) Unsuccessful channel access and no new arrivals => stay in state j; Probability for event 3 is defined as:

$$P_{(3)} = P_{fail}^{MAC} P_{\Omega}(\Omega = 0). \quad (15)$$

(iv) Successful channel access and unsuccessful transmission and no new arrivals => stay in state j; Probability for event 4 is defined as:

$$P_{(4)} = P_{succ}^{MAC} P_{fail}^{PHY} P_{\Omega} = (\Omega = 0). \quad (16)$$

(v) Unsuccessful channel access and κ node(s) have a new packet => move from state j to state $j - \kappa$; Probability for event 5 is defined as:

$$P_{(5)} = P_{fail}^{MAC} P_{\Omega}(\Omega = \kappa). \quad (17)$$

ISSN: 2957- 7780

(vi) Successful channel access and unsuccessful transmission and κ node(s) have a new packet => move from state j to state $j - \kappa$; Probability for event 6 is defined as:

$$P_{(6)} = P_{succ}^{MAC} P_{fail}^{PHY} P_{\Omega}(\Omega = \kappa). \quad (18)$$

To calculate the probabilities for the state transitions for the distinct events in the Markov chain model, knowing the following probabilities is imperative.

(i) The probability of successful channel access (P_{succ}^{MAC}),

(ii) The probability of successful packet transmission (P_{succ}^{PHY}),

(iii) The probability of new packet arrivals $P_{\Omega}(\Omega = \kappa)$.

Let $P_{\Omega}(\Omega = \kappa)$ be defined to be the probability that $\kappa = 0, 1, \ldots, j$ node(s) will have a new packet to transmit according to a Poisson probability distribution.

For the scenario when one sensor node has successful channel access, successful transmission and no new arrivals happening at that node, the probability of state transition is:

$$P_{0,1} = P_r\{S_{t+1} = 1 | S_t = 0\} = Mp(1-p)^{M-1} P_q P_{succ}^{PHY}, \quad (19)$$

where S_t and S_{t+1} represent the value of the state at the event times t and $t + 1$, respectively. M is the number of nodes competing for the channel access at the state S_t. $P_{0,1}$ is the probability for moving from state 0 to 1.

The probability of success in the PHY layer, $P_{succ}^{PHY} = 1 - PEP$, may be computed by applying Equation (2) and Equation (6) for the scenario with no coding and the coded scenario respectively.

The probability that no new packet arrives at the node's queue is given by:

$$P_q = P_r(a = 0) = 1 - P_a, \quad (20)$$

where $P_a = P_r(a > 0)$ is the probability that new packets arrive at the node's queue.

The probability of remaining in the starting state is:

$$P_{0,0} = P_r\{S_{t+1} = 1 | S_t = 0\} = 1 - P_{0,1} = 1 - Mp(1-p)^{M-1} P_q P_{succ}^{PHY}, \quad (21)$$

which means none of the sensor nodes successfully transmit a packet and the system stays in its starting state. The probability of that event is the complement of the probability that any of the M nodes is successful.

The probability of transition from state j to state $j + 1$ is defined as:

 ISSN: 2957- 7780

$$P_{j,j+1} = P_r\{S_{t+1} = j + 1 | S_t = j\} = (M - j)p(1 - p)^{M-j-1}\left[P_q\right]^{j+1} P_{succ}^{PHY}. \quad (22)$$

In this instance, one of the $(M - j)$ nodes that have a packet to transmit, successfully access the channel and transmits the packet successfully with no new packets arriving at the nodes that do not have anything to transmit in their queue. The probability of transition of remaining in state j should also be computed putting into consideration the situation where new packet arrivals occur. In that circumstance, the Markov chain shifts κ steps towards the starting state.

In the case that the system is in state j and one node successfully transmits a packet, it implies that at most $\kappa = j + 1$ sensor nodes can have a new packet arrival. However, in the case where packet transmission is not successful while the chain is in the starting state j, it means at most $\kappa = j$ nodes can have a new packet arrival. Consequently, the probability of the chain transitioning κ steps towards its starting state is given as:

$$P_{j,j-\kappa} = P_r\{S_{t+1} = j - \kappa | S_t = j\} = (M - j)p(1 -)^{(M-j-1)}\binom{j+1}{\kappa+1}[P_a]^{\kappa+1}\left[P_q\right]^{j-\kappa+1} P_{succ}^{PHY} + (1 - (M - j)p(1 - p)^{M-j-1} P_{succ}^{PHY}\binom{j}{\kappa}[P_a]^{\kappa}\left[P_q\right]^{j-\kappa}, \quad (23)$$

where $\kappa = [1, \ldots, j]$. For the case $\kappa = 0$, the probability $p_{j,j}$ for remaining in the same state is calculated applying Equation (23). By utilizing the probabilities of state transition for the Markov chain, the number of steps required to shift from state 0 to state M can be evaluated, where every sensor node has transmitted its packet(s) successfully as explained in the next section.

G. Time to absorption

Decomposing the transition matrix **P** is given by:

$$\boldsymbol{P} = \begin{bmatrix} \boldsymbol{V} & \boldsymbol{R} \\ \boldsymbol{O^T} & \boldsymbol{1} \end{bmatrix}, \quad (24)$$

where the matrix **V** consists of elements $V_{x,y} = P_{x,y}$ for $x, y = 0, 1, \ldots, M - 1$ and

$$\boldsymbol{R^T} = [0\ 0 \ldots P_{(M-1),M}].$$

The fundamental matrix for the absorbing chain is defined as:

$$\boldsymbol{\Lambda} = [\boldsymbol{I} - \boldsymbol{V}]^{-1} \quad (25)$$

which is composed of elements $\lambda_{x,y}$ for $x, y = 0, 1, \ldots, M - 1$. If the initial state is$S = 0$, then the mean number of steps to absorption is:

$$\Gamma_0 = \sum_y \lambda_{0,y}. \quad (26)$$

ISSN: 2957- 7780

The duration of single step (slot) must be such that the data packet can be transmitted and the following ACK message can be received successfully, that is, the slot duration given as:

$$T_{slot,i} = T_{f,i} + T_{MaxAckWait} + T_{ACK}, \quad (27)$$

where $T_{f,i} = T_f / r_i$ (and for the uncoded case $r_i = 1$) is the interval of a data frame (payload and headers included) comprising the redundancy caused by the code rate i.

$T_{MaxAckWait}$ is the maximum time a node waits for an ACK frame before retransmitting a data packet.

T_{ACK} is the duration of an ACK frame.

Therefore, the expected time to absorption when using code rate *i* can be calculated as

$$\Theta_i = \Gamma_0 T_{slot,i}. \quad (28)$$

H. Transmission Period Analysis

A MATLAB simulation was used to detect the number of collisions, total number of transmitted packets and the number of idle slots spent during the transmission period. The values of bit error probability calculated analytically were utilized in the simulation model for the evaluation of the probability of successful transmission in the physical layer. A comparison of the analytical results and the simulation results was done in two ways to validate the correctness of the models:

(i) Results from the Markov chain model should correspond to the simulation model results relating to the number of steps to absorption; and

(ii) For a boundary scenario case, where there are no new packet arrivals during the competition period, the simulation results about the expected number of required transmissions to reach absorption should also correspond to the analytical results.

The analytical derivation of the required number of transmissions needed to reach absorption was done as described below. The mean number of steps required to transmit successfully when at Markov chain state *j* was obtained using Equation (22). The average number of steps needed for a node to be successful when at Markov chain state *j*, was derived using Equation (22), without considering the probability of new packet arrivals, as follows:

$$N_{steps,j} = \frac{1}{(M-j)p(1-p)^{(M-j-1)}P_{succ}^{PHY}}. \quad (29)$$

The expected number of transmissions that occur during a step, at state *j*, is computed as follows:

$$\mathrm{E}\{X_j\} = \sum_x P[X = x]x. \quad (30)$$

ISSN: 2957- 7780

where $x = [1, \ldots, M - j]$ and the probability that x nodes attempt to transmit at state j can be calculated as:

$$P_r[X = x] = \frac{G_j^x e^{-G_j}}{x!}. \quad (31)$$

where $G_j = p(M - j)$ is the offered traffic load at state j. The average number of transmissions required to arrive at the absorption state could therefore be calculated by taking into account all the states of the Markov chain as stated below:

$$N_{tx,MC} = \sum_{j=0}^{M} N_{steps,j}\, E\{X_j\}. \quad (32)$$

The average number of transmissions could be computed analytically using Equation (32) and compare with corresponding results from the simulation. Figure 1 shows the representation of the WSN simulation.

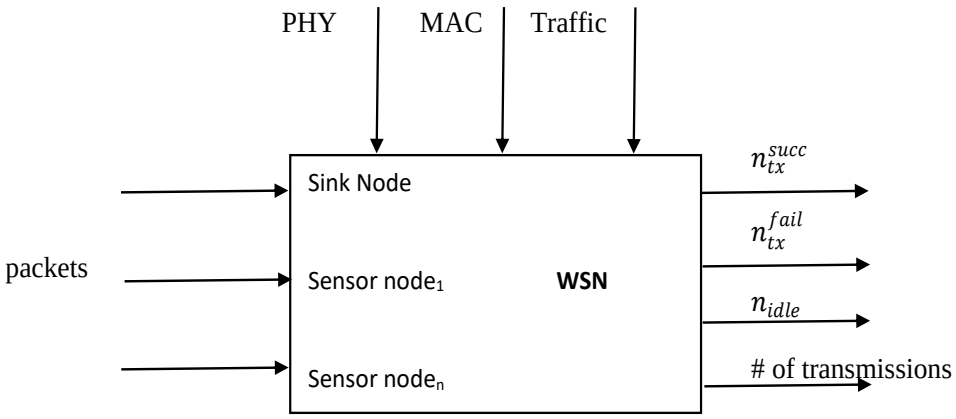

Figure 1: General Representation of WSN Simulation

I. Energy Consumption

The model for energy consumption that was employed for the evaluation of the impact of 802.11 PHY layer, SMAC and S-Aloha MAC layers on the energy utilization of the star topology network under study is described in this section. The model that was proposed could be used to compute the amount of energy depleted from the start of the period of transmission until each node has transmitted its packet(s) successfully. To compute energy consumption of the network, there is a need to know the power consumption for transmission and reception at the PHY and MAC layers. At the PHY layer, the power dissipated and hence the corresponding energy cost of a transmission has two elements; the internal circuitry expenditure and the radio frequency (RF) expenditure which is expressed as:

$$P_{tx,i} = r_i P_{tx,RF} + P_{tx,circ}, \quad (33)$$

ISSN: 2957- 7780

where the RF element is attributed to proportion of the energy content of the data packet with the applied code rate, meaning, $P_{tx,RF}$ would be multiplied by the applicable code rate r_i. This is because the energy per coded bit depends on the code that is being applied, as explained in Section III.C.

The power consumption of the receiver, P_{rx}, is attributed to the power consumed by every element at the receiver. The consumption of energy at the PHY layer for the transmission and reception of a packet could then be computed for code rate i as shown below:

$$E_{tx,i}^{PHY} = \left(r_i P_{tx,RF} + P_{tx,circ}\right) T_{f,i}. \quad (34)$$

$$E_{rx,i}^{PHY} = P_{rx} T_{f,i}. \quad (35)$$

The factors that affect energy consumption in the MAC layer are calculated in the following manner:

$$E_{tx,f}^{MAC} = P_{rx} T_{MaxAckWait},$$

$$E_{tx,s}^{MAC} = P_{rx} T_{MaxAckWait} + P_{rx} T_{ACK},$$

$$E_{rx}^{MAC} = P_{tx} T_{ACK},$$

$$E_{Imp}^{MAC} = P_{idle} T_{idle},$$

where T_{idle} is the length of the idle slot and P_{idle} is the power consumption in the idle mode.

Using the energy consumption model given as:

$$E_{TP} = n_{tx}^{fail}\left(E_{tx}^{PHY} + E_{tx.f}^{MAC}\right) + n_{tx}^{succ}\left(E_{tx}^{PHY} + E_{tx.s}^{MAC} + E_{rx}^{PHY} + E_{rx}^{MAC}\right) + E_{Imp}^{MAC} \quad (36)$$

and the derivations above, the computation of the network's average energy consumption when applying i^{th} code rate may be accomplished as follows:

$$E_{TP,i} = n_{tx}^{fail}\left(P_{tx,i} T_{f,i} + P_{rx} T_{MaxAckWait}\right) + n_{tx}^{succ}\left(P_{tx,i} T_{f,i} + P_{rx} T_{MaxAckWait} + P_{rx} T_{ACK} + P_{rx} T_{f,i} + P_{tx} T_{ACK}\right) + n_{idle}\ P_{idle} T_{idle}\ . \quad (37)$$

where;

n_{tx}^{fail} is the number of failed transmissions (due to MAC layer collision or PHY transmission errors) for the whole network,

n_{tx}^{succ} is the successful number of transmissions,

n_{idle} is the total number of idle slots spent throughout the transmission period.

 ISSN: 2957- 7780

The parameters $n_{tx}^{fail}, n_{tx}^{succ}$ and n_{idle} were obtained from the MATLAB simulations. For the case where no new packet arrivals occur, the analytical derivations presented earlier could be used determine the average number of n_{tx}^{fail} and n_{tx}^{succ}.

E_{tx}^{PHY} is the PHY layer factor on the energy consumption of a Tx-node,
$E_{tx.f}^{MAC}$ is the effect of the MAC protocol on the energy consumption of a Tx-node in the case when transmission fails.
$E_{tx.s}^{MAC}$ is the effect of the MAC protocol on the consumption of energy at the Tx-node when transmission is successful.

$E_{rx}^{PHY} E_{rx}^{MAC}$ are the energy consuming factors of the PHY and MAC layers at the receiving node respectively.

The MAC protocol contains imperfections which cause energy consumption during transmission. A factor called E_{Imp}^{MAC} is included in the calculations to cater for these imperfections whose value is depended on the MAC layer features. For instance, the parameter could represent the consequence of a back-off strategy resulting in idle slots, which are existent in the transmission periods. In an ideal SMAC, there would be no idle slots throughout the period of transmission and, consequently, E_{Imp}^{MAC} would be a zero. For MAC protocols that are competition-free, E_{Imp}^{MAC} could be attributed to the energy consumption overhead triggered by the scheduling of slots and for synchronization.

4. Results

A) Bit Error Probability

Applying Reed Solomon codes to the PHY layer produced the error performance of the transmission link regarding the ratio of energy per bit information to noise power spectral density (Eb/No) was conducted. The results are presented in Figure 2. The Reed Solomon codes are generated as a result of the 6-bit symbol utilisedAccording to the graph, BEP decreases as Eb/No increases and when coding is applied BEP performance improves significantly.

 ISSN: 2957- 7780

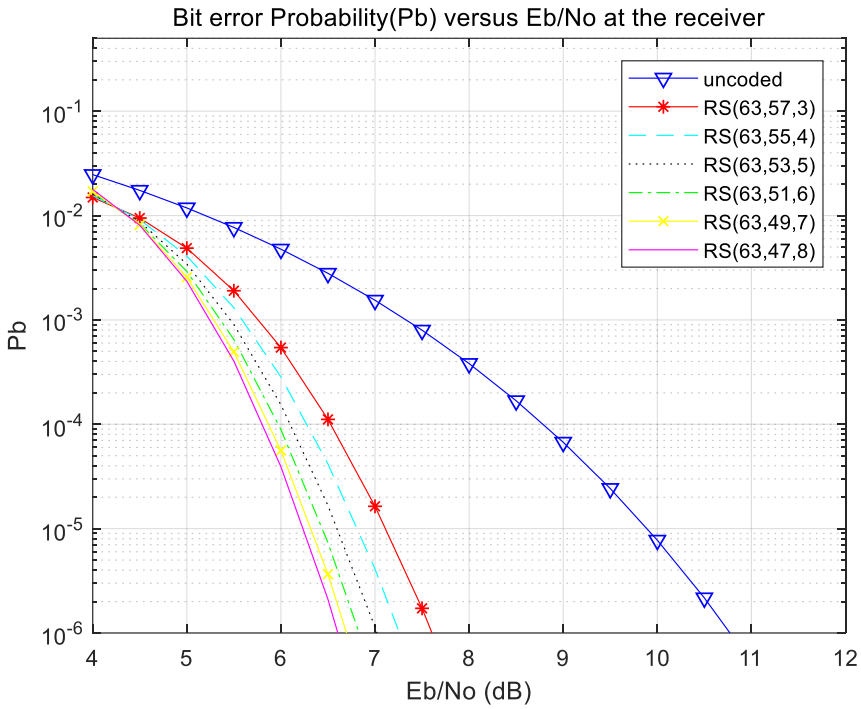

Figure 2: Bit Error Probability versus Signal to Noise Ratio in dB

The expression of bit error rate on the AWGN channel was obtained in reference to the ratio of energy per bit to the single sided noise power spectral density, Eb/No. Coding of the PHY layer introduced extra bits to the data frame, resulting in the reduction of information bits in order to accommodate the redundancy since the length of the data packets is fixed. The performance of the transmission link was evaluated in terms of Eb/No. According to the results in Figure 2, to achieve the desired BER of 10^{-5} the uncoded system required 9.9dB energy per transmitted bit, while the coded scenario resulted in the value reducing to as low as 6.2dB for the RS code 0.75. This is referred to as coding gain, and shows that, for the same performance without coding, the system consumes less energy when coding is applied. Although there is code gain with lower code rates, the rate of code gain decreases as the code rate decreases. This results in a cut-off region where reducing the rate any further does not improve the code gain. The RS codes employed were such that the block length was constant with varied redundancy. According to the performance curve, as the redundancy increases from 3 to 8 the code rate decreases resulting in the BER performance improving, because the error codes become more efficient, thus improving the probability of physical channel access P_{succ}^{PHY} as shown in Figure 2.

B) Packet Success Probability

The probability of successful packet transmission over an AWGN channel is affected when tuning of the MAC layer is considered. The outcomes are presented in Figure 3. The graph shows the

 ISSN: 2957- 7780

effect of jointly tuning the PHY and MAC layer on packet success probability versus only tuning the PHY layer. Three sets of curves that cut off at 1 on the vertical axis represent optimisation of the PHY layer only while the second set of curves that cut off at 0.377 take the MAC layer into account. There is a significant drop in packet success probability when joint layer tuning is applied as it reflects the practical scenario rather than the theoretical ideal.

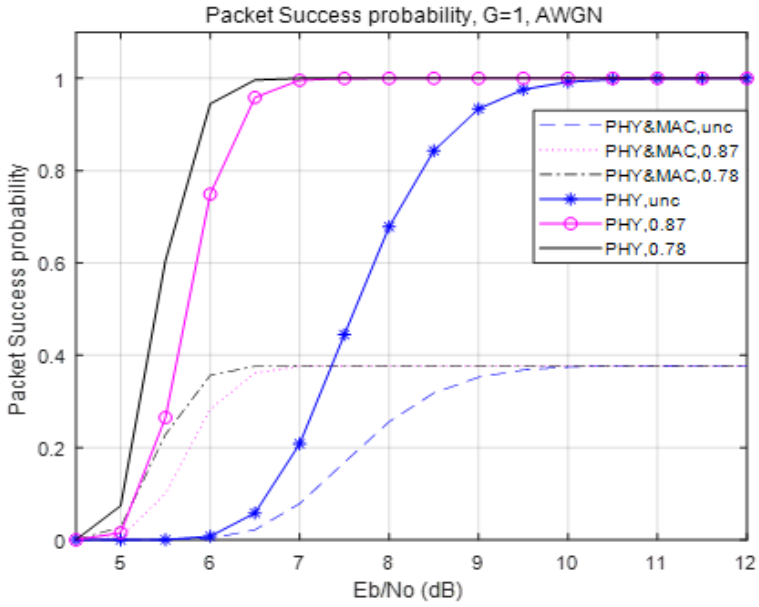

Figure 3: Packet success probabilities vs $\frac{E_b}{N_o}$ in dB for uncoded and coded cases

Packet success probability in wireless networks is the probability of packets being successfully received at the sink node. For an ideal receiver, the MAC layer analysis traditionally does not consider the effect of the probability of transmission in the PHY layer as it is assumed to be one. In this body of work, joint success probability, which incorporates the effects of PHY and MAC layers together, was considered. Figure 3 illustrates the difference between the coded and uncoded scenarios, where the coded case assumes r = {0.87, 0.78} and reflects the impact of joint probability. The curves in Figure 3 labelled "PHY and MAC" at the maximum value one, correspond to the ideal receiver.

Similarly, in the studies of the PHY layer, consideration of the probability of successful channel access in the MAC layer is not considered and is assumed to be one. This corresponds to the curves labelled "PHY". The results in Fig. 3 indicate that, there is a transition state that exists between zero and maximum, within certain values of Eb/No, where the joint success probability of P_{succ}^{PHY} and P_{succ}^{MAC} do not guarantee communication that is error-free at the PHY layer. The results also show that, when $P_{succ}^{PHY} = 1$, that is, the error-free region of the PHY layer, the

ISSN: 2957- 7780

combined packet success probability is 0.368 nonetheless, owing to the S-Aloha MAC characteristics. These results highlight the importance of considering both the MAC and PHY layer probabilities of success.

C) Number of Steps to Absorption

The Markov chain model was employed to calculate the number of steps to absorption, which indicate the value when every sensor node has transferred its packet successfully. In the simulation the same results were obtained as shown in Figure 4. It displays the number of steps to absorption for the coded and uncoded cases. The results are presented for several channel competition probability values, $p = 1/(M-j)$, p = 0.1 and p = 0.05 and are plotted in Figure 4. The value for the number of steps plotted was capped at 500 to provide a tidy graph.

The Markov chain model was applied to determine the number of steps required for each node in the WSN to report its contents to the sink node successfully. The number of steps to absorption is important because it was then converted into time to absorption after finding the duration of every step. Knowledge of the time to absorption allowed for the assessment of the consequence of optimising the physical and MAC layers.

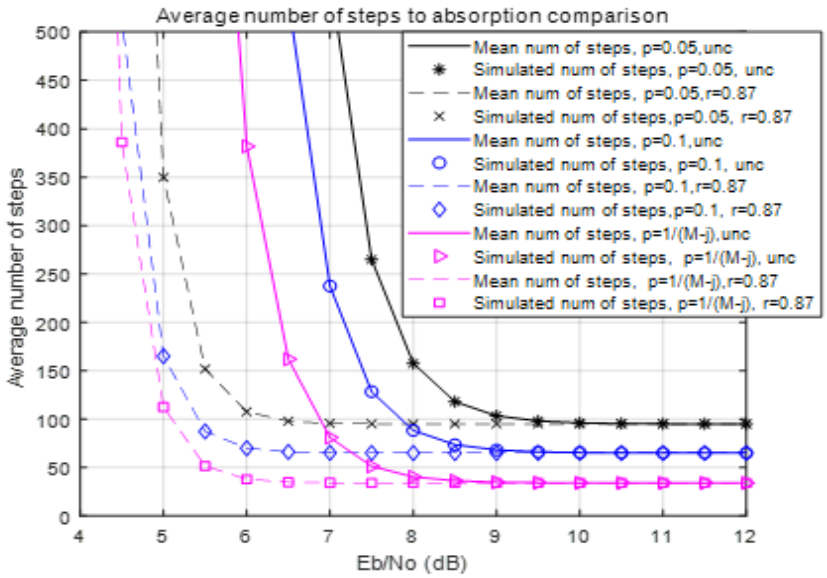

Figure 4: Average number of steps vs $\frac{E_b}{N_o}$ in dB calculated using theoretical and simulation models with different p values.

According to the results obtained, the theoretical model and the MATLAB simulation produce identical results on the average number of steps required to attain absorption as shown in Figure 4. In addition, these results show the effect of the channel competition probability on the average steps to absorption. It can be observed that p = 0.1 has a lower number of average steps to

ISSN: 2957- 7780

absorption compared to p = 0.05. This is because, the latter has less nodes competing in the channel because of the smaller probability and will therefore have more idle steps. The ideal p value is dependent on the number of nodes taking part in competing for the channel. In this research, when the competition period initially begins, the number of nodes contending for a slot, M = 20 and the optimal probability to transmit in this slot, p = 0.05 for the S-Aloha media access control protocol. Nevertheless, during this period of competition the competing nodes decrease in number when nodes begin to transmit and the channel probability of p = 0.05 turns out to be very small. In Figure 3, the observation is that, for the case when G = 1, traffic load is at its optimal for such a network and the average number of steps is minimised where $p = 1/(M - j)$.

D) Energy Saving

The percentage saving in energy for distinct coding rates in contrasted with the energy saving in the transmission of the uncoded case was calculated in this instance. The most energy-efficient code rate could be determined. Energy savings = $E_{TP} - E_{TP,i}$. The results are presented in Figure 5.

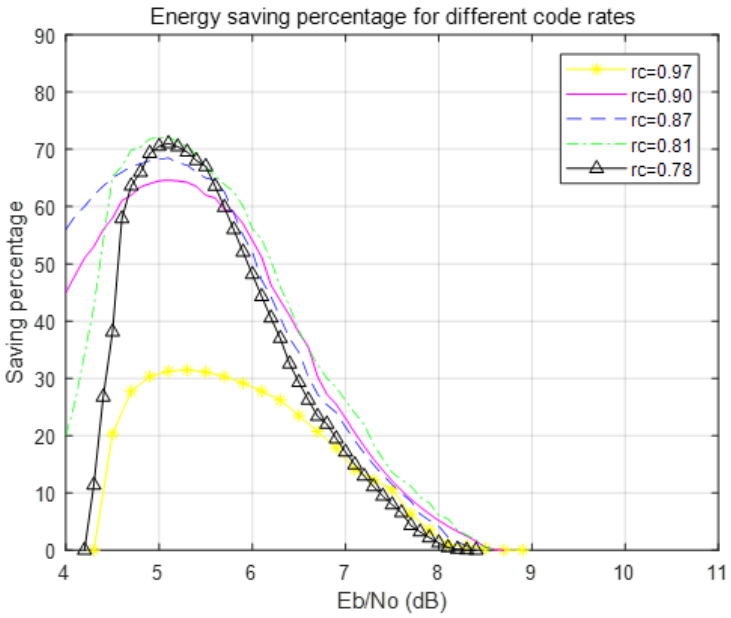

Figure 5: Percentage energy saving result vs $\frac{E_b}{N_o}$ in dB when using different code rates, p = 0.05.

Figure 5 shows that when r = 0.81, that is the code rate which produces maximum energy efficiency, could contribute the energy savings of around seventy nine percent. The weakest code rate r = 0.97, could contribute savings of a maximum of 36% however, it can be observed that this code rate offers energy gains for the broadest range of Eb/No values compared to the other code rates. When the EB/No is greater than 8.5dB the performance for the code rate r = 0.97

ISSN: 2957- 7780

performs more proficiently than the other cases. The results show that for Eb/No values smaller than 8.5dB, the stronger code rates should be employed as they deliver better energy savings.

E) Comparison of MAC Methods

Consumption of energy of the S-Aloha and SMAC media access control protocols in combination with AWGN channel provides. Equation (37) in, Section III. I is used to calculate these results plotted in Figure 6. SMAC outclasses S-Aloha in energy saving performance. However, the percentage savings for Eb/No values greater than 8.5dB drops significantly for SMAC compared to S-Aloha.

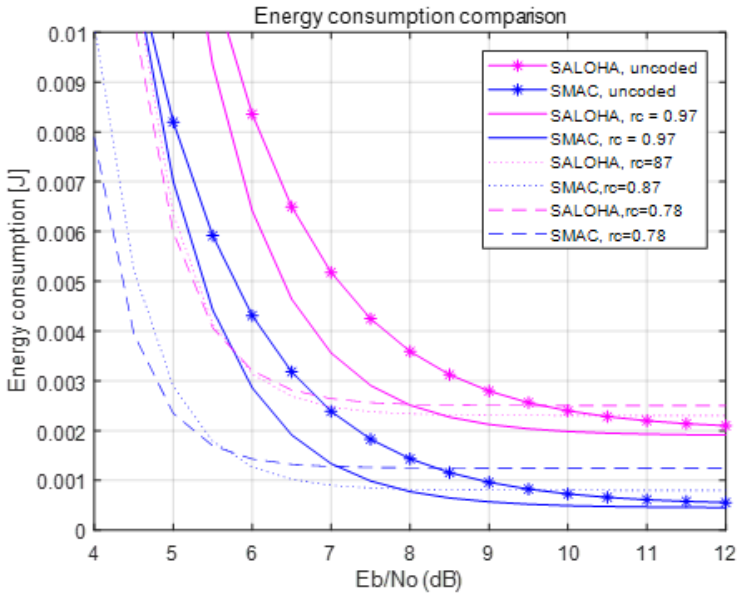

Figure 6: Comparison of energy consumption between S-Aloha and SMAC Medium Access protocols.

In reference to the SMAC protocol, the assumption was that there is perfect synchronisation between the sink node and the sensor nodes, and thus their transmission slots schedule, which would lead to channel access which is collision free. In reference to S-Aloha, the assumption is that there is an optimal slot transmission probability, namely, p = 1/(M-j) for the node. The results show that SMAC surpasses S-Aloha since there aren't any collisions during the competition period, resulting in fewer retransmissions and therefore less energy consumption.

For EB/No values greater than 8.5dB it can be stated that SMAC would lead to almost fifty percent lesser consumption of energy compared to exploiting the S-Aloha protocol. For specific Eb/No values, however, the results show that if strong coding is combined with the S-Aloha protocol, it will lead to decreased energy depletion as compared to a SMAC protocol with weak coding. For example, at Eb/No = 5.6dB, code rates r = 0.87 or r = 0.78 for S-Aloha delivers lower

 ISSN: 2957- 7780

energy utilisation than SMAC with code rate r = 0.97 or when compared with the uncoded PHY layer transmission. Considering that SMAC would entail a bigger control overhead compared to S-Aloha, the variance in energy consumption would be greater in a real-world implementation. The straightforward contrast between S-Aloha and SMAC coupled with AWGN and diverse code rates for error correction, highlight the fact that efficient energy consumption depends on the combined settings of the PHY layer features and the MAC layer attributes.

5. Conclusion

The suggested model was employed to assess the energy efficiency of various Reed Solomon coding rates for a Wireless Temperature Sensor Network using Additive White Gaussian Noise transceivers and S-Aloha Media Access Control. The approach considered the applicable attributes of the PHY and MAC layers that facilitate joint optimisation. This cross-layer scheme could also be utilized for the analysis of energy efficiency of different permutations of PHY and MAC protocols. This research study used SMAC to compare the energy efficiency of the two different MAC protocols. The results obtained from this research showed that by choosing the appropriate code rate for the PHY layer and channel specifications for the MAC layer, substantial savings in energy could be accomplished. Within specific settings in this research, the energy gains were over 75% for a specific code rate in comparison to the circumstance where no coding was applied. On the other hand, according to the results, there are some instances where applying a code rate does not result in energy saving, in comparison to the case where no coding is used.

The proposed cross-layer tuning model in this research can be used at the network implementation phase for code rate selection or can be computed adaptively during runtime with the right technology, that is, sensor nodes with strong computational capabilities. If the probable channel conditions are identified, the optimum code rate could be determined at the network planning stage. The model could also be utilised for assorted error coding schemes or to investigate the effect of transmission power or the modulation on the cross-layer operation. The model could be used on mobile sensor nodes on a random network topology.

References

[1] H. Karl and A. Willig, “Protocols and Architectures for Wireless Sensor Networks, Hoboken, NJ: Wiley, 2007, pp. 18-44.

[2] W. Dargie and C. Poellabauer, 'Fundamentals of wireless sensor networks', Chichester, West Sussex, U.K.: Wiley, 2010, pp 133-153.

[3] P. Charan, R. Paulus, M. Kumar and A. Jaiswal, 'A Cross Layer approach for Performance Optimization in Wireless Sensor Networks using Cooperative Diversity', International Journal of Computer Science & Technology, vol. 3, no. 2, pp. 158-163, 2012.

[4] M. Li, Y. Jing, C. Li 'A Robust and Efficient Cross-Layer Optimal Design in Wireless Sensor Networks', Wireless Personal Communications, vol 72, no. 4, pp. 1889-1902, 2013.
[5] H. Chao, C. Chang, C. Chen and K. Chang, 'Survey of Cross-Layer Optimization Techniques for Wireless Networks', *Wireless Technologies*, pp. 60-76.
[6] S. Shabdanov, P. Mitran and C. Rosenberg, 'Cross-Layer Optimization Using Advanced Physical Layer Techniques in Wireless Mesh Networks', *IEEE Transactions on Wireless Communications*, vol. 11, no. 4, pp. 1622-1631, 2012.
[7] B. Fu, Y. Xiao, H. Deng and H. Zeng, 'A Survey of Cross-Layer Designs in Wireless Networks', *IEEE Communications Surveys & Tutorials*, vol. 16, no. 1, pp. 110-126, 2014.
[8] Z Chen, S Li, "An Energy-Efficient Access Control Algorithm with Cross-Layer Optimization in Wireless Sensor Networks". Wireless Sensor Network, vol 2, no. 2, pp. 168-172, 2010.
[9] H. Karvonen, C. Pomalaza-Raez and M. Hamalainen, 'A Cross-Layer Optimization Approach for Lower Layers of the Protocol Stack in Sensor Networks', ACM Trans. Sen. Netw., vol. 11, no. 1, pp. 1-30, 2014.
[10] IEEE, 'IEEE Standard for Information Technology—Telecommunications and Information Exchange Between Systems—Local and Metropolitan Area Networks—Specific requirements Part II: wireless LAN medium access control (MAC) and physical layer (PHY) specifications IEEE Std 802.11g', 2007.
[11] S. Kulkarni, A. Iyer and C. Rosenberg, 'An address-light, integrated MAC and routing protocol for wireless sensor networks', IEEE/ACM Transactions on Networking, vol. 14, no. 4, pp. 793-806, 2006.
[12] T. Shu and M. Krunz, 'Energy-efficient power/rate control and scheduling in hybrid TDMA/CDMA wireless sensor networks', Computer Networks, vol. 53, no. 9, pp. 1395-1408, 2009.
[13] J. Choi, H. Kim, I. Baek and W. Kwon, 'Cell based energy density aware routing: a new protocol for improving the lifetime of wireless sensor networks', Computer Communications, vol. 28, no. 11, pp. 1293-1302, 2005.
[14] F. Aron, T. Olwal, A. Kurien and M. Odhiambo, 'Energy Efficient Topology Control Algorithm for Wireless Mesh Networks', in International Wireless Communications and Mobile Computing, 2008, pp. 135-140.
[15] Y. Yuan, Z. Yang, Z. He and J. He, 'An integrated energy aware wireless transmission system for QoS provisioning in wireless sensor network', Computer Communications, vol. 29, no. 2, pp. 162-172, 2006.
[16] I. Akyildiz, M. Vuran and O. Akan, 'A Cross-Layer Protocol for Wireless Sensor Networks', in Information Sciences and Systems, 2006 40th Annual Conference, Princeton, 2006, pp. 1102-1107.
[17] S. Yessad, L. Bouallouche-Medjkoune, and D. Aïssani, "A cross-layer routing protocol for balancing energy consumption in wireless sensor networks," *Wireless Personal Communications,* vol. 81, no. 3, pp. 1303-1320, 2015.
[18] H. Yetgin, K.T.K. Cheung, M. El-Hajjar and L Hanzos, 'Cross-Layer Network Lifetime Maximization in Interference-Limited WSNs', IEEE Transactions on Vehicular Technology, vol. 64, no. 8, 2015, pp. 3795 - 3803
[19] Y. Zhou, Z. Sheng, C. Mahapatra, V. C. Leung, and P. Servati, "Topology design and cross-layer optimization for wireless body sensor networks," Ad Hoc Networks, vol. 59, pp. 48-62, 2017.
[20] G Bianchi, "Performance Analysis of the IEEE 802.11 Distributed Coordination Function". IEEE Journal on Selected Areas in Communications, vol 18, no. 3, pp. 535-547, 2000.
[21] Y Zhang, C He, L Jiang, "Performance Analysis of S-MAC Protocol under Unsaturated Conditions". IEEE Communications Letters, vol 12, no. 3, pp. 210-212, 2008.
[22] Y Wang , M Vuran , S Goddard, "Cross-Layer Analysis of the End-to-End Delay Distribution in Wireless Sensor Networks". IEEE/ACM Transactions on Networking, vol 20, no. 1, pp. 305-318, 2012.

[23] Y. Ma and C. Ma, 'Introduction of FECs and its Applications on Internet & Wireless Communications', *Advanced Materials Research*, vol. 403-408, pp. 1776-1780, 2011.

[24] F. R. Lone, A. Puri and S. Kumar, 'Performance Comparison of Reed Solomon Code and BCH Code over Rayleigh Fading Channel', International Journal of Computer Applications, vol.71, no. 20, pp. 23-26, June 2013

[25] D. V. Ratnam, S. SivaKumar, R. Sneha, N. S. Reddy, P. S. Brahmanandam and S, G. Krishna, 'A Study on Performance Evaluation of Reed Solomon (RS) Codes Through an AWGN Channel Model in a Communication System', International Journal of Science and Communication, vol 3, no. 1, pp. 37-40, 2012.

[26] S. Kumar and R. Gupta, 'Bit Error Rate Analysis of Reed Solomon Code for Efficient Communication System', International Journal of Computer Applications vol. 30, no.12, pp.11-15, September 2011.

[27] M. Abdelfatah Abdeltwab, K. ElBarbary and A. Elhenawy, 'Performance Improvement of Coded OFDM Communication System in AWGN Channel', International Journal of Computer Applications, vol. 110, no. 11, pp. 17-23, 2015.

[28] V. Korrapati, M. Prasad, D. Reddy and G. Tej, 'A Study on performance evaluation of Reed Solomon Codes through an AWGN Channel model for an efficient Communication System', International Journal of Engineering Trends and Technology (IJETT), vol. 4, no. 4, pp. 1038-1041, 2013.

[29] S. Usha and K. Nataraj, 'BER Performance of Digital Modulation Schemes with and Without OFDM Model for AWGN, Rayleigh and Rician Channels', International Journal of Science and Research (IJSR), vol. 4, no. 11, pp. 330-335, 2015.

[30] D. Xu and K. Wang, 'Stochastic Modeling and Analysis with Energy Optimization for Wireless Sensor Networks', *International Journal of Distributed Sensor Networks*, pp. 1-5, 2014.

[31] Y. Wang, M. Vuran and S. Goddard, 'Stochastic Analysis of Energy Consumption in Wireless Sensor Networks', in *7th Annual IEEE Communication Society Conference on Sensor, Mesh, and Adhoc Communications and Networks (SECON)*, Boston, MA, pp. 1-9, 2010

Optimum Phasor Measurement Unit Placement on Power System Grid: Case Study of Kenyan Western Region Power Network.

E. A. Nyonje[1*], M. J. Saulo[2], E. Ataro[1], E. Okendo[1]

[1]Department of Energy and Power Engineering, Technical University of Kenya

[2]Department of Electrical Engineering, Technical University of Mombasa,

[*]Corresponding author: edwardatanga2008@yahoo.com

Article History
Submission Date: 12th April 2024
Acceptance Date: 11th May 2024
Publication Date: 30th June 2024

Abstract

In Kenya, power system facilities are experiencing an old age crisis, with it comes an outdated monitoring equipment, that is, Supervisory Control and Data Acquisition System (SCADA), which is inadequate. Phasor Measurement Unit system, (PMU) is a technology which ensures reliability through efficient monitoring. The essence of this technology is its capacity to deliver synchronized measurements of power elements at practically real time. In Kenya and most sub-Saharan African countries, use of PMU technology is limited due to its high capital cost. To reduce this cost, there is need to come up with optimum means of PMU placement within power system network in order to achieve as minimal quantity of PMUs as possible while achieving maximum observability. The authors are proposing the optimum PMU placement (OPP) on Kenya Power Transmission Network (Western Region on a 39 – bus system) expending a Hybrid Algorithm method of the Particle Swarm Optimization and the Artificial Bee Colony. This hybrid algorithm executed on IEEE – 14 and 39 – bus test bench then will be implemented to Kenyan's power network, western region 39- bus system. These particular case studies are modelled on the Power System Analysis Toolbox (PSAT) and simulation done in the MATLAB. Simulation results obtained provides optimum solution of 18 PMU situated on buses; 3, 6, 7, 10, 11, 13, 16, 18, 20, 23, 26, 28, 30, 31, 32, 33, 34, and 36 for maximum observability.

Key words; The Phasor Measurement Unit (PMU), Global Positioning System, the Supervisory Control and Data Acquisition System (SCADA), Observability, Power System Analysis Toolbox (PSAT), Particle Swarm Optimization and the Artificial Bee Colony.

1. Introduction

With current dependency on power grid, a 30 minutes electrical power grid instability is an economical suicide, one-hour power grid instability is a disaster and anything above one-hour grid loss is an economic catastrophe. A faulty power protection system is too dangerous for any electrical grid. Kenya recently on 25th August, 2023 lost entire power grid for a good 15 hours, an occurrence which is unacceptable in the 21st century for a country full of Engineers and academic researchers. This grid loss effect was equally felt by the neighboring East Africa Countries, Uganda and Tanzania included. The Cabinet Minister for Energy could not explain the cause of major power grid failure three days after the total shutdown.

Kenya power system protection uses the SCADA system for its system control and management. With application of Remote Terminal Units, the SCADA system is used for data collection from electrical relays, current transformers (CT) and voltage transformer (VT). Major downside of the currently used SCADA system is, it offers asynchronous measurements at slow data rate that leads to poor monitoring of the power grid and resulting in inability to flag minute disturbances which usually cascade to cause major system shut down. The Kenya's grid shut down can be compared with power failure occurrence in North America in 2003[3] that caused a historical extensive power failure which affected millions of residence in both America and Canada just like the entire Kenya Nation faced prolonged blackout and its two neighboring countries equally suffered the fate.

The US power outage post analysis indicated that the fault was cascaded because there was a phase difference between two regions, that is, Western Michigan and Cleveland. It took time to identify this for the sole reason that there was no efficient technology to monitor phase shifts effectively, a thing PMU technology now handle effectively. To improve power system protection, the SCADA system should be replaced by a modern monitoring unit like Phasor Measurement Unit (PMU). PMU technique is very essential to power utility Engineers as it allows them to monitor, identify and correct electrical power faults incase variation from normal operations are realized.

The PMU measure the magnitude and phase angle of electrical signal voltage, current, frequency and rate of change of (RCF), these components are usually time stamped using global positioning system (GPS) for real time monitoring. However, PMU devices are very expensive thus it is not practical that they be installed in all buses in the electrical power system. Subsequently, optimal PMU placement (OPP) method was developed to realize minimum

 ISSN: 2957- 7780

possible number of PMUs that can be used for maximum observability of an electrical power utility while minimizing on cost of their installation and ensuring efficiency.

The advantages of the PMU compared to SCADA system has been out washed by its costs implication, it is very expensive to install PMUs in all the buses in an electrical network and this made Engineers to find a way in which optimal placement can be achieved through use of minimal number of PMU possible with maximum observability.

According to previous research work on optimization, there exists various methods applied to acquire optimum PMU placement for maximum power system observability. [4] Presents review on PMU placement methods considering mathematical programming, a heuristic and Meta-heuristic approaches. These approaches includes but not limited to Depth First Search (DeFS)[5] and Minimum Spanning Tree (MST), in Metaheuristic, Simulated Annealing (SA), Genetic Algorithm (GA), the Tabu Search (TS) and Differential Evolution is mentioned[6]. [7] Expounds on Genetic Algorithm as a means to achieve optimal PMU optimization and allocation for maximum observability of a power system, it further state that modelled system can be efficiently used in PMU allocation in any network. In [8], Carousal Genetic Algorithm has been proposed which is a development from the traditional Genetic Algorithm used for optimal PMU placement method[9]. A very interesting algorithm in Artificial Bee Colony (ABC) was implemented in a Kenya Power system, Nairobi region to achieve maximum optimization. The authors placed more interest on the System Observability Redundancy Index (SORI) which was considered to operate under normal baseload condition using Zero Injection Bus and without Zero Injection Bus [10]. In [11], the authors brings out the short coming of the conventional algorithms which includes; enslavement on central initialization, sluggish convergence, local optima trap among others. They suggest that since Artificial Bee Colony have intelligent foraging behavior, it minimaxes these short coming. In [12][13], hybrid optimization method is introduced where a particle swarm optimization and Tabu search is used towards achieving optimization. [14] Employs use of exhaustive search (ES) which was believed to offer stronger results compared to its predecessors. While considering power system redundancy with its reliability in consideration, Mixed Integer Linear Programming (MILP) was put in use by [15]. [16] Emphasis on application of a binary search algorithm to achieve required minimum number of PMUs to obtain maximum observability on an electrical system.

 ISSN: 2957- 7780

In Kenya power transmission network, western region network is critical as it has power generation sources tapped to the grid and any instability in one of its generation source may cause grid instability in the entire Country and by extension, region. It is crucial to put measures that ensures the network is stable at all times and the advanced monitoring system at the moment is PMU. In Kenya, the PMU modelling work has only been done to Kenya Power System, Nairobi Region, this particular research work presents a proposed Optimum PMU placement (OPP) on Kenya Power system, Western region 39 – bus system using a hybrid algorithm of Particle Swarm Optimization and an Artificial Bee Colony. The algorithm developed is executed on an IEEE – 14 and 39 – bus test bench, thereafter being applied to the Kenya Power Network system (Western region 39 – bus system). The actual modelling is done using a Power System Analysis Toolbox (PSAT), and simulation done in a MATLAB.

Based on the research work done previously, this paper tends to explore the hybrid Metaheuristic of the Particle Swarm Optimization algorithm and an Artificial Bee Colony in order to achieve optimum placement while considering converging time. The selection of PSO-ABC resulted from the unique characteristic of the two algorithms enable recombination. ABC is capable of optimizing larger systems, this assists PSO to obtain local minima in larger systems something PSO cannot achieve on its own. Equally, the fairly prompt convergence speed of the PSO significantly reduce interval taken by an ABC in the triple search sequence.

The Optimum PMU Placement problem formulation is undertaken by application of prevailing method, that is, depth-first method and then the hybrid of particle swarm optimization (PSO) and artificial bee colony (ABC). The new method is first applied on the IEEE standard buses; IEEE – 14 and IEEE – 39 bus systems for verification, then implemented on Kenya Power Network system, Western region 39 – bus system.

Kenya Power Western region 39-bus system is a use of authenticated method based on IEEE – 39 standard bus system.

Thus, the remaining portion of this paper is as follow; the power systems observability and PMU placement rules is covered in section 2, Section 3 explains proposed methods whereas in section 4, case studies has been elaborated and in 5 section discussion of the results obtained is undertaken. Last part is section 6 which concludes this paper.

2. Basic rules for power system observability and PMU placement

 ISSN: 2957- 7780

In order to obtain maximum power system observability, the common method employed is topological and numerical methods. Topological observability method obtains details on power system network connectivity, PMUs location and measurement types using logical while numerical observability method derive its information from a measurement matrix gain or factorization of Jacobian matrix. For optimum PMU placement problem, the paper applies a topological method.

It is important to note that for an observability to be obtained, the voltages of all the buses within the network system need to be known, this requirement is essential. The interesting part of the PMU placement phenomenon is that the measurement of the voltage and branch current can be taken directly by the installed PMU on a particular bus or indirectly applying other known parameters on the neighboring connected buses. The phenomenon enables all buses within the network to be observable if required number of PMUs are located strategically in a power system.

Below are the rules used for topological observability;

(i) In direct measurement, voltage at a bus containing a PMU and the current of all incident branches to that particular bus containing the PMU are all known.

(ii) Any PMU installed bus always have its voltage phasor and all branch current phasors connected to it directly be measured by the installed PMU on the said bus.

(iii) Availability of the voltage and branch current at the end of the line containing the PMU is known, the voltage at the unknown voltage at the other side which does not have the PMU installed bus can be calculated.

(iv) Where voltages at both ends of a bus are known, the currents between the two buses in consideration can be calculated by applying Ohm's law.

2.1 Optimum PMU Problem Formulation

Main purpose of the OPP is to obtain minimum possible quantity of PMUs required in a power system network in order to attain sustainable running and implementation cost involved. Optimum objective function formulation is as follows;

$$F = min \sum_{i=1}^{N} P_i X_i \quad (1)$$

Whereas;

F Refers to an objective function for optimum PMU placement

P_i Refers to the PMU price at bus i;

 ISSN: 2957- 7780

$$x_i = \begin{Bmatrix} 1 & if\ PMU\ is\ availble\ at\ bus\ i \\ 0 & if\ no\ PMU\ availble\ at\ bus\ i \end{Bmatrix} \quad (2)$$

N; Represents the total buses presents in a system network;

P_i ; Represent the cost price of the PMU at bus i;

Objective function F, is exposed to the observability constraint in Eq. (3) which guarantees every individual bus observability.

$$F_i = \sum_{i=1}^{N} a_{ij} x_{ij} \geq A \quad (3)$$

Where;

F_i Represents the constraint being observed on every individual bus connected with PMUs;

$$F_i = \begin{Bmatrix} \neq 0 & if\ bus\ i\ is\ observable \\ = 0 & if\ bus\ i\ is\ unobservable \end{Bmatrix} \quad (4)$$

A Is a vector of size N whose elements area are all 1;

a_{ij} Represents binary connectivity matrix of the network below;

$$a_{ij} = \begin{Bmatrix} 1 & if\ i = j \\ 1 & if\ buses\ i\ and\ j\ are\ connected \\ 0 & if\ bus\ i\ and\ j\ are\ not\ connected \end{Bmatrix} \quad (5)$$

2.2 The system observability redundancy index (SORI)

System observability redundancy index (SORI) refers to the total number of buses being covered optimally by the PMUs in a power system. When SORI is high, it gives an indication of reliable PMU monitoring system. The authors use SORI in determining which algorithm provides the highest redundancy measurement. Below is the SORI computation as presented in Eq. 6.

$$SORI = \sum_{i=1}^{N} a_{ij}\, x_{PMU} \quad (6)$$

Whereas;

$SORI$ Represents the sum total number of buses in the power system network.

a_{ij} Gives representation of the binary matrix connectivity;

x_{PMU} Gives optimum PMU placement in a network that offers maximum observability;

ISSN: 2957- 7780

Figure 1 presents a 14 – bus network topology used for OPP problem solution and the matrix connectivity is presented in eq. (7)

$$A = \begin{vmatrix} 1&1&0&0&1&0&0&0&0&0&0&0&0&0 \\ 1&1&1&1&1&0&0&0&0&0&0&0&0&0 \\ 0&1&1&1&0&0&0&0&0&0&0&0&0&0 \\ 0&1&1&1&1&0&1&0&1&0&0&0&0&0 \\ 1&1&0&1&1&1&0&0&0&0&0&0&0&0 \\ 0&0&0&0&1&1&0&0&0&0&1&1&1&0 \\ 0&0&0&1&0&0&1&1&1&0&0&0&0&0 \\ 0&0&0&0&0&0&1&1&0&0&0&0&0&0 \\ 0&0&0&1&0&0&1&0&1&1&0&0&0&1 \\ 0&0&0&0&0&0&0&0&1&1&1&0&0&0 \\ 0&0&0&0&0&1&0&0&0&1&1&0&0&0 \\ 0&0&0&0&0&1&0&0&0&0&0&1&1&0 \\ 0&0&0&0&0&0&0&0&0&0&0&1&1&1 \\ 0&0&0&0&0&0&0&0&1&0&0&0&1&1 \end{vmatrix} \quad (7)$$

From eq. (8) it can be seen that when observability constraints are exposed to the objective function, then, it is clear from Eq. 7 that at least one variable from the constraints must be positive (digital 1). Take an example of bus 4, its observability is achieved by placing a PMU on at least one of the buses; 2, 3, 4, 5, 6, and 9. Similar to that of bus 9, the observability is achieved by placing a PMU in at least one of the buses; 12, 13, and 14.

$$PO_1 = lb_1 + lb_2 + lb_5 \geq 1$$

$$PO_2 = lb_1 + lb_2 + lb_3 + lb_4 + lb_5 \geq 1$$

$$PO_3 = lb_2 + lb_3 + lb_4 \geq 1$$

$$PO_4 = lb_2 + lb_3 + lb_4 + lb_5 + lb_6 + lb_8 \geq 1$$

$$PO_5 = lb_1 + lb_2 + lb_4 + lb_5 + lb_6 \geq 1$$

$$PO_6 = lb_5 + lb_6 + lb_{11} + lb_{12} + lb_{13} \geq 1$$

$$PO_7 = lb_4 + lb_7 + lb_8 + lb_9 \geq 1 \quad (8)$$

$$PO_8 = lb_7 + lb_8 \geq 1$$

$$PO_9 = lb_4 + lb_7 + lb_9 + lb_{10} + lb_{14} \geq 1$$

$$PO_{10} = lb_9 + lb_{10} + lb_{11} \geq 1$$

$$PO_{11} = lb_6 + lb_{10} + lb_{11} \geq 1$$

$$PO_{12} = lb_6 + lb_{12} + lb_{13} \geq 1$$

ISSN: 2957- 7780

$$PO_{13} = lb_{12} + lb_{13} + lb_{14} \geq 1$$

$$PO_{14} = lb_{9} + lb_{13} + lb_{14} \geq 1$$

Where;

PO Is the PMU observability

lb Is the bus location

3. Proposed method

3.1 Particle Swarm Optimization

PSO as the name depicts operates based on particle movement, swarm moving from one point to another and to make choices on the best route through linear and vector control. PSO was developed by Kennedy and Eberhart after exploring prior principle of optimization by swarm like bird flocking or fish schooling[17][18].

Particle swarm optimization operates on population principle where particles $e_i = (e_{i,1}, e_{i,2}, \dots, e_{i,n}), i = 1,2, \dots, Sn.$ this equation distributes the population uniformly across the search area. In PSO, particles represent solutions and each particle is considered to offer a potential solution of an optimized system. When the solution is obtained from a particle, velocities of the particle are updated through self-best and global best solution from the previously achieved. This can be mathematically represented as;

$$v_i^j(q+1) = \omega v_i^j(q) + c_1 * r_1 * [p_{i,j}^{best}(q) - x_q^j(q)] + c_2 * r_2[g_j^{best}(q) - e_i^j(q)], \quad 10$$

Where $v_i(q+1)(-vmax \leq v_i(q+1) \leq v \max)$ represents the rate at which position of the particles changes and c_1 and c_2 are the two learning variables that controls the effect of the social and cognitive components e_1 $(i = 1,2)$ and random numbers in the range [0, 1] and ω is the inertia weight that enables the convergence of the PSO algorithm[12].

3.2 Artificial Bee Colony

This algorithm is a type of algorithm which explores a certain behavior of bees, that is, it imitates the process the honey bee follows in its operations to obtain food for the queen. It consists of three category of bee group namely, employed, onlooker and scout bees[11]. Employed bee is given the responsibility of searching for accessible sources of food and acquiring information about accessible food sources, information that is passed to onlooker

 ISSN: 2957- 7780

bees[19]. From the information, onlooker bees select superior food source from the food pull. If the onlooker bees decide that the food quality is not the best, it will be deserted by an employed bee. ABC algorithm presents every food source as potential solution to an optimization problem and the food source is evaluated by the fitness value of the potential solution. The number of employed bees is usually equal to the number of food source.

3.3 Employed bee point

Here the bee searches the neighboring locality of the current food source location. If search bore a new a new better food source location, it replaces the old food location. To evaluate the fitness function, Eq. (11) is used

$$fitness_i = \begin{matrix} {}^{1}/_{1+FF_i} & if\ FF_i \geq 0 \\ 1+FF_i & if\ FF_i < 0 \end{matrix} \quad 11$$

Where FF is fitness function.

The next step is to determine the parameters that need to be changed such that neighboring food source selected and the present value are not similar, then velocity of food source is computed and updated as depicted in Eq. 12 and Eq. 13

$$v_{ij} = e_{ij} + \varphi_{ij}(e_{ij} - e_{kj}) \quad 12$$

$$e_{i,d} = e_d^{min} + r(e_d^{max} - e_d^{min}) \quad 13$$

Where i represents the employed bee, j represents random index, k represents the random neighboring index to i and φ is the random number between 0 and 1. R is an actual number ranging between 0 and 1 and d is the problem space dimension with minimum and maximum limits[20].

3.3.1 Onlooker bee point

Results achieved by the employed bees is scrutinized and the higher probability on the new food source is designated as the new food source. This new food source proceeds to the global best solution.

$$p_i = \frac{fit\ (x_i)}{\sum_i^{S_n} fit\ (x_i)} \quad 14$$

Where fit (x_i) indicates the suitability of i^{th} food source

S_n Represents population size of the food source.

 ISSN: 2957- 7780

If onlooker bee determines that the new food source is superior to the previously settled on food source, employed bee takes record of the new position and the trial counter is reset by increasing it to 1[20].

3.3.2 Scout bees point

Under scout bee step, the next food source is sourced without reference to previous records and the incremental steps of the iterations counter.

3.4 Hybrid of the algorithm

A hybrid algorithm is achieved by a combination of two or more algorithms. In this case, a hybrid of particle swarm optimization (PSO) and artificial bee colony (ABC) is put into use to obtain Optimal PMU Placement on the three bus systems. This proposed hybrid optimization is established on recombination of two algorithms, that is, PSO and ABC. ABC has better ability in search for global optimum but it does not utilize the global best solution directly since it stores the global best solution at every level of iteration. Particle swarm optimization has the capability that directly utilizes global best solution at every level of iteration. To improve on both the algorithms functionality and overcome individual weaknesses, this research is proposing the recombination procedure between PSO and ABC.

Under the hybrid, at the termination of the ABC process, PSO algorithm takes over the process as indicated in Eq. 15 and Eq. 16.

$$v_{new}(t) = \omega_1 v_{old}(t-1) + c_1 r_1 (E_{best} - E_{old}) + c_2 r_2 (G_{best} - E_{old}) \quad 15$$

$$E_{new}(t) = E_{old}(t-1) + v_{new}(t) \quad 16$$

Where v_{new} and e_{new} represents a new food source velocity and position respectively.

ω Represents inertia weight.

c_1 and c_2Represents acceleration coefficients.

r_1 and r_2 are random numbers.

E_{best} represents best position of a food source.

G_{best} is global position of food source

The final result achieved after recombination is represented in the equation 17.

$$PO = \begin{cases} E_{new}(t), & Run\ ABC\ until\ its\ end \\ v_{new}(t), & PSO\ takes\ over \\ 0, & If\ conditions\ are\ not\ met \end{cases}$$

 ISSN: 2957- 7780

The data used in this hybrid metaheuristics algorithm is obtained from power system analysis toolbox (PSAT).

Figure 1 presents flow chart hybrid algorithm applied in this optimization. In the flow chart diagram, the recombination algorithm method of PSO – ABC is elaborated. A solution is created which can be termed the greatest best. This greatest best is the gbest of the PSO and the neighbor of the onlooker bees for the ABC [21] for the algorithm to achieve the greatest best.

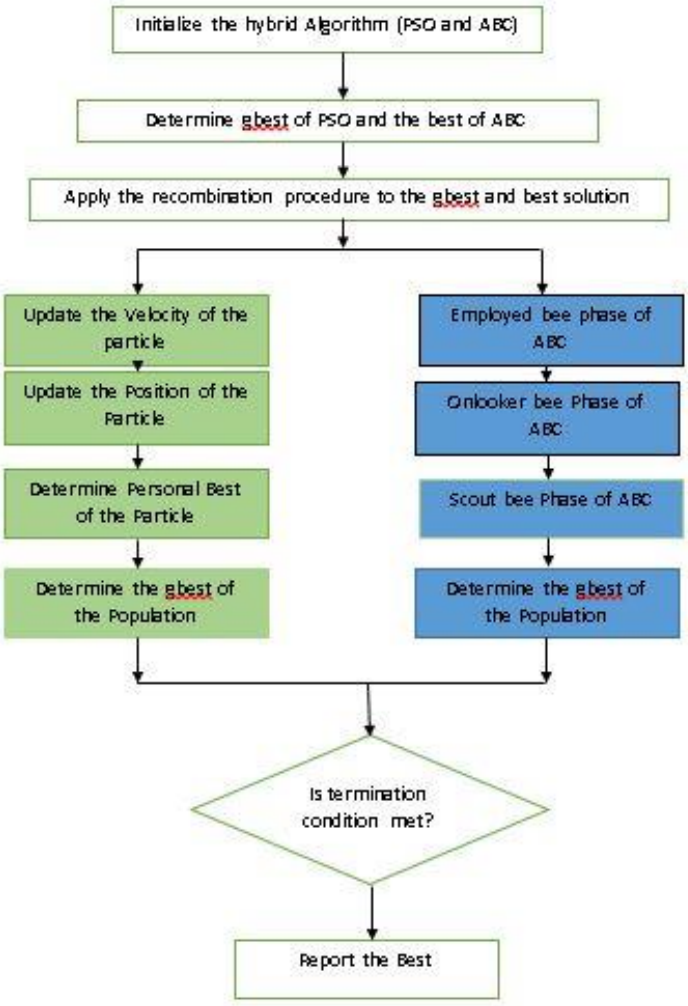

Figure 1: The flow chart hybrid algorithm used for optimization

4. Case studies

Consideration is given to the three network systems, IEEE – 14 bus system, IEEE – 39 bus system, Kenya Power Western Region System which is a 39 – bus system and is composed of both 132KV and 220 KV lines. IEEE – bus was selected to enable study and in-depth analysis

 ISSN: 2957- 7780

of power system behavior on MATLAB and PSAT tool box. It further influenced the problem formulation in the article which is used for IEEE – 9 bus system and the Kenya Power western region – 39 bus system analysis and comparison. Since the research considers Kenya Power system, western region which is a 39 – bus system, this informed the decision to select IEEE 39 – bus system for a case study in order to provide a bench mark to our research .It is assumed that the operating conditions in both IEEE 39 – bus system is similar to those of Kenya Power Western Region conditions. Data used in modelling was acquired from the Kenya Power and lightening company. Kenya Power and lightening company is the main power utility in Kenya. Power System Analysis Toolbox (PSAT), a MATLAB toolbox critical in power system analysis and simulation is used in the simulation to obtain the results. The generation units are modelled as standard PV buses considering reactive power limits and the loads are modelled by constant PQ loads[10]. To help in PMU location, the PSAT generates graph representation. Figures 2, 3, 4 ,5,6,7 and 8 below present the models and graphical representation of the case studies;

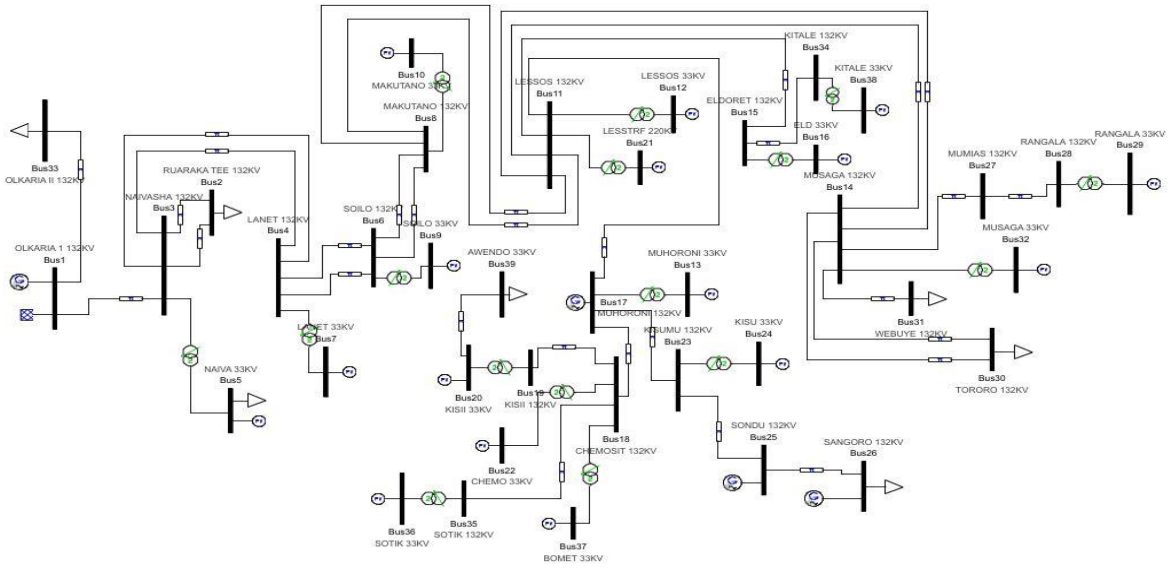

Figure 2: Kenya Power Western Region 39 Bus system without PMU

 ISSN: 2957- 7780

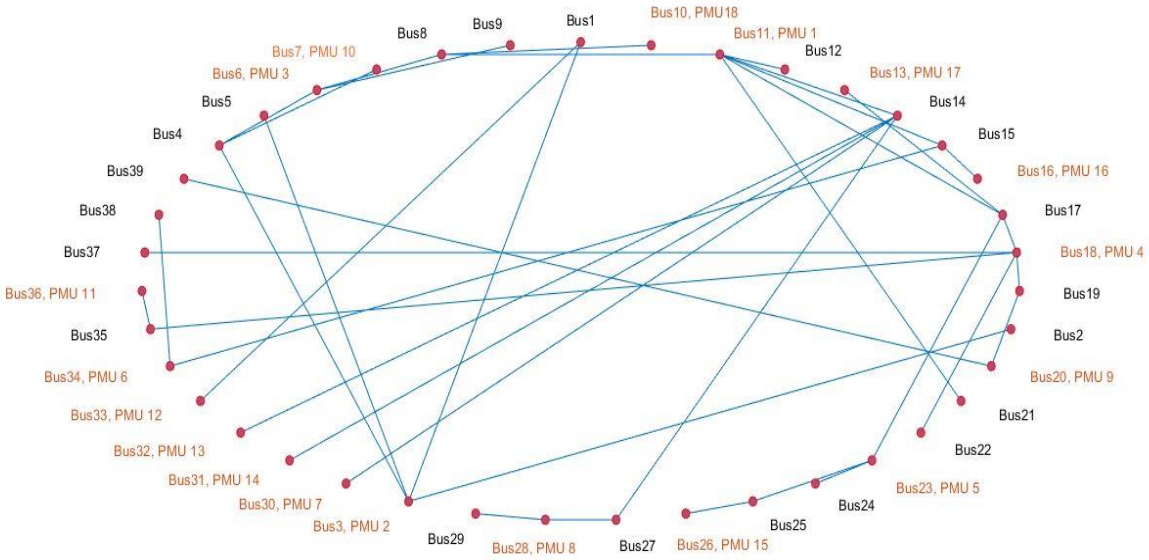

Figure 3: Kenya Power Western Region 39 Bus system graph representation of PMU location using PSO-ABC.

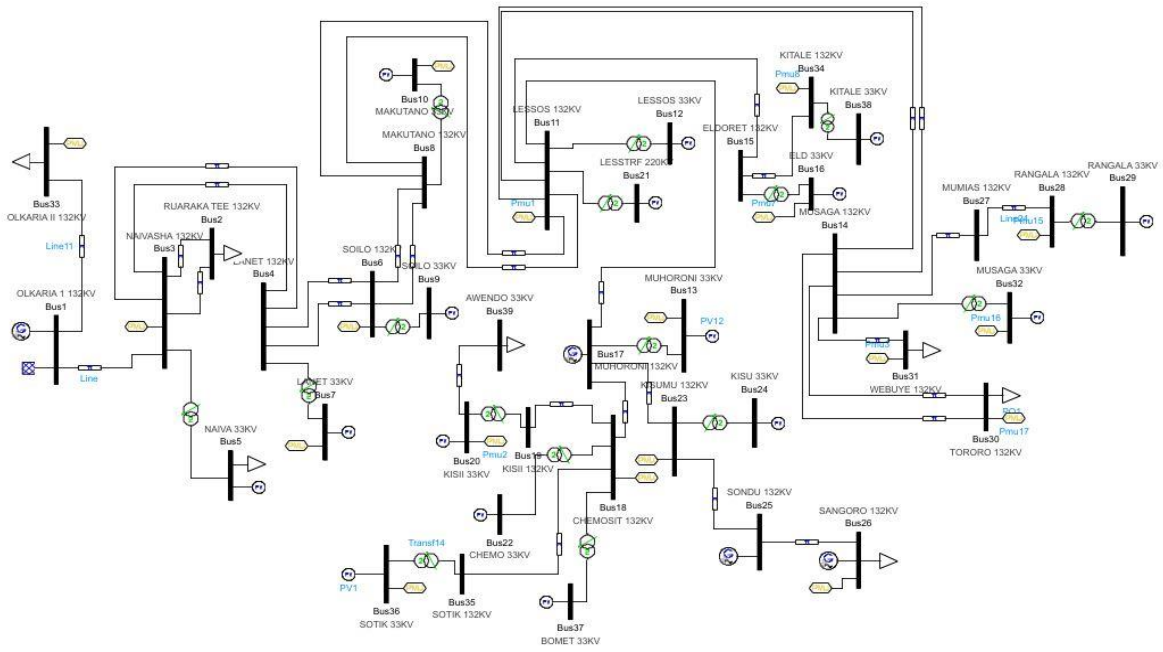

Figure 4: Kenya Power Western Region 39 Bus system with PMU placement using PSO-ABC.

5. Simulation results

In this part, simulation results from MATLAB are availed and discussed for the case study bus systems using proposed methods.

ISSN: 2957- 7780

From the simulation, the PSO – ABC algorithm used for Optimum PMU Placement on IEEE – 14 bus, IEEE – 39 bus and the Kenya power Western region – 39 bus system and obtained results are presented in table 4. It is noticed that the algorithm offers several optimal solutions for various bus systems.

Table 1: PSO – ABC algorithm used for Optimum PMU Placement

Bus system	**Branches**	**Optimum PMU Placement location points**	**Number of PMUs**	**CPU run time**
IEEE-14 bus	16	1,4,6,8,14	6	0.11953s
IEEE-39 bus	46	2,4,6,8,13,16,18,20,23,26,32,33,35,37,38,39	16	0.41724s
Kenya Power Western region 39-bus	45	3,6,7,10,11,13,16,18,20,23,26,28,30,31,32,33,34,36	18	0.15046s

The result indicates that IEEE-14 bus system is completely observed by six PMUs using hybrid of PSO-ABC algorithm. PMUs are situated at buses; 1,4,6,8 and 14. IEEE – 39 bus system is completely observable by 16 PMUs that are located at buses; 2, 4, 6, 8, 13, 16, 18, 20, 23, 26, 32, 33, 35, 37, 38 and bus 39. The results for IEEE – 39 using PSO – ABC is validated with results with [16] and then applied to Kenya Power Western region 39 – bus system. The Kenya Power Western region 39 – bus system is fully observable with 18 PMUs located at 3, 6, 7, 10, 11, 13, 16, 18, 20, 23, 26, 28, 30, 31, 32, 33, 34, 34 and 36.

6. Conclusion

This paper proposes an optimum PMU placement (OPP) method which involves hybrid algorithm of particle swarm optimization and artificial bee colony. The combination of the two algorithms offers better exploration and exploitation capabilities in searching optimum by the ABC and the strong ability in global search by PSO. This has greatly helped in getting rid of weaknesses in the traditional algorithms by reducing the computational complexity and the problem of converging in the local minima. It will also reduce the converging rate. It is of great importance to note that simulation results of the Kenya Power Western – 39 bus system and IEEE – 39 bus system differs slightly despite having similar number of buses. The Kenya Power Western region bus system utilizes higher number of PMUs at 18 PMUs whereas IEEE – 39 bus system utilizes 16 PMUs for maximum observability.

 ISSN: 2957- 7780

References

[1] J. Chen, "Power System State Estimation Using Phasor Measurement Units," *Theses Diss. Comput. Eng.*, 2013, [Online]. Available: http://uknowledge.uky.edu/ece_etds/35.

[2] H. Drive and R. Gardens, "CONSULTANCY SERVICES FOR THE STUDY OF (SYSTEM OPERATIONS) REGULATIONS - 2023," no. August, 2023.

[3] S. Energy, S. Universit, P. Sud, and J. Warichet, "Power System Wide Area Measurement , Protection & Control Western America disturbance August 10 , 1996," 2013.

[4] N. M. Manousakis, G. N. Korres, S. Member, P. S. Georgilakis, and S. Member, "Optimal Placement of Phasor Measurement Units : A Literature Review," *2011 16th Int. Conf. Intell. Syst. Appl. to Power Syst.*, pp. 1–6, doi: 10.1109/ISAP.2011.6082183.

[5] Y. Bj, T. Marsland, and C. Tg, "Selective Depth-First Search Methods Selective Depth-First Search Methods," no. January, 2015.

[6] K. K. More and H. T. Jadhav, "A literature review on optimal placement of phasor measurement units," *Proc. 2013 Int. Conf. Power, Energy Control. ICPEC 2013*, pp. 220–224, 2013, doi: 10.1109/ICPEC.2013.6527654.

[7] P. Ayegba, J. Ayoola, E. Asani, and A. Okeyinka, *A Comparative Study of Minimal Spanning Tree Algorithms*, no. March. 2020.

[8] C. Cerrone, R. Cerulli, and B. Golden, "Carousel greedy: A generalized greedy algorithm with applications in optimization," *Comput. Oper. Res.*, vol. 85, no. May 2018, pp. 97–112, 2017, doi: 10.1016/j.cor.2017.03.016.

[9] A. Abdulkareem, D. Ogbe, T. Somefun, and F. Agbetuyi, "Optimal PMU placement using genetic algorithm for 330kV 52-Bus Nigerian network," *Adv. Sci. Technol. Eng. Syst.*, vol. 6, no. 1, pp. 597–604, 2021, doi: 10.25046/aj060164.

[10] E. O. Okendo, C. W. Wekesa, and M. J. Saulo, "Optimal placement of Phasor Measurement Unit considering System Observability Redundancy Index: case study of the Kenya power transmission network," *Heliyon*, vol. 7, no. 7, p. e07670, 2021, doi: 10.1016/j.heliyon.2021.e07670.

[11] A. Kumar, D. Kumar, and S. K. Jarial, "A review on artificial bee colony algorithms and their applications to data clustering," *Cybern. Inf. Technol.*, vol. 17, no. 3, pp. 3–28, 2017, doi: 10.1515/cait-2017-0027.

[12] B. Oduntan, F. Ariyo, and S. Akintade, "Optimal Placement of Phasor Measurement Unit on Electrical Grid Using a Hybrid Technique," *American Scientific Research Journal for Engineering*. [Online]. Available: http://asrjetsjournal.org/.

[13] X. Chen *et al.*, "Full coverage of optimal phasor measurement unit placement solutions in distribution systems using integer linear programming," *Energies*, vol. 12, no. 8, pp. 1–19, 2019, doi: 10.3390/en12081552.

[14] S. D. Immanuel and U. K. Chakraborty, “Genetic Algorithm: An Approach on Optimization,” *Proc. 4th Int. Conf. Commun. Electron. Syst. ICCES 2019*, no. July 2021, pp. 701–708, 2019, doi: 10.1109/ICCES45898.2019.9002372.

[15] C. Schwindt and J. Zimmermann, “Handbook on project management and scheduling vol. 1,” *Handb. Proj. Manag. Sched. Vol. 1*, vol. 1, pp. 1–663, 2015, doi: 10.1007/978-3-319-05443-8.

[16] S. Chakrabarti and E. Kyriakides, “Optimal placement of phasor measurement units for power system observability,” *IEEE Trans. Power Syst.*, vol. 23, no. 3, pp. 1433–1440, 2008, doi: 10.1109/TPWRS.2008.922621.

[17] R. Eberhart and J. Kennedy, “A New Optimizer Using Particle Swarm Theory,” pp. 39–43.

[18] G. Pereira, “Particle Swarm Optimization,” 2014. [Online]. Available: https://www.researchgate.net/publication/228518470.

[19] Y. Xu, P. Fan, and L. Yuan, “A simple and efficient artificial bee colony algorithm,” *Math. Probl. Eng.*, vol. 2013, 2013, doi: 10.1155/2013/526315.

[20] S. M. Kiseng, C. M. Muriithi, and G. N. Nyakoe, “Under voltage load shedding using hybrid ABC-PSO algorithm for voltage stability enhancement,” *Heliyon*, vol. 7, no. 10, p. e08138, 2021, doi: 10.1016/j.heliyon.2021.e08138.

[21] J. Zhong, “Phasor Measurement Unit (PMU) Placement Optimisation in Power Transmission Network based on Hybrid Approach,” 2012.

Impacts of Solar Cell Temperature for Power Generation in the Coastal Region of Kenya

J. Opole [1, *], G. Kidegho[1], J. Muga[1]

[1]Department of Electrical and Electronic Engineering, School of Engineering and Technology, Technical University of Mombasa, P.O. Box 90420-80100 Mombasa, Kenya.

Article History
Submission Date: 12th April 2024
Acceptance Date: 26th May 2024
Publication Date: 30th June 2024

Abstract

Solar cells convert radiant energy to electrical energy, however, as the solar cell temperature rises, the band gap narrows thus affecting cell characteristics like open circuit voltage, short circuit current, fill factor, and efficiency. This research project aimed to study solar cell temperature's impacts on the power generation of monocrystalline and polycrystalline solar cells in the coastal region of Kenya, particularly Mombasa, Kilifi, and Kwale Counties. The data on irradiance, ambient temperatures, solar cell temperatures, and wind speeds were collected and analyzed for PV module output characteristics. The findings revealed that the cell temperature rise ranged from 2.5 ℃ to 4.8 ℃ per unit rise in ambient temperature, the variation is governed by the local wind speeds. Cell temperature rise causes open circuit, short circuit current and fill factor to change by −0.023 V/°C to −0.056 V/°C, 0.0018 A/°C to 0.0025 A/°C, −0.0024 /°C to-0.0045 /°C for monocrystalline cells and −0.026 V/°C to −0.061 V/°C, 0.0017 A/°C to 0.0023 A/°C, -0.0025 /°C to -0.0047 /°C for polycrystalline cells. Moreover, the efficiency was noted to drop with the rise in cell temperatures. It has also been observed that for monocrystalline and polycrystalline cells of the same ratings when exposed to the same outdoor conditions, monocrystalline shows better performance in the coastal region of Kenya.

Keywords: Coastal region of Kenya, Solar PV module, High ambient temperatures, Cell temperature, Performance parameters

1) Introduction

Climate change has become a worldwide concern raising the global call to minimize the emission of greenhouse gases (Dwivedi et al., 2022). In the energy sector, a shift to renewable energy is a major step in the solution of this problem (Fankhauser, 2013)(Sinsel et al., 2020). Kenya is not left behind in championing this change at present and in the future by embracing

the use of renewable energy(Kiprop et al., 2019). Currently, renewable energy sources generate the bulk of Kenya's electricity at an installed capacity of 92% with the energy mix mainly being geothermal 828.04 MW, hydro 826.23 MW, wind 336.05 MW, solar 52.0 MW and bioenergy 2.00 MW (Kenyan energy report 2021). The Kenyan government has put in place strategies and policies to transcend to 100% renewable energy by 2030 (Kiprop et al., 2019), on full implementation of this plan, the country will experience a cost saving of up to 26.1 billion US dollars (Wambui et al., 2022). For a 100% transition, several untapped renewable energy potentials must be exploited to bring additional power to the grid. Research shows that solar PV and wind are the most promising technologies in Kenya (Manirambona et al., 2022). Kenya is endowed with very high solar potential with average annual Global Horizontal Irradiation (GHI) ranging from 5-7 kWh/m2/day (Kariuki and Sato, 2018). Solar PV technology is best suited for use since it is readily available, highly reliable, and provides a long life with low operational and maintenance cost (Pujan Jaiswal et al., 2021). Therefore, due to such advantages, solar PV tech-nology is acknowledged as a solution to energy problems in Africa (Quansah and Adaramola, 2018). Currently, the main utility, Kenya Power & Lighting Company serves approximately 8.6 million customers (KPLC report 2022), this leaves the rest of the population to look for alternative sources of energy independently. Thus energy technologies such as solar which is available everywhere in the country, is replenishable and can be easily tapped for use by PV module, and is suitable for use in rural areas that are not connected to the national grid. The coastal region of Kenya whose area is approximate-ly 67,500 square kilometers with a 600 km long coastline, experiences high ambient temperatures in most times of the year. This temperature has ad-verse effects on the performance of the solar cells since the efficiency of the crystalline solar cell de-pends on the amount of irradiance falling on the surface of the solar cell (Al-Naser et al., 2012). The most important cell parameters like open circuit voltage, short circuit current, fill factor, and efficiency of the solar cell are reported to change with temperature (Chander et al., 2015a; Genc, 2022), which can be remedied by employing various cooling methods to bring the temperature of the PV cells down for better power production (Abu-Rahmeh, 2017; Hudișteanu et al., 2021). This relationship provokes the study of the effects of temperature on the solar cell output parameters and how various cell technologies perform outdoors under the same temperature conditions in the coastal region of Kenya.

2) Theoretical basis and Mathematical modeling

 ISSN: 2957- 7780

2.1 Solar cell circuit diagram

The solar cell circuit diagram can be represented as shown in the Figure

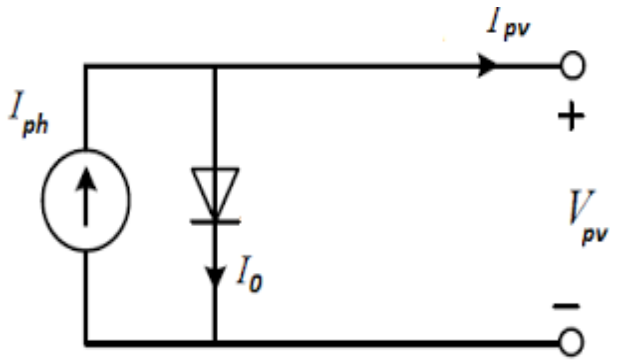

Figure 1: Schematic of ideal solar cell

A solar cell converts radiant energy from the electromagnetic spectrum waves to electrical energy. The electromagnetic spectrum that delivers energy to the solar cell consists of various wavelengths such as ultraviolet, visible light, and infrared wavelengths. Ultraviolet occupies 3% at 100 nm–400 nm, visible light 44% at 400 nm–700 nm, and infrared 53% at above 700 nm of the radiant energy spectrum(Sargunanathan et al., 2016). Solar cells mainly convert visible wavelengths of the electromagnetic spectrum to electrical energy (Kidegho et al., 2021). When the solar cell is illuminated with light energy, only the wavelengths whose energy is above the band gap energy will create electron-hole pairs in the solar cell. The wavelength cut-off frequency model (Dubey et al., 2013a; Singh and Ravindra, 2012) is described as;

$$\lambda_g = \frac{1240}{E_g(eV)}(nm) \qquad (1)$$

Where λ_g is the cut-off wavelength, E_g is the band gap energy and eV is energy in electron-volts. The charged electron-hole pairs generated by the radiant energy in the band gap cause current density (Khatibi et al., 2019; Shockley and Queisser, 1961) modeled by;

$$J = -J_{ph} + J_O\,(e^{\frac{qV}{nKT}} - 1) \qquad (2)$$

J is the current density, J_ph is the photo-generated current density, Jo is the diode reverse saturation current density, n is the diode ideality factor, q is the charge and V is the voltage across the cell terminals, K is the Boltzmann constant and T is the temperature. The radiant energy whose wavelength is above the cut-off frequency causes heating in solar cells (Kidegho et al., 2021). The semiconductor band gap dependence on temperature (Singh and Ravindra, 2012) is given by;

ISSN: 2957- 7780

$$E_g(T) = E_g(o) - \frac{\alpha T^2}{(T+\beta)} \quad (3)$$

Where E_g (T) refers to the band gap of the semiconductor at some temperature T, which may be direct or indirect,E_g (o) is the band gap value at T= 0 K, α and β are constants. Band gap decreases with temperature, reduction in the band gap results in increased current as more photons can excite electrons in the valence band of the semiconductor. On the other hand, an increase in temperature leads to an increase in the internal energies of the silicon particles, which leads to increased collisions hence increased resistance leading to a reduced charge recombination process hence a decrease in VOC (Ndeto et al., 2022). Fill factor and efficiency are functions of both current and voltage and since voltage is affected more, the two also reduce.

2.2 Main Solar Cell Output Parameters

2.2.1Open circuit voltage

When the solar cell is not connected to the load, no current flows through the terminals, the voltage measured across the cell terminals, in this case, is maximum, referred to as open circuit voltage (Singh and Ravindra, 2012) modeled as;

$$V_{oc} = \frac{kT}{q} in(\frac{Isc}{Io} + 1) \quad (4)$$

Where V_{oc} is the cell open circuit voltage, Isc is the short circuit current. The temperature dependence of V_{oc} can be derived (Chander et al., 2015a; Green et al., 2011) by;

$$\frac{dV_{oc}}{dT} = \left(\frac{V_{oc}}{T}\right) + V_{th}(\frac{1}{I_{sc}}\frac{dI_{sc}}{dT} - \frac{1}{I_o}\frac{dI_o}{dT}) \quad (5)$$

Where dV_{oc} is the change in open circuit voltage, dI_{sc} is the change in short circuit current,$V_{th} = KT/q$, dI_o is the change in reverse saturation current and dT is the temperature change.

2.2.2 Short circuit current

When no load is connected to the solar cell and the terminal is shorted, the current flowing in this case is referred to as short circuit current abbreviated as Isc. It is directly proportional to the photocurrent from the incident solar energy. The density of the electron-hole pairs generated in the solar cell band gap is proportional to the incoming radiant energy. Thus, the model relating current to the spectral irradiance (Chander et al., 2015a; Singh and Ravindra, 2012) is given by;

 ISSN: 2957- 7780

$$I_{sc} = q \int_{hv=E_g}^{\infty} \frac{dN_{ph}}{dhv} d(hv) \qquad (6)$$

Where N_{ph} is the initial photon flux.

2.2.3 Fill factor

This is the ratio of the maximum power generated by the solar cell to the product of open circuit voltage and the short circuit current (Khatibi et al., 2019) modeled by;

$$FF = \frac{P_{max}}{V_{oc}\, I_{sc}} \; or \; \frac{V_{max}\, I_{max}}{V_{oc}\, I_{sc}} \qquad (8)$$

$$FF = \frac{V_{oc} - In(V_{oc} + 0.72)}{V_{oc} + 1} \qquad (9)$$

Where V_{oc} = (v_{oc}/V_{th}) is defined as normalized Voc. Temperature dependence of the fill factor can be obtained by (Khatibi et al., 2019)

$$\frac{dFF}{dT} = \frac{(\frac{dV_{oc}}{dT} - V_{oc/T})}{(V_{oc} + V_{th})} \left\{ \frac{(V_{oc}/V_{th} + 0.28)}{(V_{oc}/V_{th} + 0.72)} - FF \right\} \qquad (10)$$

$$\frac{1}{FF} \frac{d(FF)}{dT} \approx -0.0013 \; per \; ℃ \qquad (11)$$

The change of fill factor with the temperature is given by $\frac{dFF}{dT}$ and $\frac{dV_{oc}}{dT}$ is the change of open circuit voltage with temperature.

2.2.4 Efficiency of the cell

A solar cell is an energy conversion device. Where energy conversion takes place, the ratio of energy conversion is a factor of consideration. For the solar cell, the efficiency is given by the ratio of output electrical energy from the solar cell to input radiant energy from the sun (Khatibi et al., 2019; Singh and Ravindra, 2012; Smestad et al., 2008);

$$\eta = \frac{P_{max}}{P_{in} Area} \text{ or } \eta = \frac{V_{oc}\, I_{sc}\, FF}{P_{in}} \qquad (12)$$

P_{max} is the maximum power obtained from the solar cell, P_{in} incoming irradiance in (W/m^2) and $Area$ is the area of the solar cell in square meters

2.2.5 The Duffie and Beckmann Model

Research has shown that solar cell temperature is influenced by the incident irradiance, temperature of the surroundings, and wind speeds (Chandra et al., 2018; Genc, 2022; Zhe et

 ISSN: 2957- 7780

al., 2019). Duffie and Beckmann modeled the correlation between these factors using the model in Equation 13;

$$T_c = T_a + \left[\left(\frac{G}{G_{NOCT}}\right)\frac{9.5}{5.7 + 3.8V_w}(T_{cNOCT} + T_{aNOCT})\right] \quad (13)$$

Where T_c is the cell temperature, T_a is the ambient temperature, G is the irradiance, G_{NOCT} is the irradiance at normal cell operating temperature, V_w is wind speed taken for values less than one, T_{cNOCT} is the normal operating cell temperature and T_{aNOCT} is the normal operating ambient temperature.

3) Materials and Methods

Before data collection commenced, modeling and simulation were carried out for the various solar PV module parameters, this is important for a quick scan of what to expect under field conditions.

3.1 Setup for Temperature Effects Simulation in PVsyst software.

According to weather data, the ambient temperature for the coastal region of Kenya ranges from 22 ℃ to 32 ℃. Based on this data ambient temperature ranging from 20 ℃ to 33 ℃ was modeled using Duffie and Beckmann model (Equation-13) to obtain the expected corresponding cell temperature and the result obtained. Moreover, solar PV output parameters were simulated in PVsyst software at standard test conditions for various cell temperatures ranging from 25 ℃ to 65 ℃. The setting for the simulation in the PVsyst window is shown in Figure 2. The key control parameters were maximum irradiance value, short circuit current, open circuit voltage, efficiency, and cell temperature.

ISSN: 2957- 7780

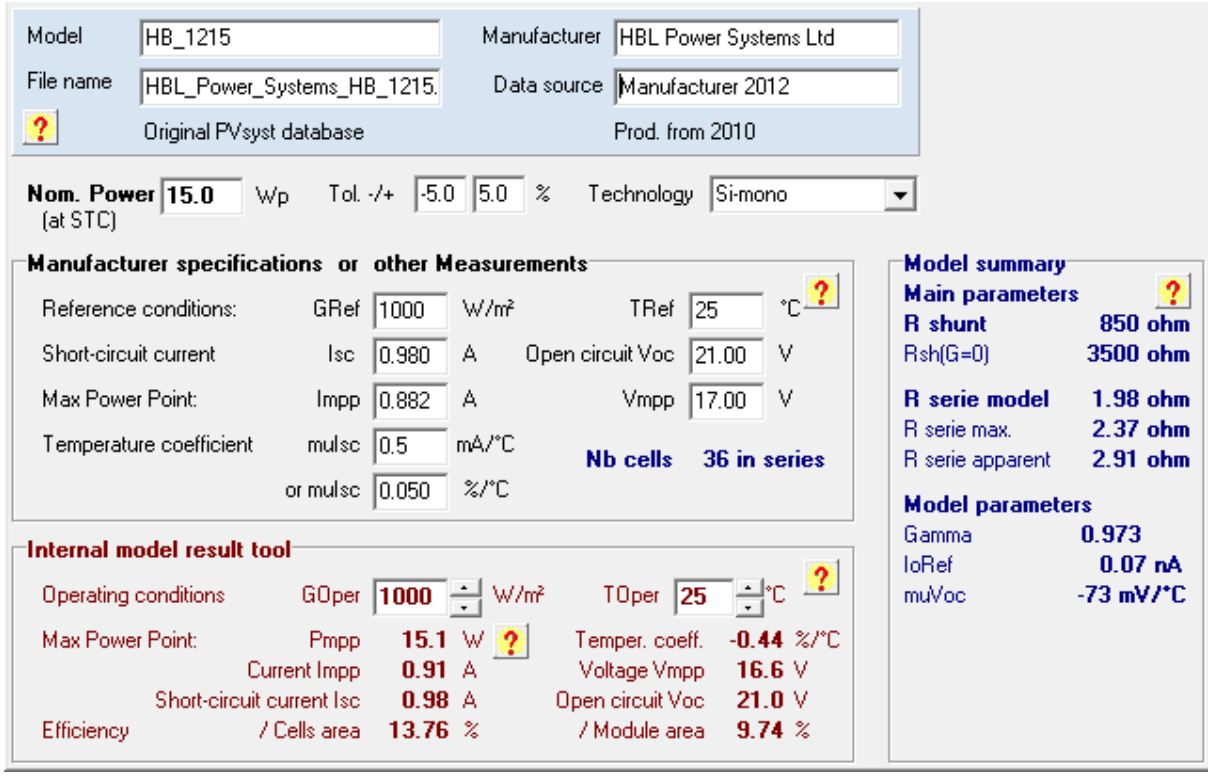

Figure 2: PV parameters setting on PVsyst window

3.2 Setup for measurement of Voc, Isc Temperature and Power

In this setup, the performance of solar PV modules was then investigated under outdoor conditions. The studies were based on three Counties of the coastal region of Kenya (Mombasa, Kilifi, and Kwale). The specific selected sites for the study were Technical University of Mombasa (4°02'18.4"S 39°40'10.9" E) in Mombasa County, Mtwapa Primary school (3°56'33.6"S 39°45'46.8"E) in Kilifi County and Mwakigwena Primary school (4°16'48.4"S 39°33'36.2"E) in Kwale County. Several measurements were carried out for each site on separate days since the setup could not be mounted simultaneously on all sites. Monocrystalline and polycrystalline solar PV modules were chosen for the study since they are the most commonly used solar PV technologies in the coastal region of Kenya for power generation from the survey conducted earlier. Four panels were used, two for monocrystalline type and the other two for polycrystalline type. Thermocouples type K were used for temperature measurements. Each solar panel had a thermocouple mounted at the back side where it sensed the panel temperature and sent the equivalent signal to the data logger through a channel configured for temperature measurements. One solar PV module from each type was used to measure open circuit voltage, and the terminals of solar PV were connected to the data logger through a channel configured for measurements of voltage. Similarly, one solar PV module of

ISSN: 2957- 7780

each type was used for short-circuit current measurements. The terminals of each solar PV module were connected to the data logger through a channel configured for current measurements. All these solar PV module parameters like panel temperatures, currents, and voltages were logged using the KEYENCE NR-500 data logger [Figure 3 (g)], at a rate of one second to note any slightest change in the parameters and for continuous readings. The solar irradiance (W/m2) was measured using a PCE-SPM1 solar irradiance meter [Figure 3 (d)] that was mounted together with PV modules. Wind speed and ambient temperature were measured using a digital anemometer fitted with a temperaturesensor [Figure 3 (f)]. The measurements from the data logger were monitored through the measurement window on the computer screen [Figure 3 (e)]. The measurement of power was performed for the two solar PV modules [Figure 3 (b)]. Rheostat (0-10 Ω, 2 A) was used as the variable load connected to the PV module circuit. Each solar PV module was connected to the separate rheostat with the same adjustment. One multimeter was connected in series to each solar PV module for current measurements and one voltmeter was connected across the variable resistor for volts drop measurements. The measurements from both meters were taken for each PV module when the values of resistances were 0 Ω. The resistances were increased gradually at intervals of 1 Ω and readings for currents and corresponding volts drop were taken from each meter for each solar PV module. The power was calculated by finding the product of currents and corresponding volts drop across the load. The maximum power points obtained from this calculation were used to compute fill factors and efficiencies using the model Equations 8 and 12 respectively.

 ISSN: 2957- 7780

Figure 3: Equipment used and set up for outdoor measurement; (a) Solar PV module preparations for measurements, (b) Power measurements (c) Solar PV arranged for Voc & Isc measurements, (d) Irradiance meter, (e) Reading on the computer screen, (f) Digital anemometer and (g) Data logger.

4) Results and Discussions

The results and discussion for this work are divided into two parts. Firstly, the results of output characteristics of solar PV modules from the model and simulation from PVsyst are analyzed and the findings are discussed. Secondly, the results from the outdoor measurements from the sites are analyzed and the findings are discussed.

4.1 Simulation results

4.1.1 Result from Duffie and Beckmann model

This model shows the relationship between the ambient temperature and the solar cell temperature. The Duffie and Beckmann model is shown in Equation 13. Various cell temperatures were modeled for different values of ambient temperature and the values are plotted to produce the graph in Figure 4.

ISSN: 2957- 7780

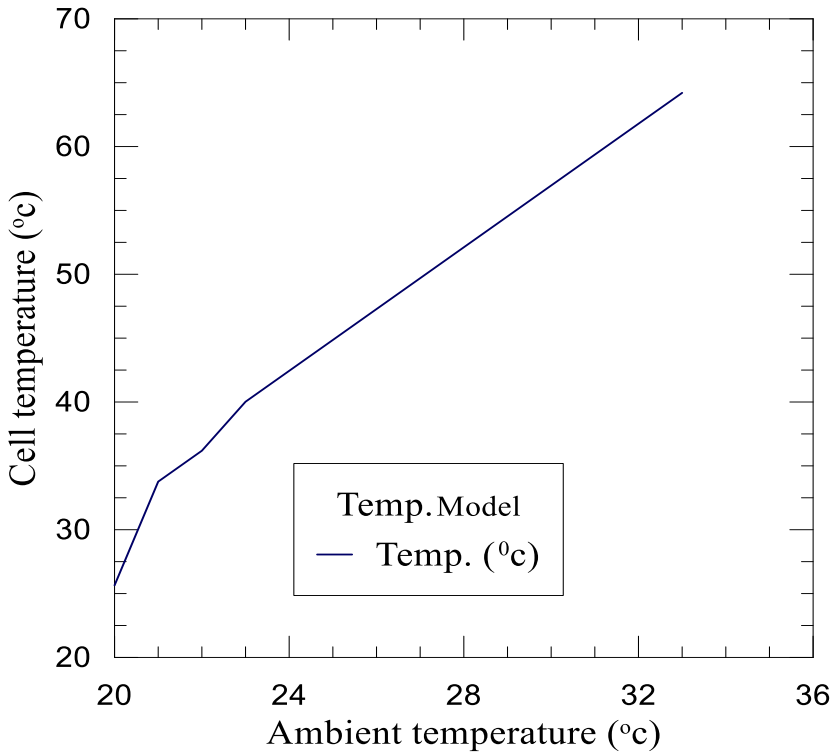

Figure 4: Simulation from Duffie and Beckmann model

From the relationship, it is observed that cell temperature relates to ambient temperature such that when the ambient temperature increases, there is a notable increase in cell temperature and when the ambient temperature is low, cell temperature is equally low. It can be observed from the relations that for every 1 ℃ rise in ambient temperature, the cell temperature rise ranged from 2.5 ℃ to 4.8 ℃. This value is not constant but subject to change depending on the local wind speeds.

4.1.2 PVsyst simulation results.

A 15 Wp, 21.6 Voc solar PV module with 36 series connected monocrystalline cells was chosen for the simulation. The solar characteristics were entered in the PVsyst window as shown in Figure 2. The simulations were run and results obtained as shown in Figure 5; current-voltage graph at various cell temperatures (i), power-voltage graph at various cell temperatures and constant irradiance (ii), power-voltage graphs at various cell temperatures and irradiance levels (iii) and module efficiency at various cell temperatures (iv). The current-voltage curve [Figure 5(i)], shows that an increase in cell temperature above 25 ℃ causes a notable decrease in solar cell open circuit voltage and a very small increase in short circuit current. The decrease in open circuit voltage is noted to be 0.073 V/℃ while the from 25 ℃ to 65 ℃, a drop in open circuit voltage is increase in short circuit current is noted to be 0.0005 A/℃. On the same note, as the cell temperature is increased observed from 21.6 V to 18 V. The effect of cell temperature is well seen in the power output shown in [Figure 6 (i) & (ii)] where the maximum power is obtained from the module when the temperature is at 25 ℃, a notable drop in power at the rate of 0.07 W /℃ is observed as the temperature rose above 25 ℃. The output power dropped up

ISSN: 2957- 7780

to 12.4 W when the cell temperature was 65 ℃. [Figure 6 (ii)] shows the behavior of the module efficiency with temperature, the drop in efficiency was recorded to be 0.44% /℃. The efficiency of the module is a factor of open circuit voltage and short circuit current since the temperature has a notable effect on the open circuit voltage, this is reflected in the output of the solar module while the current experiences a very small increase.

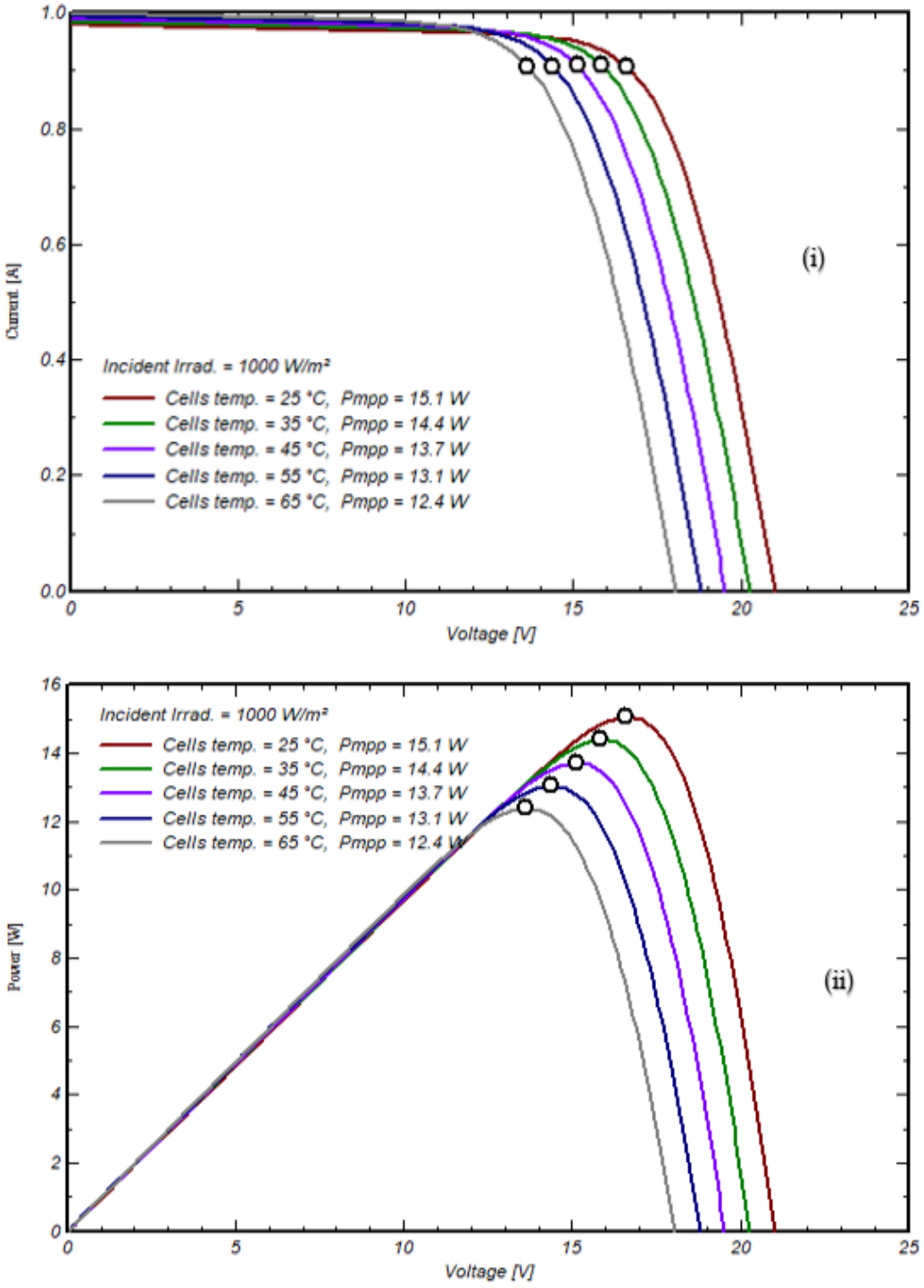

Figure 5: Simulated I-V and P-V curves from PVsyst at a constant irradiance; (a) Current-Voltage curve, (b) Power-Voltage curve.

ISSN: 2957- 7780

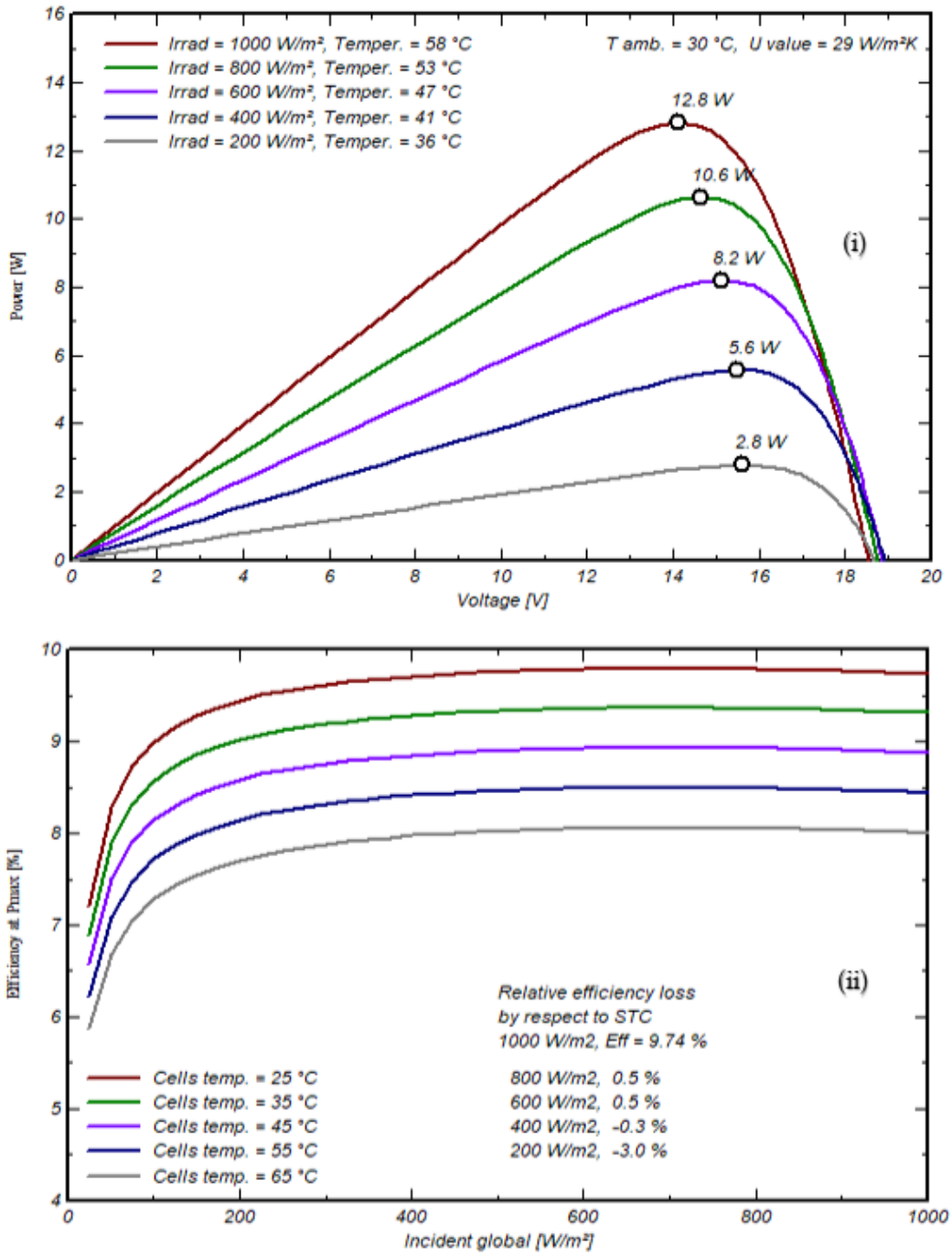

Figure 6: Effects of irradiance on P-V curve and the variance in Efficiency with temperature; (i) Power-Voltage curve at various irradiance values, (ii) Efficiency of the module at different cell temperatures

4.2 Result from Outdoor Measurement

4.2.1 Behavior of environmental parameters

The results of the measured environmental parameters such as irradiance, ambient temperature, and wind speeds are presented in this sub-section. Their relationship with cell temperature which is the key parameter of the study was analyzed and presented in Figure 7.

 ISSN: 2957- 7780

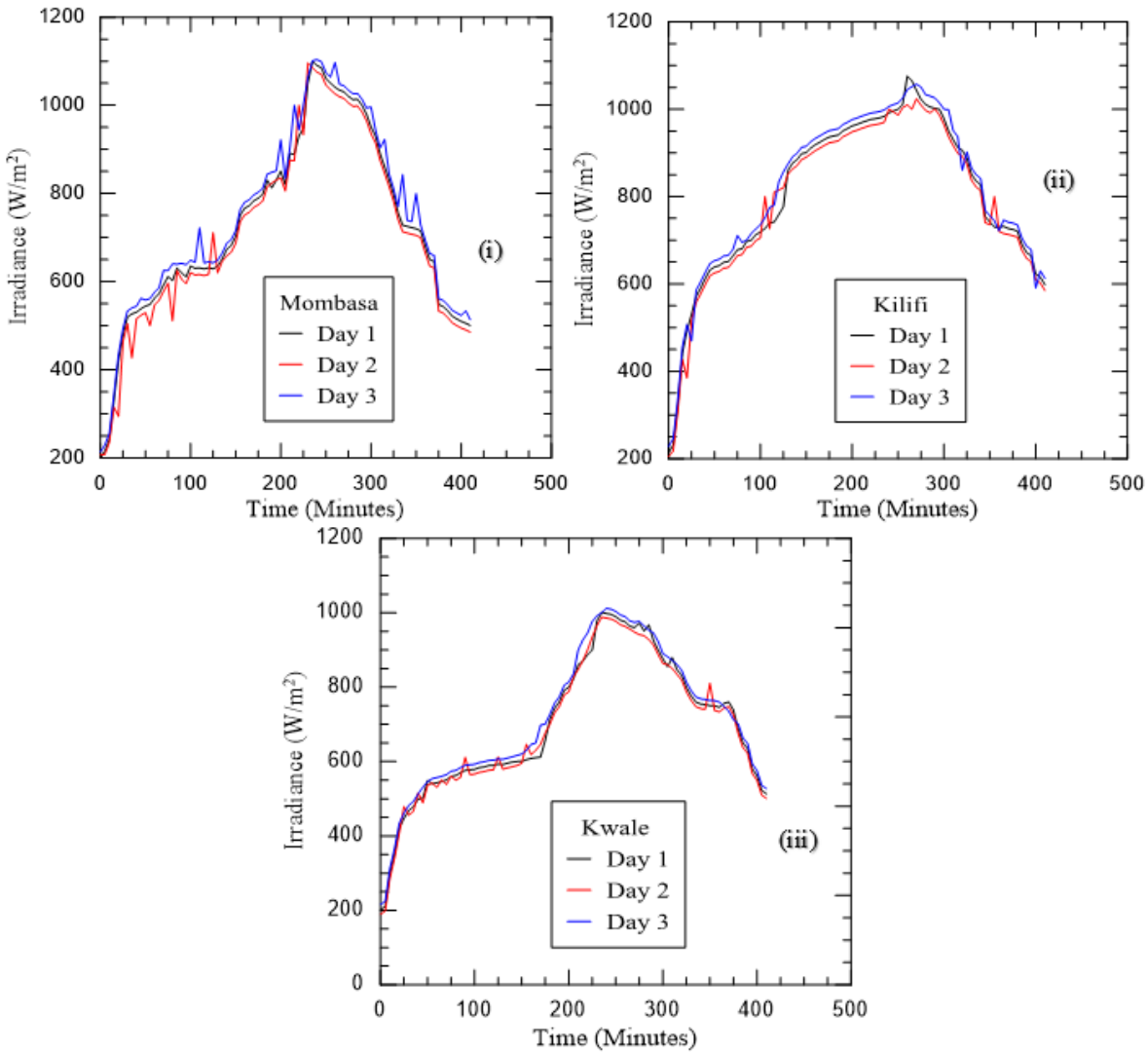

Figure 7: Irradiance Distribution (W/m2); (i) Mombasa site, (ii) Kilifi site and (iii) Kwale site

Data on irradiance were collected for three different days per site and the finding presented as shown in Figure 7, was to show the irradiance distribution pattern in each site. Irradiance ranging from 200 W/m2 to 1100 W/m2 was recorded in Mombasa [Figure 7 (i)], where the maximum irradiance was recorded at 1.00 pm. For Kilifi, the irradiance ranged from 213.73 W/m2 to 1076 W/m2 with maximum irradiance observed at 1.25 pm [Figure 7 (ii)]. Similarly, irradiance of 201.63 W/m2 to 1000.72 W/m2 was recorded in Kwale [Figure 7 (iii], where the maximum irradiance was noted at 12.55 pm. The irradiance is noted to increase from morning and reach a maximum at around 1:00 p.m. before it started decreasing. As irradiance increases, the ambient temperature was observed to increase resulting in to increase in solar PV module temperature. The effect of an increase in solar PV module temperature is seen in the output parameters represented in Figure 8.

ISSN: 2957- 7780

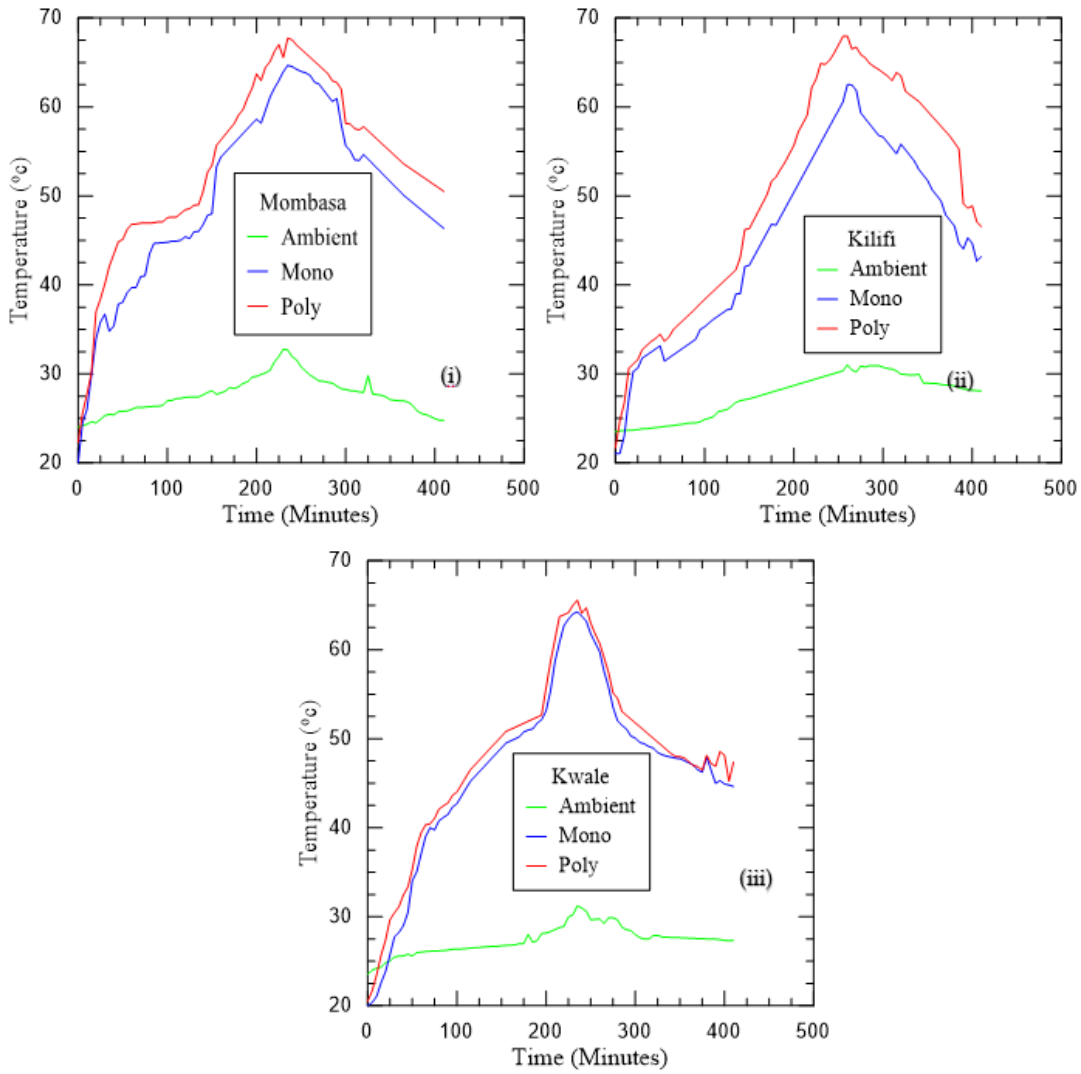

Figure 8: Ambient and Cell Temperature; (i) Mombasa site, Kilifi site (ii) and (iii) Kwale site

As irradiance increased, the ambient temperature increased, and likewise the cell temperature. This is observed in all three sites as shown in [Figure 8(i), (ii) and (iii)] which is in agreement with the literature (Chakiri and Lamchich, 2021; El Achouby et al., 2018; Fébba et al., 2018; Musanga et al., 2018). The maximum ambient temperature recorded in Mombasa was 32.69 ℃ [Figure 8 (i)], 31.03 ℃ in Kilifi [Figure 8 (ii)], and 31.22 ℃ in Kwale [Figure 8 (iii)]. The temperature for the monocrystalline solar module rose to a maximum of 64.68 ℃, 62.51 ℃, and 64.27 ℃ for the Mombasa, Kilifi, and Kwale sites respectively, while for the polycrystalline module, the rise was 67.72 ℃, 67.95 ℃, and 65.57 ℃ for the same sites, respectively. It is noted that the cell temperature rise varies from 2.0 ℃ to 4.5 ℃ per unit rise in ambient temperature. These findings agree with the results from Duffie and Beckmann's model presented in Figure 4. This variation is nonlinear due to the effect of wind speeds as further presented in Figure 9.

ISSN: 2957- 7780

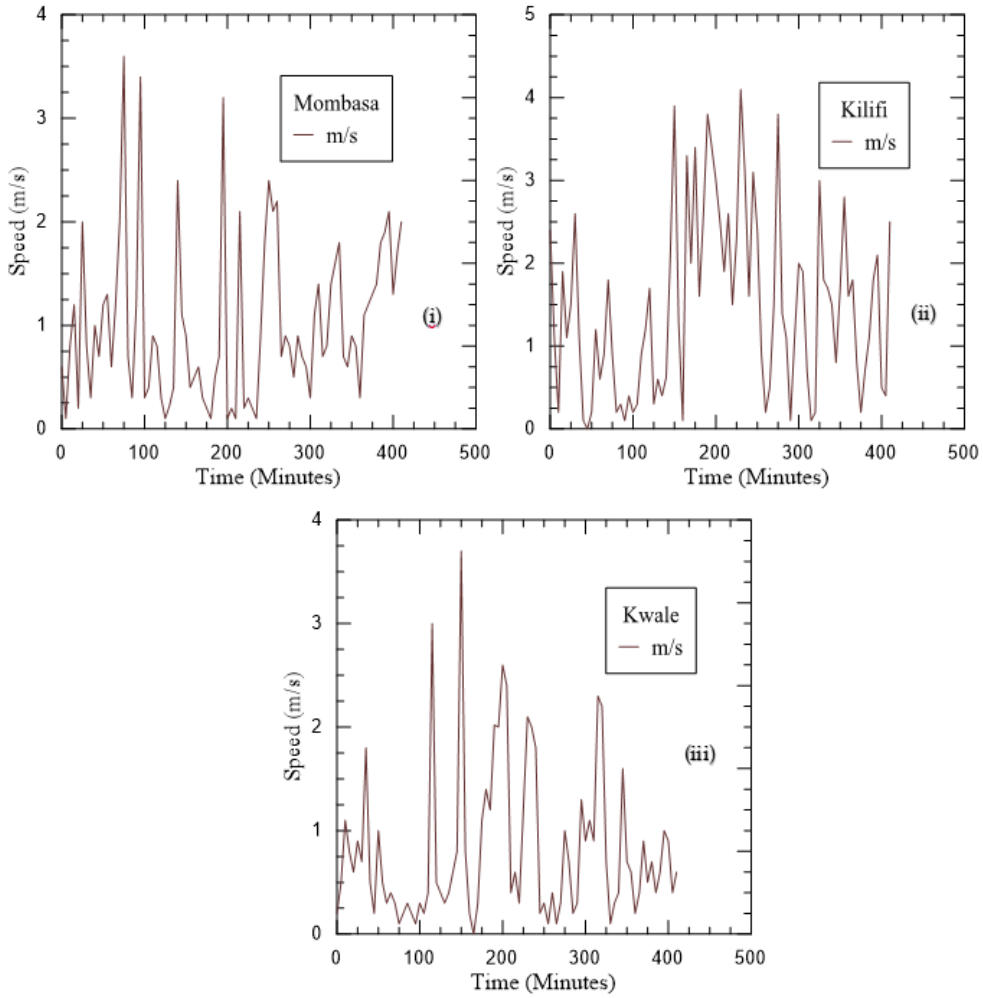

Figure 9: Wind speed Distribution; (i) Mombasa site, (ii) Kilifi site, and (iii) Kwale site.

Figure 9 shows wind speed measurement results. The necessity of this is that the movement of wind aids in cooling solar PV modules (Chandra et al., 2018; Zhe et al., 2019) by sweeping away the heat waves generated at the back of the panel, therefore, the stronger the wind speeds, the higher the cooling thus increased power production. For the Mombasa site wind speeds ranging from 0.1 m/s to 3.6 m/s were recorded [Figure 9 (i)], while for the Kilifi site, the wind speeds ranged from 0.1 m/s to 4.1 m/s [Figure 9 (ii)]. On the other hand, for the Kwale site, the wind speeds ranged from 0.1 m/s to 3.7 m/s [Figure 9 (iii)]. In all the sites, the wind speed was not constant but changed after short intervals of time producing spiked graphs shown in Figure. 9.

4.2.2 PV Performance Parameters

The results presented in the sub-section show how the solar PV module output characteristics varied when exposed to environmental conditions. The main characteristics presented here are; open circuit voltage, short circuit current, fill factor, and efficiency.

ISSN: 2957- 7780

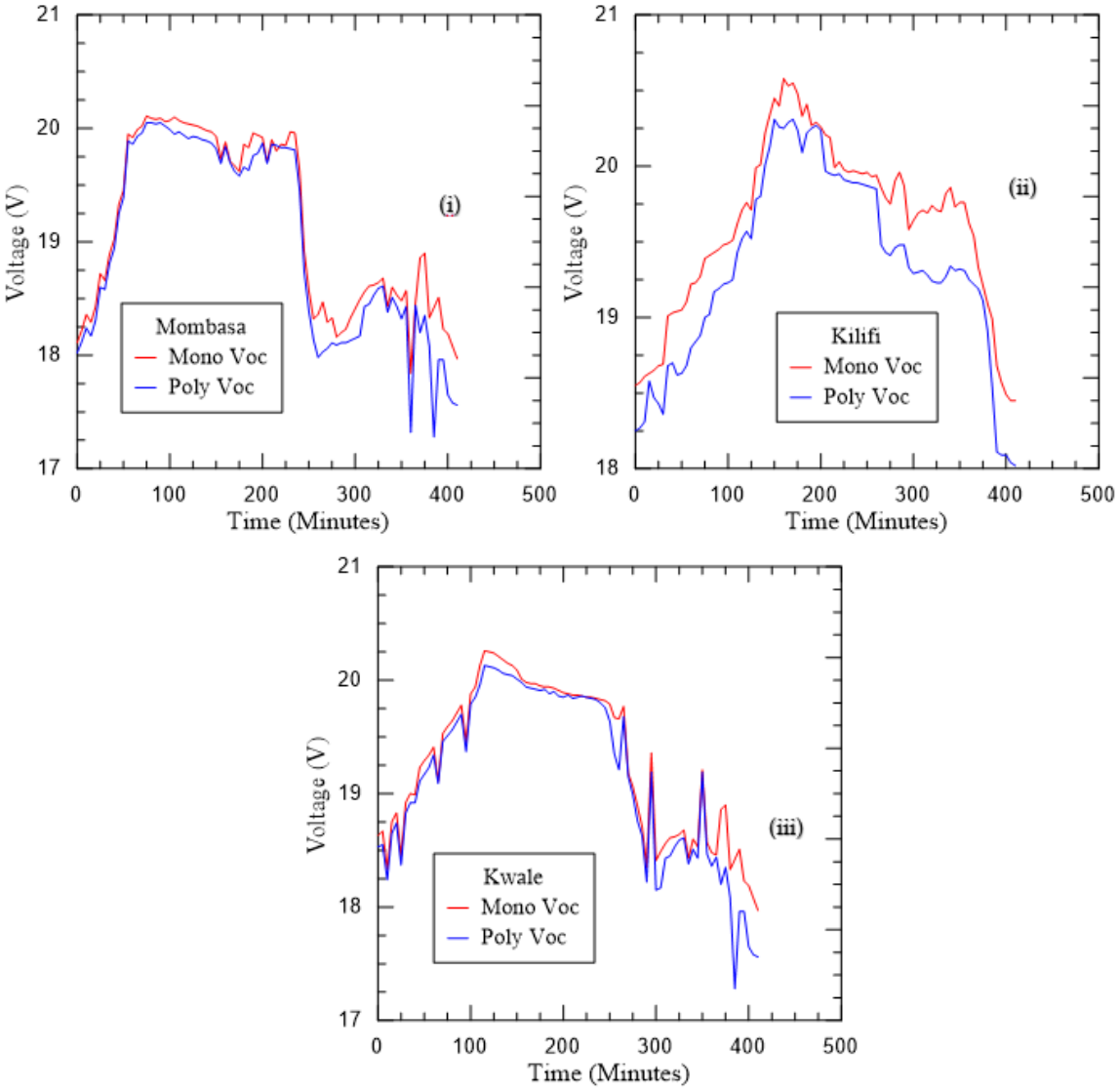

Figure 10: PV module Open Circuit Voltage; (i) Mombasa site, (ii) Kilifi site and Kwale site.

At the start of the data collection in the morning, the value of the solar irradiance was low, as the irradiance increased, open circuit voltage was seen to increase proportionately. At an irradiance of 611.36 W/m2 and cell temperature of 41.03 ℃ maximum open circuit voltage of 20.11 V was observed in the Mombasa site for monocrystalline [Figure 10 (i)], while at the same irradiance and cell temperature of 46.93 ℃ and open circuit voltage of 20.05 V was obtained in Mombasa site for polycrystalline [Figure 10 (i)]. For Kilifi the maximum open circuit voltages were obtained at irradiances of 850 W/m2, monocrystalline had an open circuit voltage of 20.45 V at a cell temperature of 42.21 ℃ while polycrystalline had an open circuit voltage of 20.31V at a cell temperature of 46.33 ℃ [Figure 10 (ii)]. [Figure 10 (iii)] shows the data for the Kwale site, at an irradiance of 600 W/m2 and cell temperature of 45.20 ℃, a maximum open circuit voltage of 20.26 V was obtained for monocrystalline while at 46.67 ℃

 ISSN: 2957- 7780

an open circuit voltage of 20.13 V for polycrystalline module was obtained. The drop in open circuit voltage as the cell temperature rose above the nominal cell operating temperature, was observed to range from 0.023 V/°C to 0.056 V/°C for monocrystalline and 0.026 V/°C to 0.061 V/°C polycrystalline. This finding is close to the simulation results which had a coefficient of 0.073 V/°C. The outdoor findings are noted to be slightly higher, this is attributed to higher ambient temperatures along the coastline region.

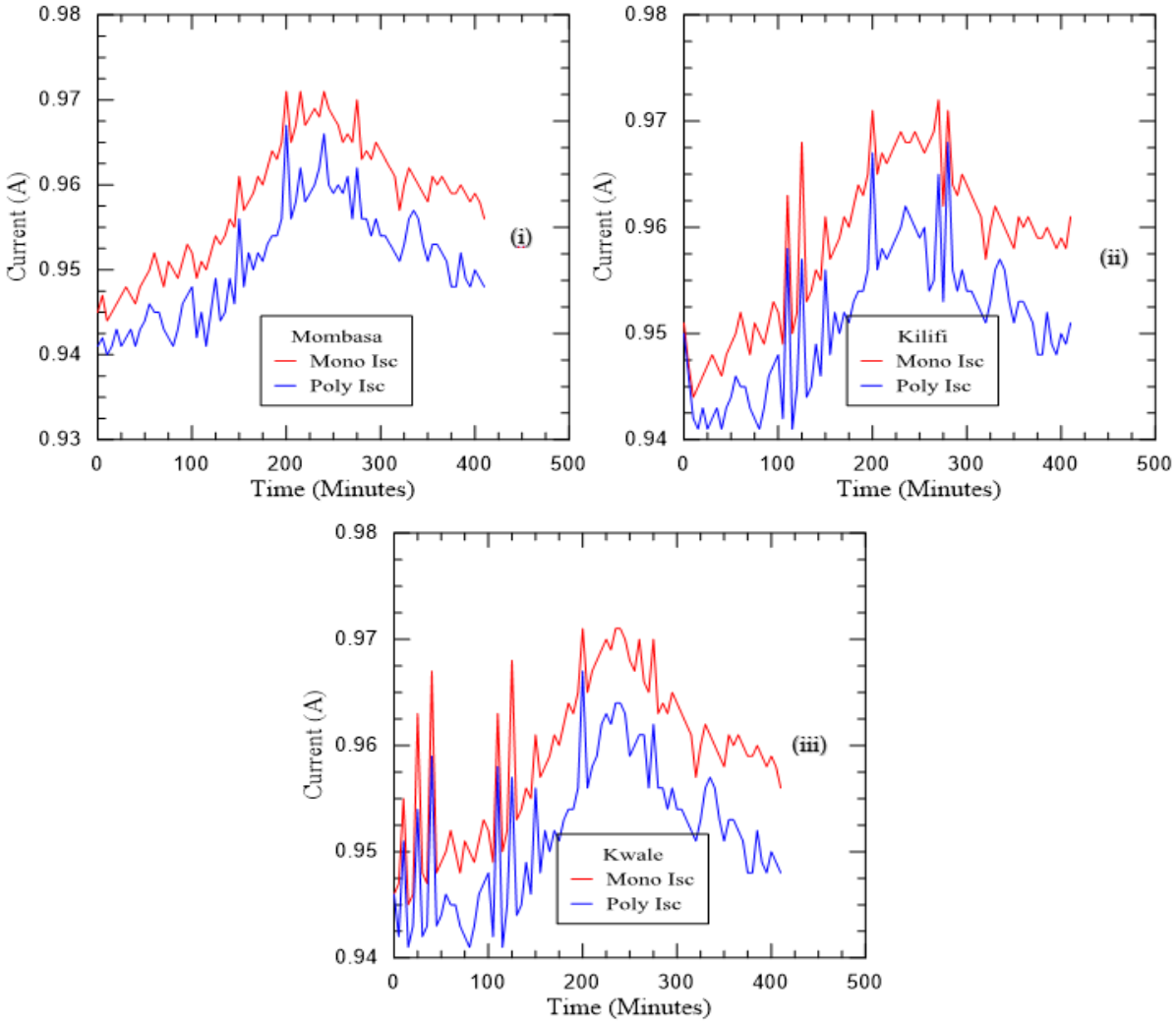

Figure 11: PV module Short Circuit Current; (i) Mombasa site, (ii) Kilifi site and (iii) Kwale site

The results for short circuit current site measurements at three sites are shown in Figure 11. As the cell temperature increases above the nominal cell operating temperature, a slight increase in short circuit current is observed in all three sites. Short circuit current increased from 0.945 A to 0.968 A for monocrystalline and from 0.941 A to 0.962 A for polycrystalline PV module as depicted from Mombasa site measurements [Figure 11 (i)]. The measurements for Kilifi are shown in [Figure 11 (ii)] where the current slightly increased from 0.951 A to 0.961 A for

ISSN: 2957- 7780

monocrystalline solar PV module and from 0.95 A to 0.956 A for polycrystalline PV module. For the Kwale site [Figure 11 (iii)], similar slight changes were noted from 0.946 A to 0.971 A for monocrystalline and 0.946 A to 0.964 A for polycrystalline solar PV modules. The increase rate is observed to range between 0.0018 A/°C to 0.0025 A/°C for monocrystalline and 0.0017 A/°C to 0.0023 A/°C for polycrystalline module. This finding is close to the simulation findings of 0.0025 A/°C and agrees with the findings by (Chander et al., 2015b) of 0.002 A/°C.

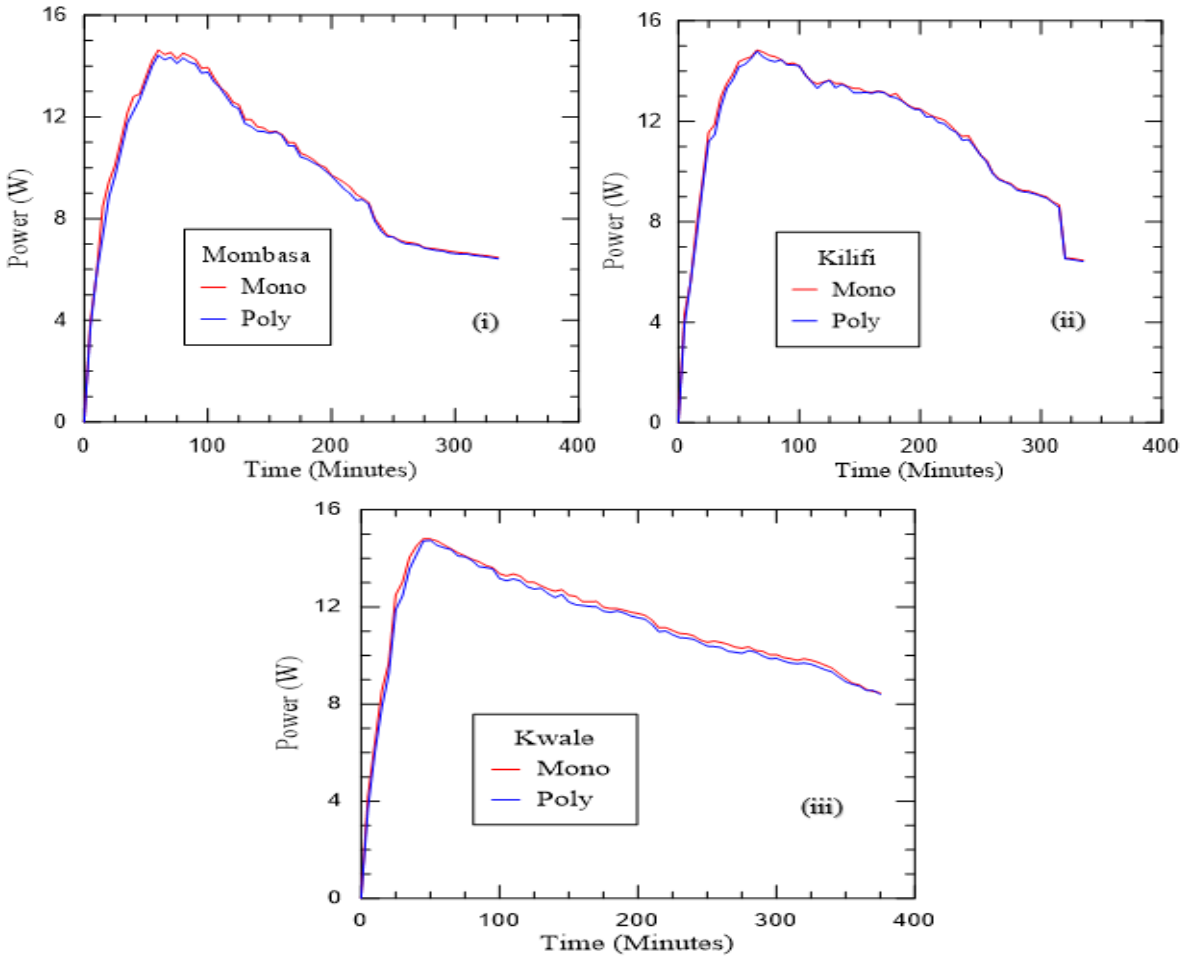

Figure 12: PV module Power; (i) Mombasa site, (ii) Kilifi site (iii) Kwale site

Figure 12 shows the output power generated by the PV modules in the areas of each site, The power generated was noted to rise with the increase in irradiance up to maximum points at nominal cell operating temperature, beyond which the power generated from the modules started to drop as cell temperature increased further. The maximum power obtained. Maximum power of 14.68 W and 14.47 W were recorded in the Mombasa site [Figure 12 (i)], while

ISSN: 2957- 7780

14.83 W and 14.79 W were obtained for the Kilifi site [Figure 12 (ii)]. For the Kwale site maximum power of 14.81 W and 14.71 W were recorded [Figure 12 (iii)].

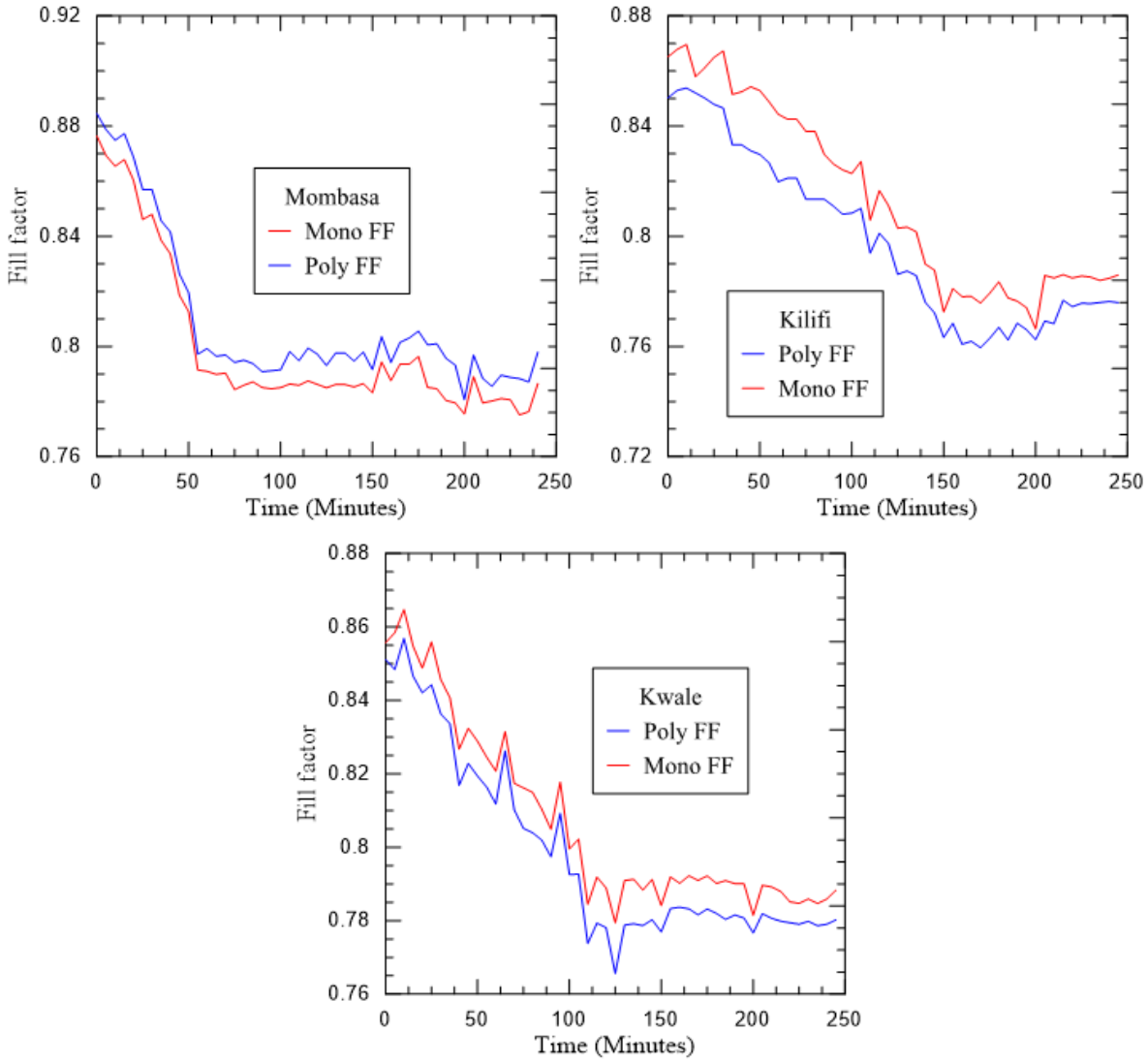

Figure 13: PV module Fill Factor; (i) Mombasa site, (ii) Kilifi site and (iii) Kwale site.

The fill factor for the solar panels is shown in the graphs in Figure 12. At cell temperature above the nominal cell operating temperature fill factor is seen to decrease with an increase in cell temperature. For the monocrystalline PV module, the decrease is from 0.88 to 0.79 and 0.87 to 0.78 for polycrystalline panels for the Mombasa site shown in [Figure 12 (i)]. The decrease is noted to be 0.87 and 0.77 for monocrystalline and 0.85 to 0.76 for polycrystalline in the Kilifi site [Figure 12 (ii)]. The measurement result from the Kwale site is from 0.85 to 0.78 for Monocrystalline and 0.85 to 0.75 for polycrystalline solar PV modules. From the findings, the fill factor appears to drop in the range of 0.0024 /°C to 0.0045 /°C for

ISSN: 2957- 7780

monocrystalline and 0.0025 /℃ to 0.0047 /℃ for polycrystalline solar PV modules. These results are close to other previous findings (Chander et al., 2015a; Pradhan and Panda, 2017) which is - 0.002 /℃

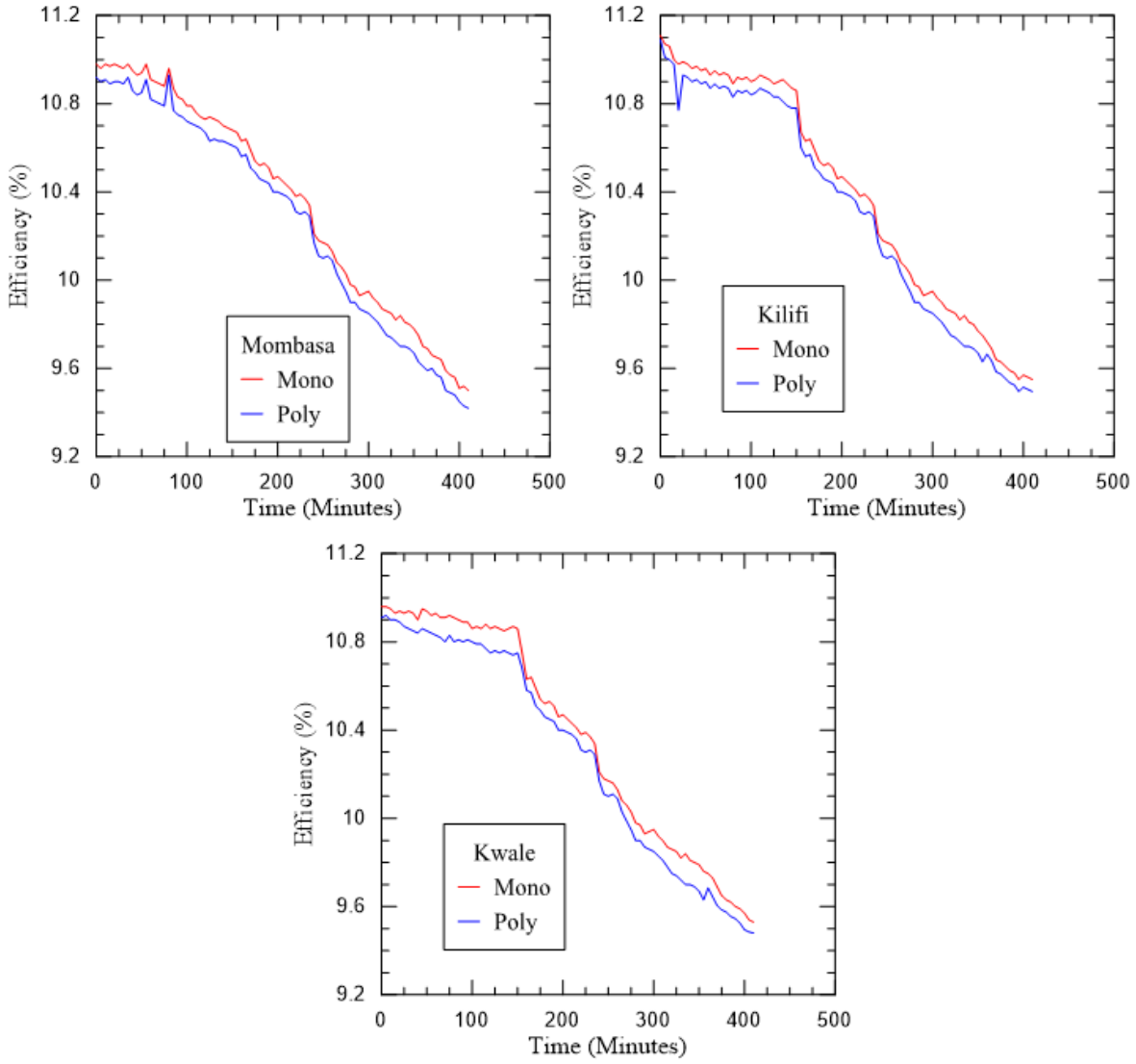

Figure 14: PV module Efficiency; (i) Mombasa site, (ii) Kilifi site and (iii) Kwale site.

The behavior of solar PV efficiency is observed in Figure 13. It can be seen that the maximum efficiency for the monocrystalline PV is 11.1 % and 11 % for the polycrystalline PV module for the Mombasa site as shown in [Figure 13 (i)] while for the Kilifi, site the maximum efficiencies for the panels are 11 % and 10.9 % for monocrystalline and polycrystalline solar panels respectively as shown in [Figure 13 (ii)]. The findings in the Kwale site are as shown in [Figure 13 (iii)], monocrystalline had a maximum efficiency of 11 % while that of polycrystalline was 10.9 %. The efficiencies for both monocrystalline and polycrystalline solar

ISSN: 2957- 7780

panels decrease as the cell temperature rises above the nominal cell operating temperature. The rate of drop rate ranged from 0.46 % to 0.51 %/℃ for monocrystalline while that for polycrystalline is 0.47 %/℃ to 0.53 %/℃, which strongly agrees with (Dubey et al., 2013a, 2013b; Rahman et al., 2015) as well as the simulation results.

5) Conclusion

From the analysis, it is observed that an increase in irradiance causes an increase in cell temperature and ambient temperature. The rise in cell temperature ranged from 2.5 ℃ to 4.8 ℃ per unit rise in ambient temperature, the variation depends on the local wind speeds. When exposed to the same outdoor conditions, the polycrystalline cell is noted to be 4 ℃ to 5 ℃ hotter than monocrystalline. The main solar output parameters such as open circuit voltage, short circuit current, fill factor, and efficiency are affected by cell temperatures. This is revealed in all the sites along the coastal region for both monocrystalline and polycrystalline PV modules. Open circuit voltage starts decreasing at cell temperature above 40 ℃. The average rate of decrease is observed to range from 0.023 V/℃ to 0.056 V/℃ for monocrystalline and 0.026 V/℃ to 0.061V/℃ for polycrystalline. For short circuit current, a slight increase is recorded in the range of 0.0018 A/℃ to 0.0025 A/℃ for monocrystalline and 0.0017 A/℃ to 0.0023 A/℃ for Polycrystalline module. Local wind speeds are noted to cause cooling, thus lowering the cell temperature. The fill factor is observed to decrease. The decrease rate ranges from 0.0024 /℃ to 0.0045 /℃ for monocrystalline and 0.0025 /℃ to 0.0047 /℃ for polycrystalline solar PV modules. Furthermore, a drop is observed in the efficiency at the rate ranging from 0.46 % to 0.51% /℃ for monocrystalline while that for polycrystalline is 0.47 %/℃ to 0.53 %/℃. For a 15 W solar module of the same ratings exposed to the same outdoor conditions, monocrystalline demonstrates better performance over the polycrystalline cell and, therefore, is best suited along the coastal region of Kenya with high ambient temperatures. However, in terms of costs per watt, polycrystalline is relatively cheap as compared to monocrystalline hence affordable and economical. Besides, polycrystalline has inherently lower carbon footprints compared to the monocrystalline.

References

Abu-Rahmeh, T.M., 2017. Efficiency of Photovoltaic Modules Using Different Cooling Methods: A Comparative Study. JPEE 05, 32–45. https://doi.org/10.4236/jpee.2017.59003

Al-Naser, Q.A.H., Al-barghooth, N.M., Al-Ali, N.A., 2012. International Journal of Engineering, Business and Enterprise Applications (IJEBEA) www.iasir.net. International Journal of Engineering 6.

Chakiri, S., Lamchich, M.T., 2021. Modelling effect of temperature and irradiance changes of Assa, Morocco on photovoltaic modules' performance. E3S Web Conf. 240, 03005. https://doi.org/10.1051/e3sconf/202124003005

Chander, S., Purohit, A., Sharma, A., Arvind, Nehra, S.P., Dhaka, M.S., 2015a. A study on photovoltaic parameters of mono-crystalline silicon solar cell with cell temperature. Energy Reports 1, 104–109. https://doi.org/10.1016/j.egyr.2015.03.004

Chander, S., Purohit, A., Sharma, A., Arvind, Nehra, S.P., Dhaka, M.S., 2015b. A study on photovoltaic parameters of mono-crystalline silicon solar cell with cell temperature. Energy Reports 1, 104–109. https://doi.org/10.1016/j.egyr.2015.03.004

Chandra, S., Agrawal, S., Chauhan, D.S., 2018. Effect of Ambient Temperature and Wind Speed on Performance Ratio of Polycrystalline Solar Photovoltaic Module: an Experimental Analysis 10.

Dubey, S., Sarvaiya, J.N., Seshadri, B., 2013a. Temperature Dependent Photovoltaic (PV) Efficiency and Its Effect on PV Production in the World – A Review. Energy Procedia 33, 311–321. https://doi.org/10.1016/j.egypro.2013.05.072

Dubey, S., Sarvaiya, J.N., Seshadri, B., 2013b. Temperature Dependent Photovoltaic (PV) Efficiency and Its Effect on PV Production in the World – A Review. Energy Procedia 33, 311–321. https://doi.org/10.1016/j.egypro.2013.05.072

Dwivedi, Y.K., Hughes, L., Kar, A.K., Baabdullah, A.M., Grover, P., Abbas, R., Andreini, D., Abumoghli, I., Barlette, Y., Bunker, D., others, 2022. Climate change and COP26: Are digital technologies and information management part of the problem or the solution? An editorial reflection and call to action. International Journal of Information Management 63, 102456.

El Achouby, H., Zaimi, M., Ibral, A., Assaid, E.M., 2018. New analytical approach for modeling effects of temperature and irradiance on physical parameters of photovoltaic solar module. Energy Conversion and Management 177, 258–271. https://doi.org/10.1016/j.enconman.2018.09.054

Fébba, D.M., Rubinger, R.M., Oliveira, A.F., Bortoni, E.C., 2018. Impacts of temperature and irradiance on polycrystalline silicon solar cells parameters. Solar Energy 174, 628–639. https://doi.org/10.1016/j.solener.2018.09.051

Genc, A.K.A.K.N., 2022. Effects of temperature and solar irradiation on the performance of monocrystalline, polycrystalline, and thin-film PV panels. International Journal on Technical and Physical Problems of Engineering (IJTPE) 254–260.

Green, M.A., Emery, K., Hishikawa, Y., Warta, W., 2011. Solar cell efficiency tables (version 37): Solar cell efficiency tables. Prog. Photovolt: Res. Appl. 19, 84–92. https://doi.org/10.1002/pip.1088

Hudișteanu, S.V., Țurcanu, F.E., Cherecheș, N.C., Popovici, C.G., Verdeș, M., Huditeanu, I., 2021. Enhancement of PV Panel Power Production by Passive Cooling Using Heat Sinks with Perforated Fins. Applied Sciences 11, 11323. https://doi.org/10.3390/app112311323

Irwanto, M., Daut, I., Sembiring, M., Ali, R.B., Champakeow, S., Shema, S., n.d. Effect of Solar Irradiance and Temperature on Photovoltaic Module Electrical Characteristics.

Kariuki, B.W., Sato, T., 2018. Interannual and spatial variability of solar radiation energy potential in Kenya using Meteosat satellite. Renewable Energy 116, 88–96. https://doi.org/10.1016/j.renene.2017.09.069

Khatibi, A., Razi Astaraei, F., Ahmadi, M.H., 2019. Generation and combination of the solar cells: A current model review. Energy Sci Eng 7, 305–322. https://doi.org/10.1002/ese3.292

Kidegho, G., Njoka, F., Muriithi, C., Kinyua, R., 2021. Evaluation of thermal interface materials in mediating PV cell temperature mismatch in PV–TEG power generation. Energy Reports 7, 1636–1650. https://doi.org/10.1016/j.egyr.2021.03.015

Kiprop, E., Matsui, K., Maundu, N., Mix, A., 2019. Can Kenya supply energy with 100% renewable sources? International Scientific Journal of Environmental Sciencehttp://environment. scientific-journal. com.

Manirambona, E., Talai, S.M., Kimutai, S.K., 2022. Sustainability evaluation of power generation technologies using Multi-Criteria Decision Making: The Kenyan case. Energy Reports 8, 14901–14914. https://doi.org/10.1016/j.egyr.2022.11.055

Musanga, L.M., Barasa, W.H., Maxwell, M., 2018. The Effect of Irradiance and Temperature on the Performance of Monocrystalline Silicon Solar Module in Kakamega. PSIJ 19, 1–9. https://doi.org/10.9734/PSIJ/2018/44862

Mwende, R., n.d. Photovoltaic (Pv) System Performance Forecasting and Modelling Using Real-time Observation and Weather Data.

Ndeto, M.P., Wekesa, D.W., Njoka, F., Kinyua, R., 2022. Correlating dust deposits with wind speeds and relative humidity to the overall performance of crystalline silicon solar cells: An experimental study of Machakos County, Kenya. Solar Energy 246, 203–215.

Pradhan, A., Panda, B., 2017. Experimental Analysis of Factors Affecting the Power Output of the PV Module. IJECE 7, 3190. https://doi.org/10.11591/ijece.v7i6.pp3190-3197

Pujan Jaiswal, S., Shrivastava, V., Palwalia, D.K., 2021. Opportunities and challenges of PV technology in power systems. Materials Today: Proceedings 34, 593–597. https://doi.org/10.1016/j.matpr.2020.01.269

Quansah, D.A., Adaramola, M.S., 2018. Aging and degradation in solar photovoltaic modules installed in northern Ghana. Solar Energy 173, 834–847. https://doi.org/10.1016/j.solener.2018.08.021

Rahman, M.M., Hasanuzzaman, M., Rahim, N.A., 2015. Effects of various parameters on PV-module power and efficiency. Energy Conversion and Management 103, 348–358. https://doi.org/10.1016/j.enconman.2015.06.067

Sargunanathan, S., Elango, A., Mohideen, S.T., 2016. Performance enhancement of solar photovoltaic cells using effective cooling methods: A review. Renewable and Sustainable Energy Reviews 64, 382–393.

Schwingshackl, C., Petitta, M., Wagner, J.E., Belluardo, G., Moser, D., Castelli, M., Zebisch, M., Tetzlaff, A., 2013. Wind Effect on PV Module Temperature: Analysis of Different Techniques for an Accurate Estimation. Energy Procedia 40, 77–86. https://doi.org/10.1016/j.egypro.2013.08.010

Shockley, W., Queisser, H.J., 1961. Detailed Balance Limit of Efficiency of *p-n* Junction Solar Cells. Journal of Applied Physics 32, 510–519. https://doi.org/10.1063/1.1736034

Singh, P., Ravindra, N.M., 2012. Temperature dependence of solar cell performance—an analysis. Solar Energy Materials and Solar Cells 101, 36–45. https://doi.org/10.1016/j.solmat.2012.02.019

Sinsel, S.R., Riemke, R.L., Hoffmann, V.H., 2020. Challenges and solution technologies for the integration of variable renewable energy sources—a review. Renewable Energy 145, 2271–2285. https://doi.org/10.1016/j.renene.2019.06.147

Smestad, G.P., Krebs, F.C., Lampert, C.M., Granqvist, C.G., Chopra, K.L., Mathew, X., Takakura, H., 2008. Reporting solar cell efficiencies in Solar Energy Materials and Solar Cells. Solar Energy Materials and Solar Cells 92, 371–373. https://doi.org/10.1016/j.solmat.2008.01.003

Tsuno, Y., Hishikawa, Y., Kurokawa, K., 2006. Translation Equations for Temperature and Irradiance of the I-V Curves of Various PV Cells and Modules, in 2006 IEEE 4th World Conference on Photovoltaic Energy Conference. Presented at the 2006 IEEE 4th World Conference on Photovoltaic Energy Conference, IEEE, Waikoloa, HI, pp. 2246–2249. https://doi.org/10.1109/WCPEC.2006.279619

Wambui, V., Njoka, F., Muguthu, J., Ndwali, P., 2022. Scenario analysis of electricity pathways in Kenya using the Low Emissions Analysis Platform and the Next Energy Modeling system for optimization. Renewable and Sustainable Energy Reviews 168, 112871. https://doi.org/10.1016/j.rser.2022.112871

Zhe, L.W., Irwan, Y.M., Irwanto, M., Amelia, A.R., Safwati, I., 2019. Influence of wind speed on the performance of the photovoltaic panel. IJEECS 15, 62. https://doi.org/10.11591/ijeecs.v15.i1.pp62-70

 ISSN: 2957- 7780

The Carbon Gap in Sustainable Housing and Infrastructure Development, a Lifecycle Approach for Climate Change and Adaptation in Developing Countries

Eric Wekesa Wanjala

Kenya Power and Lighting Co. Plc, P.O. Box 30099-00100 Nairobi, Kenya

Email: ericowanjala@gmail.com

Article History

Submission Date: 18th October 2023
Acceptance Date: 6th May 2024
Publication Date: 30th June 2024

Abstract

According to the United Nations Environment Program UNEP report on Infrastructure for Climate Action 2021, infrastructure contributes to **79%** of all greenhouse gas GHG emissions and accounts for **88%** of all adaptation costs. According to the International Development Infrastructure Commission Recommendation Report, 2020, an outlay estimated at **US$ 90** trillion is required for infrastructure development by developing and emerging countries for the period **2016-2030.** Considering that carbon constitutes over **79%** of GHG emissions, what volume of carbon emission is expected from housing and infrastructure developments in developing countries by 2030? How are the emissions being measured, tracked and or controlled nationally or at infrastructure project level? Developing countries have a huge deficit of the **17** United Nations Sustainable Development Goals (SDGs) yet to be implemented implying the largest Co2 emissions. Urgent policy framework and paradigm shift to less carbon-based solutions recommended at national and project level respectively. There is deficiency of data on expected carbon Co2/GHG emissions from planned and ongoing housing and infrastructure projects. Each project has a carbon footprint. Further, the type of construction, materials used, and volume of fuel consumed determines the level of carbon emissions. There is carbon contribution at each project milestone i.e., planning, commissioning, operations, and decommissioning. Use of carbon plan(s) with project life cycle (PLC) approach is an effective technique for estimation of expected carbon footprint and low emission strategy. The study explores and recommends a policy framework approach and application of carbon plans and project lifecycle model for infrastructure and building construction or development in Kenya as a climate change and adaptation.

Keywords: Carbon, Greenhouse Gas, Climate Change, Adaptation, Action, Lifecycle

1) Introduction

The world today is faced with troubling issues of rising accumulation of greenhouse gases and consequent global warming (*Tathagat and Dod, 2015*). According to the Paris Agreement 2015, a target was established to reduce the global temperature rise at between 1.5ºC to 2ºC above pre-industrial levels by 2030. According to the International Development Infrastructure Commission Recommendation Report, 2020, an outlay estimated at US$ 90 trillion is required for infrastructure development by developing and emerging countries for the period 2016-2030. Further, the United Nations (UN) conference on trade and development estimated US$ 2.5 trillion to address the investment gap in developing countries including infrastructure needs annually to realize the global goals. Noting that each infrastructure and building construction has a carbon footprint, higher carbon or greenhouse gas GHG emissions are expected from developing countries. This applies if business as usual situation is sustained in engineering developments.

Beside Kenya being a signatory and obligated to the Paris Agreement 2015 and use of Kenya Carbon Emissions Reduction Tool (KCERT 2050) to establish optimal energy pathway to realize reduction in GHG emissions by 32%, there exists a gap in carbon and GHG emission management i.e., tracking, measurement, accounting and reporting at project or activity level in Kenya. The application of the KCERT2050 tool is only limited to modelling energy consumption and corresponding annual GHG or carbon emissions for policy considerations. The identified gap which is lack of mechanism to project, measure, track and account for carbon emissions in projects impacts sector level performance and reporting on carbon or GHG emissions. The study focused on construction sector where housing and infrastructure constructions are highest. Buildings are responsible for 35% of global energy consumption and 38% of global energy-related CO2 emissions *(United Nation Environment Programme (UNEP), 2020)*. Kenya's carbon or GHG emission data is primarily collected from the operational or use phase of most projects implemented across various sectors. This is inadequate as it lacks life cycle carbon contribution. For green construction, project life cycle PLC approach with life cycle assessment LCA is commended for wholistic determination of carbon footprint (CF) [15]. The deficiency of data on carbon estimates at project determinative stages i.e., initiation, planning, design, approval, commissioning, decommissioning and disposal impedes emission control over the PLC [1, 8]. The LCA is beneficial to decision-making process in that it can be used to review sustainability initiatives throughout the entire

 ISSN: 2957- 7780

life cycle of the infrastructure or building, including the design, detailing, delivery and disposal phases. A number of studies in North America, Europe and Japan used LCA as a useful tool for determining the carbon footprint and embodied energy consumption in assessing the environmental performance of buildings *(Lemay, 2011, Bribián et al., 2009, Junnila and Horvath, 2003, Junnila et al., 2006, Suzuki and Oka, 1998)*. Various construction activities lead to environmental pollution through land clearing, equipment's engine emissions, demolition, burning, and use of dangerous chemicals, among others according to *(Adebowale Philips Akinyemi et al., 2017).* Lack of accurate accounting and tracking emissions as identified in the gap further risks loss of credit opportunities in carbon markets. Effective accounting of carbon emission requires continual evaluation of variances during the entire PLC comparing baseline estimates established at project initiation (planning) versus actual levels measured during construction, operation or use phase. Building construction accounts for an estimate 40% of global energy-related emissions.

The study used qualitative techniques and reviewed literature associated with reduction of carbon or GHG emissions in construction project with notable case study of buildings [2,3,4,5,6,8] and port construction [15]. The study recommends use of project life cycle PLC approach with incorporation of life cycle assessment (LCA) [2,3,6,8,13]. PLC assures effective projections of carbon or GHG emissions for project life cycle however LCA established embodied energy analysis and emissions for materials (with existing carbon values or coefficients) and components used at different stages of project life cycle [1]. Study findings to improve policy framework, adoption of carbon plans, and establish inventory for sustainable materials (carbon coefficients) etc. These will improve carbon or GHG management through introduction of carbon plans in project approval and funding as part of sustainability, accurate reporting on carbon or GHG emissions and projections, increased opportunities in carbon markets for infrastructure and housing projects by the Government of Kenya, public and private sector players and non-governmental institutions. Stakeholders in regulatory, standards and capacity building notably the Institution of Engineers of Kenya (IEK), the Engineers Board of Kenya (EBK) and Environment Institute of Kenya (EIK), ministries and other agencies etc. will use the findings to advance low emission strategies and capacity at sector and institutional levels for engineering development and success of NDC targets.

1.1 Carbon Quantifications

 ISSN: 2957- 7780

Carbon footprint is a measure of the exclusive total amount of carbon dioxide emission that is directly and indirectly caused by an activity or is accumulated over the life stages of a product, including activities of individuals, populations, governments, companies, organizations, processes, industrial sectors etc. *(Wiedmann and Minx, 2008).* Outstanding merit for CF calculation is that it is possible to adapt it to any project [15]. All sectors should be obliged to perform CF calculations for posterity more so construction sector whereby significant impact on the environment due to large earth movements, the treatment of compound materials, and land modification is prevalent. Globally, 20% of carbon and GHG emissions are generated by construction sector being the first in material(s) consumption. LCA methodology allows calculation, evaluation, and interpretation of the generated emissions during the lifetime of an infrastructure or building thereby showing the GHG produced during all the project phases [2,3,6,8,13]

1.2 Project Life Cycle (PLC) for Carbon Reduction in Construction Projects.

LCA allows the calculation, evaluation, and interpretation of the generated carbon emissions during the lifetime of an infrastructure, building thereby showing the GHG produced during all the project phases [2,3,6,8,13]. PLC acts to establish the start and end of a project [1]. The four stages in PLC are initiation or conceptualisation, planning or design, execution or implementation, and termination or closure [1]. Green and conventional projects are similar with one notable dissimilarity. Green construction model focuses on sustainability and environment friendly requirements unlike conventional. PLC requires low carbon emission or GHG strategies to be considered at the project initiation and concept stage [1]. These benefits are transferred inter-stage to the end of the project [1]. Each project stage in a green construction concept interrelates with the next for transfer of green benefits or low carbon gains. It is expected that an accumulated gain of green benefits is realizable at the end of the PLC [1].

1.3 The Initiation phase / Project Initiation

At this stage conceptualization or concept development incorporates low carbon planning. This impacts the design concept and whole series of construction activities to the project end of life [1]. The owner sets a green centric project strategy leading to green designs, shapes, technology, and construction. Green model influences the process(s) hence control project financing, team, cost, quality, and time [1]. The people qualifications include training on

 ISSN: 2957- 7780

sustainability and or low emission. Stage deliverable(s) comprises documentation on tasks, responsibilities, project details (name, budget, appointments etc).

1.4 The Design Phase / Project Planning

The most significant stage of PLC that projects expected carbon or GHG emissions associated with the gradual implementation of a projects [1]. Green drawings, designs and building specifications done for low carbon. Consultancy or expertise sourced for complex projects to avert risks of poor designs causing changes in project scope, and strategy, repetitive work, delays in schedule, and cost swelling [1]. Green centric design comprises two main aspects: (1) Life Cycle Assessment (LCA) and (2) Eco-Conscious Design (ECD) [1]. LCA is key in determination of embodied carbon hence critical for material selection [2,3,6,8,13]. Green centric planning stage assures deliverables that transfer benefits to construction stage in form of project structure and team, detailed design drawing(s), task scope(s), technical data, project schedules, work schedules, material / spending schedules, procedures, etc.

1.5 The Construction Phase / Project Execution

Dependent on the deliverables from initiation, planning and design stage [1]. Major risks occur that change project scope at this stage notably force majeure, resource and finance constraints, contractual and stakeholder conflicts etc [1]. Key activities are supply of materials, construction methods, use of tools and labour, waste management and upkeep prior to handover. These influence emissions mainly choice of materials and transportation. Cradle to gate, cradle to site and cradle to handover processes apply in supply of materials for low emission objectives. Heavy equipment consume fossil-derived oils hence higher footprint. Labour efficiency during construction activities determines carbon reduction as carbon is calculated on the activities of workers during the project. Waste management and residual cleaning of buildings and maintenance of buildings is the ultimate activity of the project life cycle [1]. Direct carbon-based wastes originate from the combustion process of material waste at the project site while indirect waste come from the process of transporting solid waste discharges to landfill sites. Research shows that construction industry produces large amounts of waste and more than 50% of the waste material is deposited in the final dump [1]. Nearly 26% of landfill sites are occupied by construction waste [1]. Quality and control are key at this stage of construction. Deliverables are project documentation i.e., reports comprising of change management, tests, inspections, risks and meetings.[1].

 ISSN: 2957- 7780

1.6 Project Handover / Closure / Operational / Maintenance

Final examination of works in respect to the contractual scope is done upon completion of construction stage. Detailed checklists are used containing all items of work including pending item(s) capture in defects liability period. Once all corrective actions are effected, it is necessary to review all construction activities before the work is declared complete and handover to owner. The final inspection should involve all key stakeholder representatives. The final deliverable is documentation comprising all control documents in the construction phase, final drawing (as built drawing), and the operating manual and the handover report. Green construction concept requires an evaluation of carbon and GHG emissions is performed to account for variances in actual project emissions from projections at initiation.

1.7 Carbon Emission in Construction

Infrastructure and buildings constructions consume the largest volumes of materials. This makes them lead in carbon emissions due to high embodied energy in materials used. Embodied Energy corresponds to the energy expended by all processes associated with the production of building materials and their components. This includes mining, manufacturing materials and equipment, assembly and transportation etc. Therefore, total contained energy during construction of infrastructure and buildings is directly proportional to the level of complex material used and process(s) involved. In typical construction(s) highest emissions of CO2 arise from the use of concrete, aluminium and steel. These have high contained energy levels. This imply the contained energy is as an indicator of the overall environmental impact of building materials and systems. Carbon energy is the energy spent during the construction process. It is consequential energy from the manufacturing, distribution / supply, transportation and equipment used during construction work. Generally, it comes from combustion (fossils), such as in factories and vehicles. Embodied carbon is calculated by KgCO2 / Kg unit of material or based on its functional unit using kgCO2 / m3 of material or kgCO2 / m2 of material, where each material has different energy values.

2) Methodology

This study used qualitative methods Literature associated with reduction of carbon emission Literature on select cases associated with low carbon emission strategies were reviewed as follows building construction in Western Australia [4], Port Construction [15], Industrial Park

in China [7], storey building Växjö, Sweden [8]. The study analysed and divulged findings and interpretations of previous research on reduction of carbon emissions. The study attempted to categorize the content of the research into the project life cycle (PLC) scope. Grounded on this opinion, the formulation of research problems associated with carbon emission in relation to PLC drawn clearly.

The study adopted two steps to improve the quality and reliability of the literature review sources (Alwan et al., 2017). Firstly, using organized keywords in well-established and high-quality scientific journals and repositories. Key words were used to collect materials for the study. The study adopted two steps to improve the quality and reliability of the literature review sources (Alwan et al., 2017). Firstly, using organized keywords to collect information in well-established and high-quality scientific journals and repositories. Lastly the literature review of carbon emission reduction strategies from industry, Governments and international agency reports, Internet and media publications, etc. Further secondary data sources in the form of a literature review consisting of industry, Government and international agencies reports, internet and media publications, etc were used. Purposive sampling and descriptive analysis methods used in data collection however analysis and interpretation done by mapping each of the research topics of the journal in tabular form. Table 1 below comprise results of research journal mapping on carbon emission reduction strategy reviewed in PLC as below.

3) Results

Table 1. Research On Carbon Emission Decrease Strategies Reviewed in The Project Life Cycle (PLC).

Reference	**Yr**	**Location**	**Type of Research / Analysis**	**Type of Construction**	**Parameter Studied**	**Project Life Cycle – PLC**			**Case Study**
						Init	**Design**	**Const**	
Pomponi & Moncaster	2016	-	LCA	Building	CO2	-	-	X	Construction

Atmaca & Atmaca	2015	Turkey	LCA (LCEA & LCCO2A)	Building	Energy & CO2	-	-	X	Building const, operation & Demolition
Baek et al.	2013	-	LCA (LCCO2)	Building	CO2	-	X	X	Design, Const, Operation, Disposal
Dong et al.	2013	SETDZ, China	Hybrid LCA	Industrial Park	CO2 / GHG	-	-	X	Operations
Pomponi & Moncaster.	2016	European Union-EU	LCA,	Building	CO2	-	X	X	Design, Const, Operation, Disposal
Biswas, 2014	2014	Western Australia	LCA	Building	CO2	-	X	X	Design, const, Operation, Disposal
Chou & Yeh	2015	-	LCA & Monte Carlo	Building	CO2	-	X	X	Design, const, Operation, Disposal
Gustavsson et al.	2010	Sweden	LCA & Bottom-up	Building	CO2	-	X	X	Construction

Source: (Author,2023), NB: Range in years 2010 < > 2016

LCA concept evaluates the resources inputs, including energy, water and materials, and environmental loadings including CO2 emissions and wastes of a building during different phases of the life cycle. Equation

$$\boldsymbol{I}=\{I\ (extraction)+I\ (manufacture)+I\ (Onsite)+I\ (Operation)+ I\ (Demolition)+I\ (Recycling)+I\ (Disposal.)\} \quad (1)$$

where I represent the life cycle environmental impact.

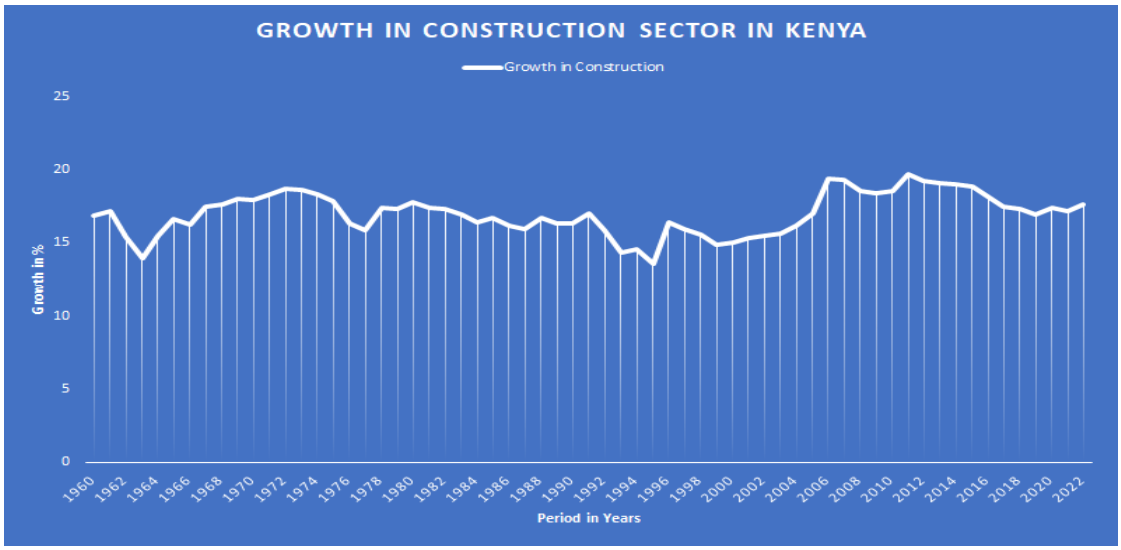

Figure 1: Growth in construction sector in Kenya period 1960 to 2022. (Source: data.worldbank.org)

It is deducible from figure 1 above that construction sector in Kenya had a growth rate of 17.7% in the year 2022. Construction industry in Kenya is expected to grow by 7.7% reaching KES 973 billion-in 2023[11]. The construction output in the country is projected at KES 1,279.1 billion by 2027[11].The industry is expected to register annual average growth rate of 5.7% from 2023 to 2026, supported by investments in transport, electricity, housing, and manufacturing [10] Additionally construction are 250,000 new affordable houses every year through PPPs, new 'level six' hospitals in six new sites, a 100,000km fiber optic connectivity network, and building a 700km road along the Kula, Isiolo, Mawe-Modogashe-Samatar-Wajir-Kutulo-El Wak-Ramu corridor, etc. [10]. All these constructions will increase the carbon footprint if business as usual scenario persists

4) Discussion

Table 1 above illustrates the literature-based review on carbon emission reduction relation to activity on the project life cycle PLC. From the 8 pieces of literature, researchers adopted the LCA method. A case of hybrid LCA as well as combinations of LCA with other analytical models noted i.e., Monte Carlo simulation, and Bottom-up analytical techniques. LCA is prevalent for analysis of embodied energy and consequent carbon emissions over a material, product or item lifecycle. This is useful for emission reduction strategies in construction noting most materials used emit variant levels of carbon dependent on embodied energy. It is

noteworthy that PLC requires low carbon strategies be incorporated at the project initiation stage. The 8-research literature reviewed did not explicitly demonstrate in PLC activity.

Table 3 Summary of activities recommended under each stage of the PLC for low carbon model.

No	Initiation	Design	Construction and handover
1	Stakeholder awareness for low carbon planning	Emphasis on low carbon designs with attention to optimizing the structure / building element.	Optimize and go green procurement or green supply chain for faster acquisition of material and equipment distribution
2	Government facilitate dissemination of knowledge on low carbon strategies.	Prioritization of low carbon building materials.	Reduction of emissions through machine optimisation and increased operator expertise.
3	Government and International institution establish environmentally sound building standards planning the building	Design for ease of disassembly	Best choice of construction method to increase efficiency in time, cost and material to have low waste generation.
4		Design concept to include use of renewable energy.	Use of eco-labelled materials in every building component for carbon reduction
5		Use of PLC and LCA in selection of low carbon material i.e., cement, steel & ceramic important.	Optimisation of energy, electricity, gas and water and material utilization in every construction operational activity
6		More innovative low carbon designs.	Adoption of the concept of reduce, reuse and recycle in waste management.
7			Utilize new technologies and renewable energy for reduction of carbon emissions
8			Engineer building structures using green cement and utilize wood materials to further reduce carbon emissions

Source: Author, 2023

5) Conclusions

The Government has prioritized affordable housing and infrastructure development in Kenya. It is noteworthy that Kenya is a signatory to the Paris Agreement 2015 and hence obligated through NDC to ambitiously achieve below 2^{o}C temperature rise by 2030. Each project regardless of scope has a carbon footprint. The carbon emissions reduction measures in the construction life cycle start from the initiation stage where the project owner has great authority in determining the whole series of construction activities [1]. The PLC approach ensures that putting forward the concept of low carbon in the initiation phase, the same is passed to successive stages of PLC herein low carbon design and further low carbon construction [1]. Therefore, the concept of low carbon will be developed on low carbon operational, low carbon dismantling and recycling following the life cycle of the building. In addition, current issues on the taxation of carbon in each sector including construction will emphasise the stakeholders to prefer the concept of low carbon development as well as sustainable environmental insight.

However, priority should also be placed on the selection of sustainable construction management techniques, use

of heavy equipment, production of construction material, human activities at the site, and transportation *(Hong et al., 2014).* Furthermore, greater emphasis needs to be given to macro-level management, international collaboration, and the development of concepts, technologies, and standards related to low-carbon construction due to their significant contributions towards net-zero energy building development *(Shi et al., 2015).*

References

1. Agung Wibowo, M., Uda, S. A., & Zhabrinna. (2018). Reducing carbon emission in construction base on Project Life Cycle (PLC). MATEC Web of Conferences, 195, 06002. https://doi.org/10.1051/matecconf/201819506002
2. Atmaca, A., & Atmaca, N. (2015). Life Cycle Energy (LCEA) and carbon dioxide emissions (LCCO2A) assessment of two residential buildings in Gaziantep, Turkey. *Energy and Buildings*, *102*, 417–431. https://doi.org/10.1016/j.enbuild.2015.06.008
3. Baek, C., Park, S.-H., Suzuki, M., & Lee, S.-H. (2013). Life cycle carbon dioxide assessment tool for buildings in the schematic design phase. Energy and Buildings, 61, 275–287. https://doi.org/10.1016/j.enbuild.2013.01.025
4. Biswas, W.K. (2014) 'Carbon footprint and embodied energy consumption assessment of building construction works in Western Australia', International Journal of Sustainable Built Environment, 3(2), pp. 179–186. doi:10.1016/j.ijsbe.2014.11.004.

5. Chau, C.K. et al. (2012) 'Assessment of CO2 emissions reduction in high-rise concrete office buildings using different material use options', Resources, Conservation and Recycling, 61, pp. 22–34. doi:10.1016/j.resconrec.2012.01.001.
6. Chou, J.-S. and Yeh, K.-C. (2015) 'Life cycle carbon dioxide emissions simulation and Environmental Cost Analysis for building construction', Journal of Cleaner Production, 101, pp. 137–147. doi:10.1016/j.jclepro.2015.04.001.
7. Dong, H., Geng, Y., Xi, F., & Fujita, T. (2013). Carbon footprint evaluation at Industrial Park Level: A hybrid life cycle assessment approach. *Energy Policy*, *57*, 298–307. https://doi.org/10.1016/j.enpol.2013.01.057

Barandica, J.M.; Fernández-Sánchez, G.; Berzosa, Á.; Delgado, J.A.; Acosta, F.J. Applying life cycle thinking to reduce greenhouse gas emissions from road projects. J. Clean. Prod. 2013, 57, 79–91. [CrossRef]

Hauschild, M.Z. Introduction to LCA methodology. In Life Cycle Assessment: Theory and Practice; Springer: Cham, Switzerland, 2017.

8. Gustavsson, L., Joelsson, A. and Sathre, R. (2010) 'Life cycle primary energy use and carbon emission of an eight-storey wood-framed apartment building', Energy and Buildings, 42(2), pp. 230–242. doi:10.1016/j.enbuild.2009.08.018.
9. Herda, G., Sangori, R., & Bock, M. (2017). Low cost, low carbon, but no data: Kenya's struggle to develop the availability of performance data for building products. Procedia Environmental Sciences, 38, 452–460. https://doi.org/10.1016/j.proenv.2017.03.136
10. Kenya construction market size, trends and forecasts by sector - commercial, industrial, infrastructure, energy and utilities, institutional and residential market analysis, 2022-2026. ReportLinker. (n.d.). https://www.reportlinker.com/p06286213/Kenya-Construction-Market-Size-Trends-and-Forecasts-by-Sector-Commercial-Industrial-Infrastructure-Energy-and-Utilities-Institutional-and-Residential-Market-Analysis.html
11. Kenya Construction Industry Databook Series Q1 2023 update: Sector to grow at 7.1% annually through 2027 - researchandmarkets.com (2023) Business Wire. Available at: https://www.businesswire.com/news/home/20230214005532/en/Kenya-Construction-Industry-Databook-Series-Q1-2023-Update-Sector-to-Grow-at-7.1-Annually-Through-2027---ResearchAndMarkets.com#:~:text=According%20to%20the%20publisher%2C%20construction,story%20in%20Kenya%20remains%20intact. (Accessed: 14 September 2023).
12. Mwende, J. (2023, May 17). List of top construction projects in Kenya – 2023. CK. https://www.constructionkenya.com/999/major-construction-projects/
13. Müller, L. J., Kätelhön, A., Bachmann, M., Zimmermann, A., Sternberg, A., & Bardow, A. (2020, January 23). A guideline for life cycle assessment of Carbon Capture and Utilization. Frontiers. https://www.frontiersin.org/articles/10.3389/fenrg.2020.00015/full
14. Pomponi, F. and Moncaster, A. (2016a) 'Embodied carbon mitigation and reduction in the built environment – what does the evidence say?', *Journal of Environmental Management*, 181, pp. 687–700. doi:10.1016/j.jenvman.2016.08.036.
15. Saravia de los Reyes, R., Fernández-Sánchez, G., Esteban, M. D., & Rodríguez, R. R. (2020b, October 12). Carbon footprint of a port infrastructure from a life cycle approach. MDPI. https://www.mdpi.com/1660-4601/17/20/7414/htm
16. *@iLabAfrica*. iLabAfrica. (n.d.). http://www.ilabafrica.ac.ke/

Assessing Energy Budget Disruptions and the Implications for Hydrology, Climate, and Engineering Practices in the Nzoia River Basin Using MERRA-2 and CERES Satellite Instruments

Stephen Mureithi Kivuti

Moi University, P.O. Box 3900-30100 Eldoret, Kenya

Email: mureithikivuti@gmail.com

Article History

Submission Date: 10th October 2023
Acceptance Date: 6th May 2024
Publication Date: 30th June 2024

Abstract

Understanding the water and energy budget dynamics in watersheds is crucial for sustainable water resource management and climate change mitigation. The primary energy source for the energy budget is shortwave radiation from the sun, which is either absorbed by the Earth's surface and atmosphere or reflected out into space. Absorbed shortwave radiation transmutes into longwave radiation, which drives the energy and water budgets. For a steady climate, the total shortwave radiation coming into the atmosphere has to be roughly equal to the sum of the shortwave radiation reflected out and the longwave radiation that escapes into space. Disruptions in this balance, such as greenhouse gas emissions and land modifications, can have severe implications for the climate and water budget. This research focuses on assessing the energy budget of the Nzoia River Basin and the implications for hydrology, climate change, and engineering practices. To investigate these disruptions, satellite data from CERES instruments (located in TRMM, Terra, Aqua, S-NPP, and NOAA-20 satellites) and the MERRA-2 dataset (collected from GEOS-5 satellites) were utilized. These datasets provided measurements of longwave and shortwave radiation, as well as meteorological data. The analysis revealed a growing imbalance in the energy budget, primarily attributed to human activities. An empirical relationship (incorporating meteorological variables and solar radiation) estimating surface fluxes within the Nzoia River Basin was developed. This relationship highlighted the degradation of the water budget due to disruptions in the energy budget and indicated potential climate change effects resulting from human activities. Correlations were observed between the clearance of natural vegetation, changes in surface

albedo, latent heat flux, and rising temperatures. Additionally, a decrease in longwave radiation escaping from the atmosphere suggested elevated greenhouse gas concentrations. Developed data forecasts indicate that the atmospheric energy budget imbalance is projected to worsen, leading to severe consequences such as prolonged droughts and intense floods for residents in the basin. Urgent management changes are essential to mitigate the adverse impacts of climate deterioration and enhance the basin's resilience to climate change.

Keywords: Energy Budget, Water Resource Management, Climate Change Mitigation, CERES, MERRA-2, Empirical Relationship, Greenhouse Gas Emissions, Climate Change Resilience

1) Introduction

150 million miles away, an ongoing PP (proton-proton) chain reaction continuously results in the release of enormous amounts of energy (Iliadis, 2015). The giant nuclear reactor where this process is carried out is called the sun. The energy released in the PP chain reaction eventually escapes from the sun. Due to the high temperatures in the sun, this energy is majorly high-frequency shortwave radiation (Gettelman & Rood, 2016). Reaching the earth in 8 minutes, this incident radiation is the source of energy that, in one form or the other, is the key driving force for life, the weather, and all processes on which life depends. Consequently, the rhythms of the sun have shaped life on Earth and its evolutionary trajectory since life first came into existence 3.8 billion years ago in the late heavy bombardment; and it will continue to do so for billions of years to come (Stüeken, et al., 2020).

All the energy that reaches the earth at the top of the atmosphere (top of atmosphere downward radiation) determines the climate of an area. By interacting with the atmosphere and the earth, it forms a balance between the energy that comes into the earth and the radiant energy that escapes from the earth. This balance between energy income and expenditure is known as the energy budget. It has been determined that, on average, 314 Watts per square meter (W/m^2) falls on every square meter of the earth's outer atmosphere; which given the surface area of the earth's outer atmosphere ($2 * 10^{15} m^2$) results in $6.8 * 10^{17}$ Joules per second (J/s) hitting the planet every second. It is important to keep in mind that this energy represents the average solar energy. In reality, this amount varies in space and time depending on your location on

Earth, and this variation is the key driving force of the incredible variety we have on Earth in terms of the seasons, ecosystems, and differing climate patterns.

Quantification of the energy budget into percentages is very useful for further analysis. The top of atmosphere downward radiation can be quantified as 100%; making it possible to easily track how the energy budget behaves in the earth's atmosphere system. About 54% of this incident solar radiation is high-frequency shortwave radiation (known as shortwave downward irradiance) that reaches the earth's surface (Trenberth, et al., 2009). The rest interacts with the atmosphere, with 23 per cent being directly absorbed into the atmosphere and 23% is reflected by the atmosphere (mainly clouds) back out into space (Trenberth, et al., 2009). Once this 54% hits the earth's surface, about 7% of the initial solar radiation is reflected out into the atmosphere depending on the surface albedo (reflectance) of the surface of the earth at the point of incidence (Trenberth, et al., 2009). For instance, dark surfaces like road surfaces (asphalt) have a low albedo and absorb much of this energy while bright surfaces like snow caps on mountains have a high albedo and thus reflect much of this energy. This means that about 30% of shortwave radiation (known as shortwave upward irradiance) is reflected out into space.

It is the energy that is absorbed into the earth (about 47%) that is crucial for determining the climate of the earth (Trenberth, et al., 2009). Of this energy, around 5% is lost to the earth as thermal energy while 23% escapes the earth as latent heat of evaporation (Trenberth, et al., 2009). Once the water vapour condenses, this latent heat is released into the atmosphere. However, once absorbed, the majority of the energy that moves within the atmosphere and the earth is long wavelength relatively low-frequency radiation (Gettelman & Rood, 2016). This can flux back and forth between the atmosphere and the earth more than once before it is released into the atmosphere. Of this longwave radiation, about 12% of the initial solar radiation passes right through the atmosphere from the Earth and out into space as longwave radiation (Trenberth, et al., 2009). At any given time, the earth radiates slightly more energy into the atmosphere in longwave radiation (about 106% of Top of atmosphere shortwave downward irradiance) than the initial shortwave radiation being absorbed from the sun (Trenberth, et al., 2009). This is possible because some of the energy that is captured by the atmosphere from the earth is radiated back to the earth (about 97%). This exchange between

the atmosphere and the earth allows total fluxes to add up to more than the energy that entered into the system initially. To complete the cycle, some of this longwave radiation (58%) is radiated from the atmosphere and back out into space (Trenberth, et al., 2009). The typical energy budget for a stable atmospheric system such as the one described above is depicted in Figure 1:

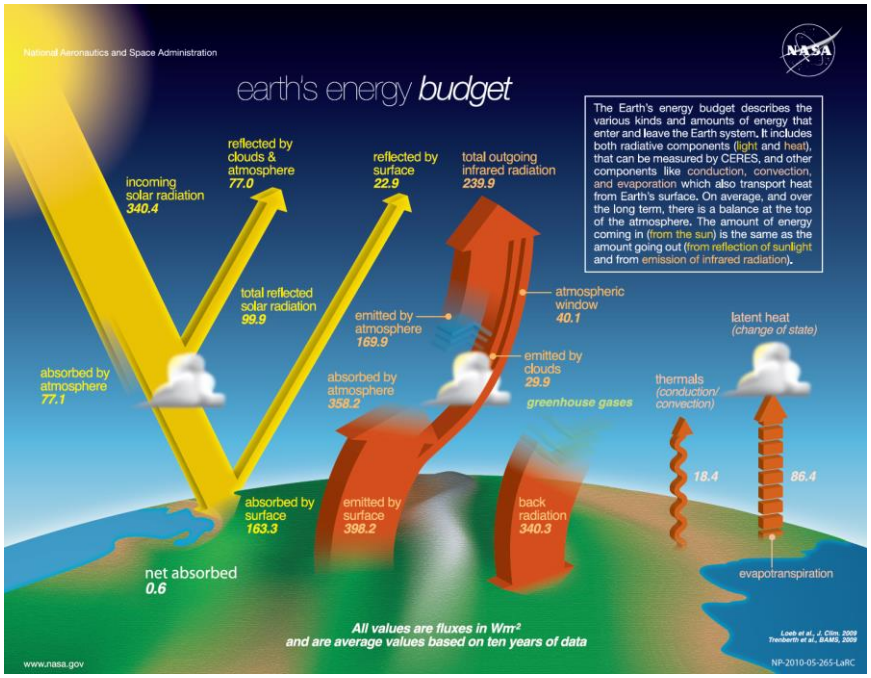

Figure 1: Earth's Energy Budget for a Typical Ideal Situation. Source: (Atkinson, 2017)

While the total amount of energy fluxing between different parts of the earth's system does not need to add up to the incident solar energy, physics determines that a stable system has a net energy loss or gain of zero. Therefore, the sum of the 30% of shortwave radiation reflected out into space and the 12% and 58% of longwave radiation radiated out to space (see the description in the previous paragraph describing the behavior of longwave radiation in the atmosphere) should total 100% if the climate is to remain steady. More energy escaping from the earth's system than is coming in would indicate a cooling climate while less energy escaping when compared to the incident radiation would infer a warming climate.

The large and constant exchange of longwave radiation between the earth’s surface and the atmosphere is what keeps the earth’s climate within the range that supports life. This is dependent on the presence of greenhouse gases in the atmosphere such as Carbon (IV) Oxide,

methane, and water vapour to keep energy from escaping from the earth. Greenhouse gases have the property of allowing shortwave radiation to pass through them and into the Earth, but they absorb the longwave radiation escaping to space and release some of it back into the Earth. This results in an effect where the majority of shortwave irradiance from the sun can get into the system, but very little longwave irradiance escapes back out of the system. It is important to also keep in mind that while clouds are understood to reflect the incident shortwave irradiance, it has been determined that clouds (particularly high-lying clouds like cirrus) contribute to the greenhouse effect by absorbing longwave upward irradiance (Katagiri, et al., 2013). However, the net energy reflected by the clouds normally supersedes the net energy absorbed. Therefore, due to the greenhouse effect, the current global temperatures average at 14^0 C rather than the – 19^0 C average that would be the case if greenhouse gases were not present in the atmosphere (Cassia, et al., 2018).

However, since the Industrial Revolution, human activity has resulted in drastic changes to the land cover and concentrations of greenhouse gases in the atmosphere. Global concentrations of greenhouse gases such as Carbon (IV) Oxide and methane have risen significantly over time (Musau, et al., 2015). Similarly, humans have interfered with the natural systems and have changed the surface albedo of the earth by clearing the land for their economic purposes. Additionally, the degradation of the land has led to a loss of important vegetation like forests which store carbon and therefore manage the levels of Carbon (IV) Oxide in the atmosphere.

Nzoia basin's importance in the region and the country has resulted in not only the degradation of the land but in the increase of greenhouse gas concentrations in the atmosphere as activities to exploit the natural abundance in the basin have kept increasing over the years. Over the decades, the basin has seen its forest and natural vegetation rapidly giving way to human activities such as agriculture, urbanization, and development of infrastructure (Moses, et al., 2015). In the Endebess area (close to Kitale and Mt. Elgon region) in the North West part of the basin, for instance, an average of 59.1 kilotons of Carbon (IV) Oxide was released every year between 2001 and 2022 into the atmosphere due to the result of tree cover loss in the area (Harris, et al., 2021). This totaled to a release of 1.3 Megatons of Carbon (IV) Oxide into the atmosphere. Similarly, Trans-Nzoia County in the upper reaches of the basin has resulted in the loss of natural diversity to local croplands (Kipkulei, et al., 2022). Similarly, lower reaches

of the basin in the South Western part have resulted in a loss of natural diversity to uses such as human settlement, agriculture, infrastructure (such as dams) and the mining of sand (Moses, et al., 2015). This trend has been exacerbated all over the basin.

These disruptions of the natural systems in the basin have affected the energy budget in the basin, which has resulted in a change in the climate patterns among many other negative impacts this has brought about. For instance, the increase in the severity of floods and droughts in the area has resulted in massive losses in terms of human lives and property (Mureithi, et al., 2022). If no measures are taken to change this situation, it is predicted that disastrous consequences such as these will become more frequent and severe in the watershed, and will affect all sectors ranging from a loss of quality drinking water to losses in agriculture due to the damaging effects of unpredictable weather (Musau, et al., 2015).

To come up with a solution to these disruptions in the water budget, it is important to understand them. This research therefore intended to provide a solution to the aforementioned issues by analysing the water budget for the basin. It focused on assessing the energy budget of the Nzoia River Basin and the implications for hydrology, climate change, and engineering practices. To investigate these disruptions, satellite data from CERES instruments (located in TRMM, Terra, Aqua, S-NPP, and NOAA-20 satellites) and the MERRA-2 dataset (collected from GEOS-5 satellites) were utilized. These datasets provided measurements of longwave and shortwave radiation, as well as meteorological data.

2) Materials and Methods

2.1 Study Area

Upon delineation of a digital elevation model in ArcGIS, the study area was determined to be about 12,700 km^2. In decimal degrees, the watershed lies within longitudes 33.5° E and 36° E and latitudes 1.5° N and −0.2° S. Nzoia basin is entirely located in Kenya, where it straddles Uasin Gishu, Trans Nzoia, Kakamega, Bungoma and Busia counties (Figure 2).

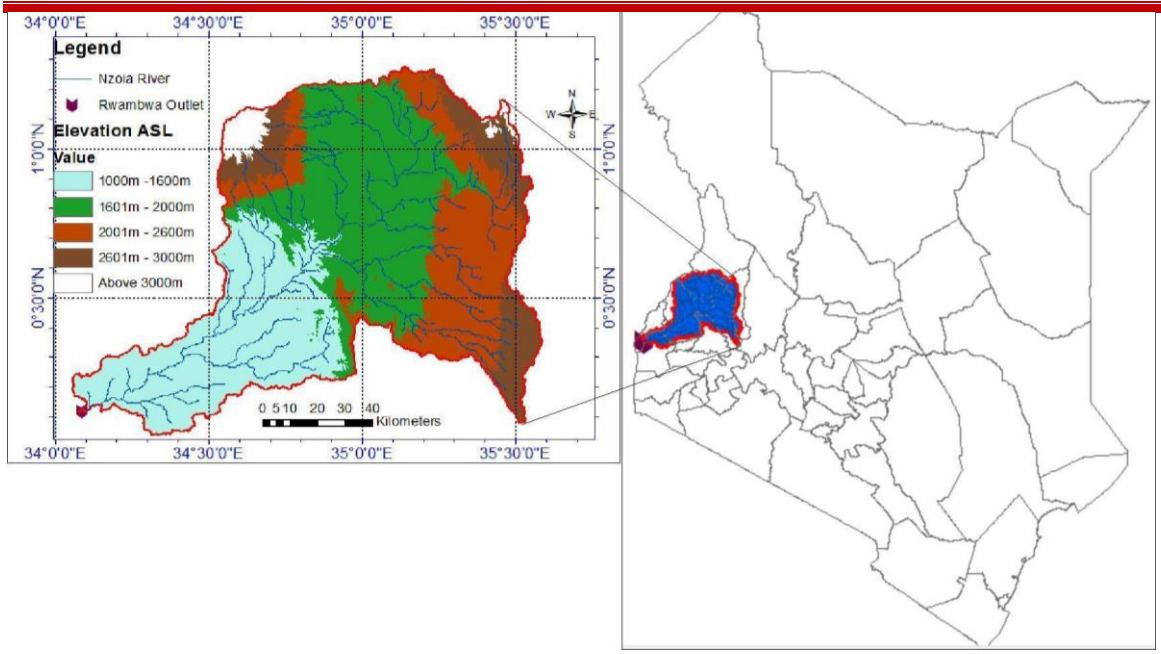

Figure 2: Nzoia basin with location and physiographic regions indicated (a delineated from a DEM for the study)

From a physiographic and land use point of view, the basin has four distinct ones: a highland zone (2,300–2,850 m Above Sea Level {ASL}), a plateau zone (1,900–2,300 m ASL), a transition zone (1,600–1,900 m ASL) and a lowland zone (1,000 m–1,600 m ASL). From the digital elevation model used in the study, anything above 2,850 m ASL was taken to represent areas occupied by the mountain peaks. These areas had the maximum elevation for the watershed of up to 4,296 m ASL. The highest peak to the north-western part of the basin is Mount Elgon while to the north-eastern part is the Cherangani Hills.

When it comes to land use, the highland zones are forested, but severe land degradation is threatening these highland forests. The plateau zone is the major maize and dairy farming area in the basin. The transition and lowland are characterized by a mix of sugarcane and small-scale farming. The lowland areas are generally flat and consequently flood-prone and swampy. Across the basin, there is evidence of encroachment of human settlement, human activity, infrastructure and urban areas into the natural landscapes of the catchment.

2.2 Data Collection

As limited by data availability, the data for the energy budget was acquired from the CERES instruments and MERRA-2 datasets were acquired from the NASA observatory, NASA

Prediction of Worldwide Energy Resources (POWER NASA). The data was collected for 13 stations as shown in Table 1. These stations were chosen to make their distribution across the basin as even as possible.

Table 1: Choice of Stations

Station ID	**Station Name**	**Latitude (decimal degrees)**	**Longitude (decimal degrees)**
8934059	Uholo	0.185	34.304
8934134	Bungoma	0.583	34.567
8934096	Kakamega	0.283	34.767
8934072	Nandi	0.150	34.933
8934061	Malava	0.446	34.851
8934016	Lugari	0.667	34.900
8935181	Eldoret	0.533	35.283
8935170	Lukamanda	0.633	35.050
8834013	Adc	1.033	34.800
8934008	Kiminini	0.900	34.917
8834098	Kitale	1.000	34.983
8935104	Kaptagat	0.867	35.500
8935137	Timboroa	0.067	35.533

2.3 Data analysis

For the data acquired, any dataset with missing values was denoted as -99. Therefore, an outlier test was sufficient to process the data to remove any missing values. The highest and lowest outlier limits that were used to get rid of outliers were calculated using the formulas in Table 2 below:

Table 2: Outlier check

Outlier	**Formula**	**Description**
Highest outlier (y_{high})	$Xavg + K_n\sigma$	For a sample size of 36 years, K_n=2.628 (Chow et.al, 1988). σ is the standard deviation of the dataset.
Lowest outlier (y_{low})	$Xavg - K_n\sigma$	

Based on the availability of energy budget satellite data from POWER NASA, the study period chosen was from 1982 to 2020 as limited by the parameter with the lowest temporal range; which was All Sky Surface Longwave Upward Irradiance. 6 parameters relevant to the energy budget were collected from the satellite data on a monthly and annual daily average timestep (Table 3). These parameters were analyzed and an energy budget for the entire basin was developed. The abbreviation in the table is useful in requesting satellite data, particularly when using the API request

Table 3: Energy budget parameters analysed

Parameter	**Abbreviation**	**Parameter definition**	**Units**	**Timestep**	**Years of data available**
Top-Of-Atmosphere Shortwave Downward Irradiance	TOA_SW_DWN	This is the total amount of solar radiation that is received at the top of the atmosphere (both direct and diffuse) on a hypothetical horizontal plane. It is essentially the amount of solar radiation that enters Earth's atmosphere from space.	W/m^2	Daily average	1982-2021
All Sky Surface Shortwave Downward Irradiance	ALLSKY_SFC_SW_DWN	This is the total amount of solar radiation that is received at the surface of the earth (both direct and diffuse) on a hypothetical horizontal plane. It is also known as the Global Horizontal Irradiance (GHI)	W/m^2	Daily average	1982-2021

Parameter	Abbreviation	Parameter definition	Units	Timestep	Years of data available
All Sky Surface Shortwave Upward Irradiance	ALLSKY_SFC_SW_UP	This is the total amount of solar radiation that is reflected upwards (and presumably out into space)	W/m^2	Daily average	1984-2020
All Sky Surface Albedo	ALLSKY_SRF_ALB	This ratio represents the rate of reflectivity of the earth's surface; it is calculated by dividing the total amount of solar energy reflected by the surface of the earth by the total amount of solar energy incident reaching the surface of the earth	W/m^2	Daily average	1982-2021
All Sky Surface Longwave Downward Irradiance	ALLSKY_SFC_LW_DWN	This is the total amount of downward thermal infrared irradiance reaching the surface of the earth on a hypothetical horizontal plane. It is also called the Horizontal Infrared Radiation Intensity from Sky. It represents the amount of energy reflected down from the atmosphere by the greenhouse effect.	W/m^2	Daily average	1982-2021
All Sky Surface Longwave Upward Irradiance	ALLSKY_SFC_LW_UP	This is the total amount of upward thermal infrared irradiance from the surface of the earth to the atmosphere. Therefore, it is the energy released from the earth into the atmosphere as longwave radiation	W/m^2	Daily average	1984-2020

Data for these parameters was collected for individual stations and their area of influence was determined; for use in the analysis of the total energy budget parameters for the basin. This area of influence was determined using Thiessen polygons (Figure 3). The Thiessen polygons are based on the premise that the area of influence of a station is always at the midpoint between the station in question and the closest station to it. In a nutshell, each polygon has exactly one generating point /station and any point chosen inside the polygon is closer to its generating

point than any other point/station (Cheng, et al., 2017). Thus, to determine the overall parameter for the watershed, the sum of parameters collected for an entire basin was multiplied by the percentage influence of the station in the basin (area of influence determined by theissen polygons/total basin area). The method was chosen based on its simplicity and ease of use.

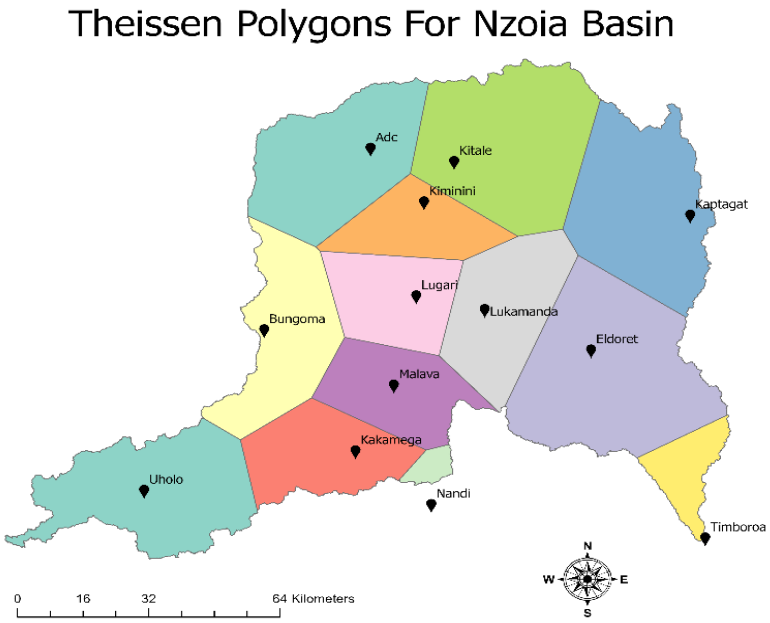

Figure 3: Theissen Polygons Showing Area of Influence (as calculated in the study using ArcGIS)

3) Results

3.1 Basin Characteristics

The study concluded that the catchment area receives 2 peaks of solar irradiance every year. The first peak occurs in March, at an average of 436.37 W/m^2 while the second peak occurs in September to October at an average of 428.78 W/m^2. Similarly, the first trough and the lowest shortwave solar irradiance incident to the atmosphere occurs in June and July, at an average of 389.19 W/m^2. The second lowest point of incident solar radiation occurs in December at 408.51W/m^2. This is in line with the summer (June) and Winter (September) solstice, and the equinoxes (March and September). Consequently, the basin receives an average monthly solar irradiance of about 415.65 W/m^2.

On an annual basis, the total solar irradiance reaching the basin was observed to be sinusoidal, with peaks of maximum solar irradiance over the watershed occurring about every 14 years

(Figure 4). These peaks and troughs were attributed to the solar cycle; which is explained by the change in sunspot activity on the sun. Table 4 shows the recorded solar cycles observed during the study. The solar cycles are typically indicated in numbers ordered from the first observed solar cycle in 1755 when extensive recording of solar sunspot activity began.

Table 4: Effect of solar cycles on shortwave irradiance received in the Nzoia basin during the study period

Solar Cycle	Start Year	Peak Year	End Year	Peak Radiation (W/m^2)
Solar Cycle 22	1986	1989	1996	415.69
Solar Cycle 23	1996	2002	2008	415.75
Solar Cycle 24	2008	2015	2019	415.71

3.2 Trends and Patterns in the Energy Budget

The top of atmosphere shortwave downward irradiance incident on the Nzoia basin exhibited sinusoidal behaviour on an annual basis due to the solar cycles. However, trend analysis indicates that the parameter varied very slightly over the years, with a range of 0.36 W/m^2 between the maximum and the minimum values in annual averages during the 36 years in which the study was carried out (Figure 4). Overall, it was observed that there is very little annual change of the annual Top of atmosphere shortwave radiation, with trend analysis revealing that the radiation did not change by much over the years (by about 0.0009 W/m^2 per year) over the study period. For this study, therefore, it can be concluded that the incident shortwave radiation entering the atmosphere system remained relatively constant.

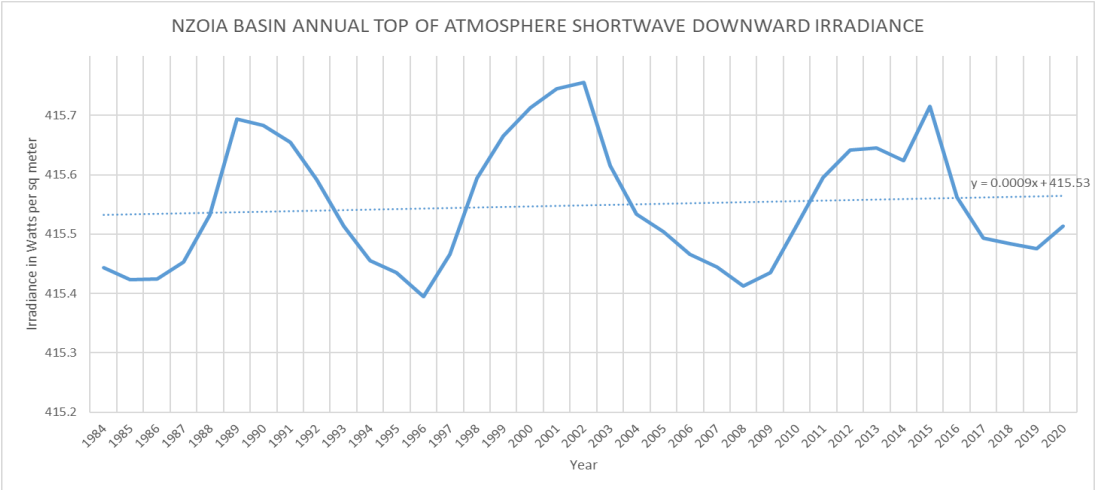

Figure 4: Annual changes in Top of atmosphere shortwave radiation

On the other hand, the shortwave downward irradiance reaching the earth's surface showed variation on a monthly timestep, with a range of about 54 W/m^2 between the maximum and minimum monthly averages. This monthly variation can be attributed to the reflective capabilities of the atmosphere (mainly the clouds). This means that more cloud cover during the year translated to more reflection of solar radiation and thus less of this radiation reaching the earth. It was also observed that annual patterns indicated frequent fluctuations in annual values of shortwave downward irradiance due to differences in annual weather conditions over the study period (Figure 5). This is an indicator that the annual weather conditions in the watershed fluctuated sporadically over the study period. While the trend analysis revealed a drop in about 0.2 W/m^2 every year at a glance, it is important to keep in mind that there are very wide fluctuations in downward shortwave radiation, with values toward the end of the study period not deviating by very much when compared with any other year during the study period.

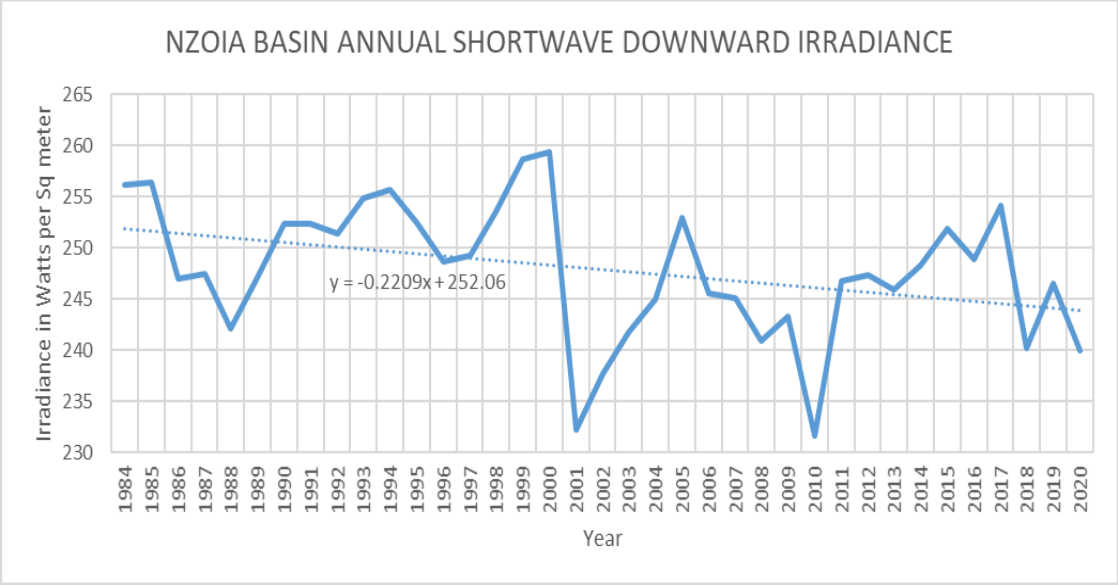

Figure 5: Annual changes in shortwave downward irradiance

The amount of shortwave radiation being reflected out from the earth's surface shows little variation on a monthly timestep, with differences of 4.58 W/m^2 between the maximum and minimum monthly values. This is because changes in reflected shortwave radiation depend chiefly on the surface albedo (reflectance of the earth). The surface albedo is determined by land use; and this feature changes gradually over time, implying that its effects would not be

obvious over a short period. On an annual basis, this effect on the change of land use becomes much more significant. The study observed that the amount of shortwave radiation being reflected upward dropped significantly over the study period (Figure 6). Trend analysis revealed that the figures dropped at the highest rate for all values of the energy budget (by about 0.6 W/m^2 per year) in the basin. Such a drop can only be explained by significant changes in land use. Therefore, analysis of the surface albedo and the land use and land cover for the basin over the study period would provide more information from which to derive a conclusion.

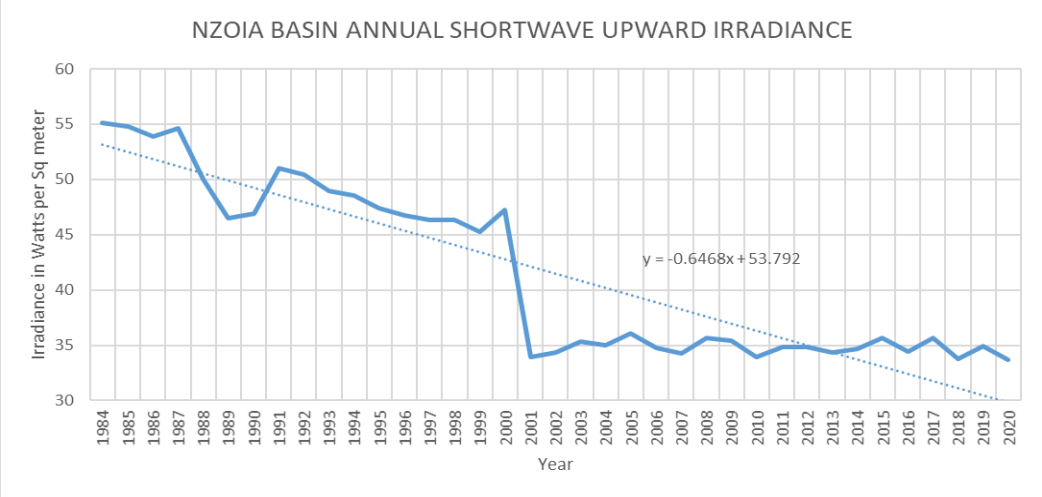

Figure 6: Annual changes in shortwave upward irradiance

The analysis of the surface albedo revealed that land use in the basin is changing significantly. Similar to the analysis of shortwave upward irradiance, monthly surface albedo had a range of 0.02 between maximum and minimum monthly values, revealing gradual changes in land use over the years. However, an analysis of yearly albedo revealed that the earth's surface in the Nzoia basin has been getting much less reflective, and therefore has been absorbing more energy from the sun over the years (Figure 7). This can be explained by an increase in the land area of surfaces that have a low surface albedo. For terrestrial areas, these include fresh asphalt (albedo 0.04), worn asphalt (albedo 0.12), Forests (albedo 0.08 to 0.18) and bare land (0.17). The analysis of the land use land cover characteristics of the basin shows that forests have been degrading in the basin but human activities such as the construction of infrastructure and the clearing of land for their activities have been increasing in terms of land surface covered (Figure 10). Therefore, we can rule out forests as being the source of this change in land use, leaving humans as the sole culprit in the increase of surface albedo in the basin.

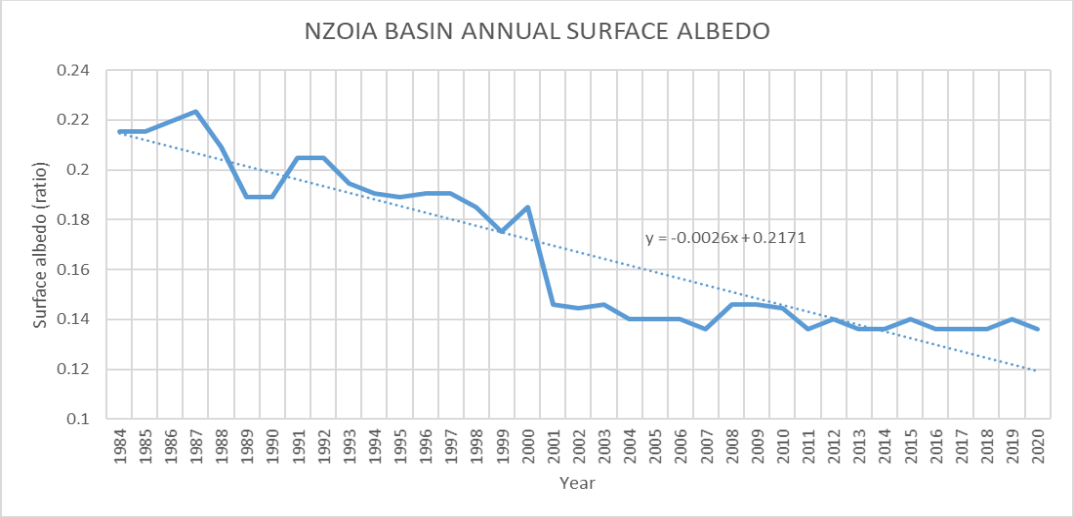

Figure 7: Annual changes in surface albedo

On closer analysis of the trends in surface albedo and shortwave upward irradiance datasets, there are noticeable changes in annual trends observed from the year 1999 onward (Figures 6 and 7). This means that while land degradation still occurred in the basin, there must have been significant efforts in terms of conserving the land use from that time onward, resulting in a slowing of the degradation of the land. Historical analysis reveals that it was at this time that the National Environment Management Authority (NEMA) was established and this period also coincided with the work of prominent environmentalists like Wangari Maathai and was when the greenbelt movement started to take hold. This is encouraging as it reveals that environmental conservation efforts can have observable positive impacts if they are properly implemented.

Longwave downward irradiance for the Nzoia basin has seen a steady annual increase throughout the study period (Figure 8). It exhibits a range of 20.23 W/m^2 and the amount of radiation reflected to Earth increases by 0.2 W/m^2 on an annual basis. This is concerning because this is an indication of the fact that the greenhouse effect is getting more severe in the catchment area; meaning that more longwave radiation passing through the atmosphere is trapped and released back to earth every year. This implies that temperatures in the basin are predicted to keep rising in the future.

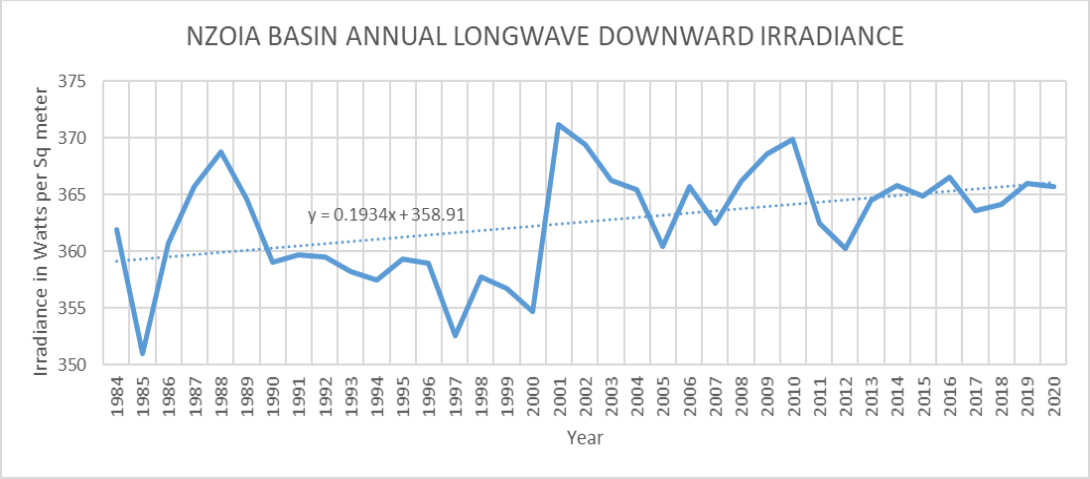

Figure 8: Annual changes in longwave downward irradiance

The results of the longwave downward irradiance are supported by those for longwave upward irradiance. Over the years, the amount of longwave radiation escaping from the earth's systems was observed to drop over the years (Figure 9). The range of this data was 11.58 W/m^2 and trend analysis revealed that the irradiance reduces by about 0.2 W/m^2 on an annual basis. This gives credence to the theory that the greenhouse effect on the watershed is worsening over time.

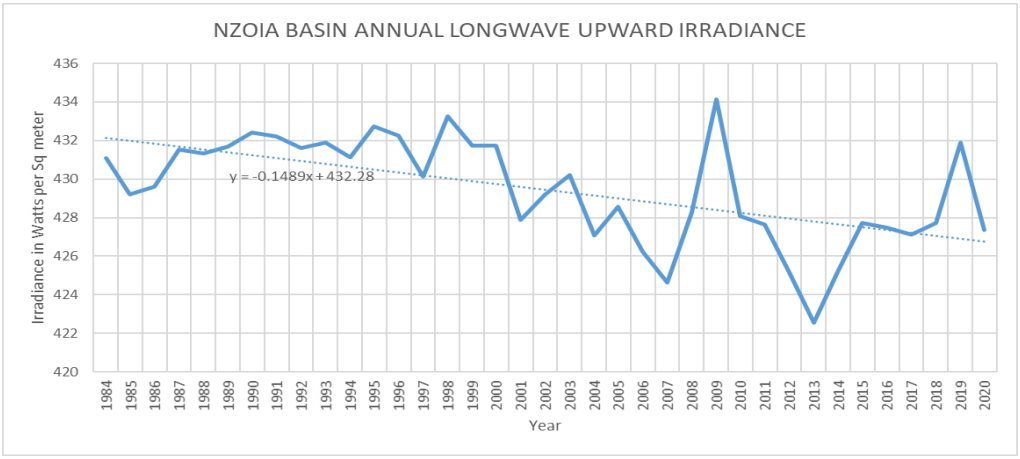

Figure 9: Annual changes in longwave upward irradiance

3.3 Commentary on Land Degradation in the Catchment

Supervised classification of Landsat 8 imagery data revealed a steady progression of human encroachment into the pristine landscapes of the basin. This has led to a considerable increase in the amount of barren land, human settlement, major roads, industries, infrastructure and

other relevant human use for the natural resources in the catchment. For instance, Figure 10 shows the difference between land use in the basin for 2015 and 2020, showing just how rapidly urban centres, human habitation and the development of road networks and infrastructure in the basin. However, while the degradation of land is dire for the catchment, there is still an opportunity to mitigate the progression of climate change in the basin by enshrining conservation strategies in decision-making and ensuring that sustainable and responsible use of the land is implemented when addressing the needs of the growing population in the watershed.

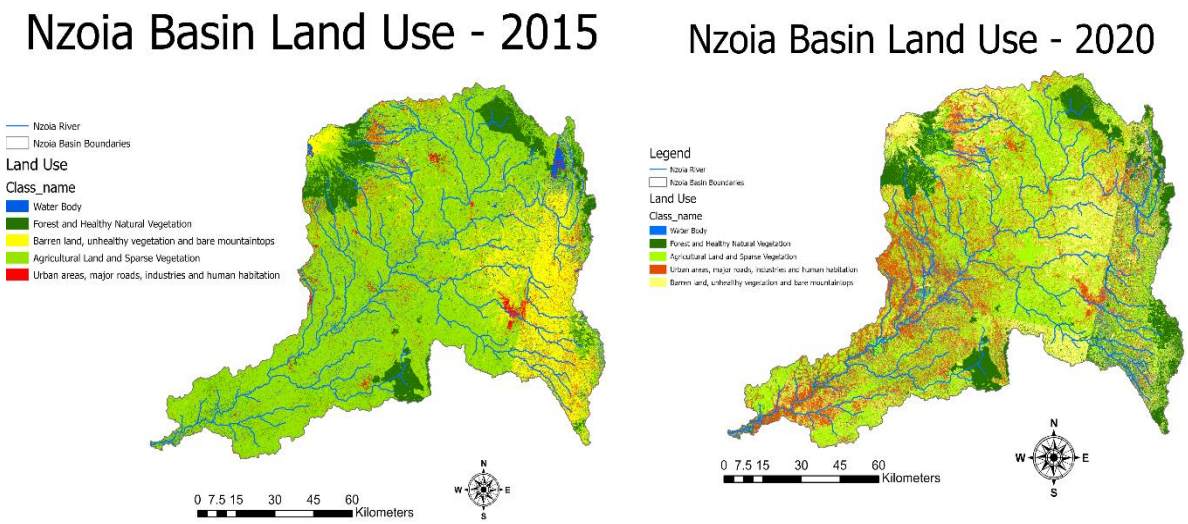

Figure 10: Supervised classification of land use in Nzoia basin; 2015 vs. 2020

4) Conclusion

Generally, the study analyzed energy parameters for the study period and showed that the catchment area exhibits the following average parameters: 415.55 W/m^2 for TOA_SW_DWN, 247.87 W/m^2 for ALLSKY_SFC_SW_DWN, 41.50 W/m^2 for ALLSKY_SFC_SW_UP, 362.60 W/m^2 for ALLSKY_SFC_LW_DWN, and 429.45 W/m^2 for ALLSKY_SFC_LW_UP. As a percentage of TOA_SW_DWN (the incident shortwave solar radiation at the top of the atmosphere), this resulted in 60%, 10%, 87% and 103% respectively. In concurrence with three values, the average surface albedo for the basin was found to be about 0.17; implying that on average around 83% of the incident solar radiation on the surface of the earth in the watershed is absorbed by the earth. The analysis of the energy budget for the basin concludes that the basin is retaining more energy over time due to a combination of land degradation and the

greenhouse effect due to the release of greenhouse gases into the atmosphere (particularly Carbon (IV) Oxide). While the catchment area faces challenges due to climate change, the study found that efforts and regulations to conserve the environment are accompanied by a change in the energy budget towards a more positive note. For instance, the slowing down of land degradation (depicted by the rate of the reduction of annual albedo) in 1999 due to a combination of factors like the establishment of NEMA and the work of Wangari Maathai and the Greenbelt movement which led to an increase in environmental awareness in Kenya could be observed directly on the data. Therefore, while climate change issues still plague the basin, there is still hope for improvement if sustainable and environmentally conscious management strategies are implemented.

Acknowledgement

The author would like to acknowledge the late Dr. Job Rotich Kosgei (Moi University), Gilbert Nyageikaro Nyandwaro (Moi University), Ednah Jelagat Kemboi (Moi University), Noah Kipyego Sum (Moi University) and Prof. Yashon Ouma (Moi University) for providing technical consultation during the research phase of the project

References

Atkinson, J. (2017, August 7). *What is Earth's Energy Budget? Five Questions with a Guy Who Knows*. Retrieved from National Aeronautics and Space Administration (NASA): https://www.nasa.gov/feature/langley/what-is-earth-s-energy-budget-five-questions-with-a-guy-who-knows

Cassia, R., Nocioni, M., Correa-Aragunde, N., & Lamattina, L. (2018). Climate Change and the Impact of Greenhouse Gasses: CO2 and NO, Friends and Foes of Plant Oxidative Stress. *Frontiers in Plant Science, 9*. doi:https://doi.org/10.3389/fpls.2018.00273

Cheng, M., Wang, Y., Engel, B., Zhang, W., Peng, H., Chen, X., & Xia, H. (2017). Performance Assessment of Spatial Interpolation of Precipitation for Hydrological Process Simulation in the Three Gorges Basin. *Water, 9*(11). doi:https://doi.org/10.3390/w9110838

Chow, V. T., Maidment, D. R., & Mays, L. W. (1988). *Applied Hydrology.* Mc Graw Hill .

Gettelman, A., & Rood, R. B. (2016). *Demystifying Climate Models.* Heidelberg: Springer Berlin. doi:https://doi.org/10.1007/978-3-662-48959-8

Harris, N. L., Gibbs, D. A., Baccini, A., Birdsey, R. A., Bruin, S. d., Farina, M., . . . Saatchi, S. S. (2021). Global maps of twenty-first century forest carbon fluxes. *Nature Climate Change, 11*, 230-240. doi:https://doi.org/10.1038/s41558-020-00976-6

Iliadis, C. (2015). *Nuclear Physics of Stars* (2nd ed.). John Wiley & Sons. Retrieved from https://books.google.co.ke/books?id=iUCkBgAAQBAJ&source=gbs_navlinks_s

Katagiri, S., Hayasaka, T., Shimizu, A., Matsui, I., Nishizawa, T., Sugimoto, N., & Takamura, T. (2013). Long term analysis of cirrus clouds' effects on shortwave and longwave radiation derived from data acquired by ground-based and satellite-borne observations. *AIP Conference Proceedings, 1531*(1), 492-495. doi:http://dx.doi.org/10.1063/1.4804814

Kipkulei, H. K., Bellingrath-Kimura, S. D., Lana, M., Ghazaryan, G., Boitt, M., & Sieber, S. (2022). Modelling cropland expansion and its drivers in Trans Nzoia County, Kenya. *Modeling Earth Systems and Environment, 8*, 5761–5778. doi:https://doi.org/10.1007/s40808-022-01475-7

Moses, A. N., Oteng, M., Masibayi, S. B., Maloba, F. A., & Mokua, E. (2015). GIS-based modeling of land use dynamics in River Nzoia basin, Kenya. *Global Journal of Engineering Science and Research Management, 2*(9), 88-104. Retrieved from http://www.gjesrm.com/Issues%20PDF/Archive-2015/September-2015/11.pdf

Mureithi, K., Kosgei, J. R., Nyandwaro, G. N., Kemboi, E. J., & Sum, N. K. (2022). Runoff estimation using satellite images in sparsely gauged basins: a case of Nzoia River Basin, Kenya. *Water Practice & Technology, 17*(8), 1758–1768. doi:https://doi.org/10.2166/wpt.2022.088

Musau, J., Sang, J., Gathenya, J., & Luedeling, E. (2015). Hydrological responses to climate change in Mt. Elgon watersheds. *Journal of Hydrology: Regional Studies, 3*, 233-246. doi:https://doi.org/10.1016/j.ejrh.2014.12.001

Stüeken, E. E., Som, S. M., Claire, M., Rugheimer, S., Scherf, M., Sproß, L., . . . Lammer, H. (2020). Mission to Planet Earth: The First Two Billion Years. *Space Science Reviews, 216*. doi:https://doi.org/10.1007/s11214-020-00652-3

Trenberth, K. E., Fasullo, J. T., & Kiehl, J. (2009). Earth's Global Energy Budget. *Bulletin of the American Meteorological Society, 90*(3), 311-324. doi:https://doi.org/10.1175/2008BAMS2634.1

Editorial Committee

Editorial Board

INSTRUCTIONS TO CONTRIBUTORS

The editorial staff of the AJERI requests contributors of articles for publication to observe the following editorial policy and guidelines accessible at https://www.iekenya.org/ in order to improve communication and to facilitate the editorial process.

Criteria for Article Selection

Priority in the selection of articles for publication is that the articles:

a. Are written in the English language
b. Are relevant to the application relevant of engineering and technology research and Innovation
c. Have not been previously published elsewhere, or, if previously published are supported by a copyright permission
d. Deals with theoretical, practical and adoptable innovations applicable to engineering and technology
e. Have a 150 to 250 words abstract, preceding the main body of the article
f. The abstract should be followed by a list of 4 to 8 "key Words"
g. Manuscript should be single-spaced under 4,000 words (approximately equivalent to 5-6 pages of A4-size paper)
h. Are supported by authentic sources, references or bibliography

Rejected/Accepted Articles

a. As a rule, articles that are not chosen for AJERI publication are not returned unless writer (s) asks for their return and are covered with adequate postage stamps. At the earliest time possible, the writer (s) is advised whether the article is rejected or accepted.
b. When an article is accepted and requires revision/modification, the details will be indicated in the return reply from the AJERI Editor, in which case such revision/modification must be completed and returned to AJERI within three months from the date of receipt from the Editorial Staff.
c. Complementary copies: Following the publishing, three successive issues are sent to the author(s)

Procedure for Submission

a. Articles for publication must be sent to AJERI on the following address:

The Editor

African Journal of Engineering Research and Innovation

P.O Box 41346- 00100

City Square Nairobi Kenya

Tel: +254 (20) 2729326, 0721 729363, (020) 2716922

E-mail: editor@iekenya.org

b. The article must bear the writer (s) name, title/designation, office/organization, nationality and complete mailing address. In addition, contributors with e-mail addresses are requested to forward the same to the Editor for faster communication.

For any queries, authors are requested to contact by mail (editor@iekenya.org).

PUBLISHER

The Institution of Engineers of Kenya (IEK)

P.O Box 41346- 00100

City Square Nairobi Kenya

Tel: +254 (20) 2729326, 0721 729363, (020) 2716922

Email: editor@iekenya.org

Website: www.iekenya.org

CONTENTS